The Turbulence Structure of Heated Supersonic Jets with Offset Total Temperature Non-Uniformities

David Earl Mayo Jr.

Dissertation submitted to the faculty of the
Virginia Polytechnic Institute and State University
in partial fulfillment of the requirements for the degree of

Doctor of Philosophy
In
Mechanical Engineering

Wing F. Ng, Chair
K. Todd Lowe, Co-Chair
Walter F. O'Brien
Luca Massa
Ricardo A. Burdisso

July 25th 2019
Blacksburg, Virginia

Keywords: fluid dynamics, supersonic jets, particle image velocimetry, compressible shear layers, jet noise, turbulence

The Turbulence Structure of Heated Supersonic Jets with Offset Total Temperature Non-Uniformities

David Earl Mayo Jr.

(Abstract)

Noise induced hearing loss is a large concern for the Department of Defense. Personnel on aircraft carriers are exposed to dangerous noise levels of noise from tactical aircraft, causing hearing damage which results in significant costs for medical care and treatment. Additionally, NASA and the FAA have begun to investigate the viability of reintroducing supersonic commercial transport in the United States and one of the largest problems to address is reducing the noise impact of these aircraft on communities.

The overarching goal of jet noise research is to optimize noise reduction techniques for supersonic jets. In order to achieve this, a more complete theoretical framework which links the jet boundary conditions to the turbulence production in the jet plume and the far-field radiated noise must be established. The research presented herein was conducted on the hypothesis that introducing thermal non-uniformities into a heated supersonic jet flow can favorably alter the turbulence structure in the jet shear layer, leading to reductions in radiated noise.

To investigate the impact of temperature on the turbulence development in the jet, spatially resolved three-component velocity vectors were acquired using particle image velocimetry (PIV) performed on two small-scale perfectly expanded Mach 1.5 jet flows, one with a uniform temperature profile and another containing a geometrically offset temperature non-uniformity.

Using the PIV data, the mean velocities, Reynolds stresses, and correlation coefficients were obtained from both jet flows and compared to analyze changes in the mean turbulence field. Small but significant reductions in the shear layer turbulence were observed in the near nozzle region of the thermally offset jet when compared to the uniform jet case. The changes result in a thickening of the shear layer nearest the location of the cold plume which alters the integral length scales of the coherent turbulent structures in the offset jet in a manner consistent with other techniques presented in the literature that reduce jet noise.

Applying quadrant analysis, a conditional averaging technique, to the jet turbulence plume revealed changes in the statistical flow field of Reynolds shear stress structures. The changes provide strong evidence of the presence of intermittent stream-wise vortical structures which serve to reduce the spatial correlation levels of turbulence in the thermally offset jet flow when compared to the uniform baseline jet.

(375 words)

This work was sponsored by the U.S. Office of Naval Research, program manager Dr. Steven Martens, via grants N00014-16-1-2444 and N00014-14-1-2836.

The Turbulence Structure of Heated Supersonic Jets with Offset Total Temperature Non-Uniformities

David Earl Mayo Jr.

(General Audience Abstract)

Increasingly large and powerful engines are required as the mission requirements for tactical aircraft become more advanced. These demands come at the cost of an increased production of noise which is particularly hazardous to crewpersons operating on Navy aircraft carriers during take-off and landing. Noise-induced hearing loss from extended exposure to high noise levels has become a major medical expenditure for the Navy. To address this issue in tactical aircraft engines, the sources of jet plume noise must be reduced, but doing so requires improved understanding of the connections between nozzle boundary conditions, the jet turbulence plume, and the radiated noise while keeping in consideration system constraints and performance requirements.

The current study introduces a novel method for controlling supersonic jet noise induced by turbulence through the introduction of an offset non-uniform temperature perturbation at the nozzle mouth. Non-invasive flow measurements were conducted using stereoscopic particle image velocimetry to obtain high-resolution velocity and turbulence data. Analysis of the flow data indicate that an offset reduced temperature plume introduced at the nozzle exit has a first-order effect on the turbulence evolution which result in small, but significant reductions in jet noise levels. The reductions observed are attributed to a disruption in the coherence of the primary noise generating turbulence structures in the jet plume which are associated with the formation of stream-wise vortical structures induced by the cold plume.

Acknowledgements

First and foremost, I would like to thank my mother Miranda, whom I love and cherish most in this life. I am forever grateful to my aunts Maureen, Maxine, Melody, and Michelle who have each loved, nurtured, and raised me. My cousins, Nathaniel, Benjamin, Shawn, Buster, Ciana, Paris, Heavyn, Miracle, and Cameron, I consider each of you to be my brothers and sisters at heart. And to the rest of my family, I appreciate your love, support, and commitment to me in my pursuit of my Ph.D immensely.

To my advisors, Dr. Wing Ng and Dr. K. Todd Lowe, the advice and mentorship you each have provided has molded me into the engineer I have become today. Furthermore, I would like to thank the remaining members of my committee, Dr. Walter O'Brien, Dr. Ricardo Burdisso, and Dr. Luca Massa for their guidance and feedback on the research presented herein.

During my time in graduate school, I have had the great pleasure of meeting many wonderful students with whom we have toiled and suffered and overcome many challenges and have equally celebrated many more successes. I would like to take the time to mention a few of these individuals. Dr. Allan Arisi, Dr. Andrew Boulanger, Ashley Saltzman, Dr. Jacob Delimont, Dr. James Phillips, Dr. Jaideep Pandit, John Gillespie, John Hutchinson, Kevin Peterson, Matt Murdock, Dr. Raul Otero, Ryan Hehir, Sean Brennan, Sean Shea, Stephen Edelmann, and Dr. Tamy Guimarães.

I would like to give special thanks to my friend and researcher-in-arms, Kyle Daniel. His contributions to the research presented here is immeasurable and without his dedication, support, and companionship, many of the accomplishments achieved during this project would not have been possible.

Finally, I would like to give special thanks to Dr. Brenda Henderson for her tutelage during my internship at NASA Glenn Research Center and our sponsor, the Office of Naval Research for trusting us with the task of performing the jet noise research presented in this dissertation.

Contents

List of Figures

List of Tables

Attributions

Many colleagues and professors have aided in the development of the research and writing of this dissertation. An overview of their contributions is detailed below.

Dr. Wing F. Ng is the primary advisor and committee co-chair for this project. He provided extensive guidance for the research presented in this dissertation.

Dr. K. Todd Lowe is a co-advisor and committee chair for this project. He provided technical guidance for the research presented and significantly contributed to the scientific analysis of the data acquired and the editing of the papers generated during this project.

Kyle A. Daniel is a doctoral candidate who has worked alongside me in this research project and is a co-author on all of the journal papers and conference proceedings presented within. We jointly developed the concept, design, manufacturing of the modifications made to the heated jet rig to conduct the research presented herein. Additionally, he assisted with acquisition all of the experimental PIV and probe data. Our frequent discussions regarding my findings in the turbulence data and his findings from acoustic measurements on the same flow field have helped to shape the conclusions found from this study.

1. Introduction

Noise induced hearing loss is a large concern for the Department of Defense. Personnel on aircraft carriers are exposed to dangerous noise levels of noise from afterburning tactical aircraft, causing hearing damage which results in significant costs for medical care and treatment. Additionally, NASA and the FAA have begun to investigate the viability of reintroducing supersonic commercial transport in the United States and one of the largest problems to address is reducing the noise impact of these aircraft on communities.

The overarching goal of jet noise research is to optimize noise reduction techniques for supersonic jets. In order to achieve this, a more complete theoretical framework which links the jet boundary conditions to the turbulence production in the jet plume and the far-field radiated noise must be established. Many methods of supersonic jet noise suppression have been investigated over the years, including nozzle chevrons, fluidic injections and inserts, asymmetric multi-stream jets, and inverted velocity profile jet flows. All of the previously mentioned methods serve to alter the boundary conditions at the nozzle exhaust to alter the turbulence development in the jet shear layer. These noise control mechanisms have been shown to statistically increase turbulence intensity near the nozzle and/or produce stream-wise vortical structures, both of which are features of free-shear layer flows that are associated with favorable reductions of noise radiated to the far-field.

Throughout the history of supersonic jet noise research, many investigations have been conducted on jet flows, both heated and unheated, ranging from small scale laboratory jets to full scale military jet engines. Experimental methods in supersonic jet noise have improved drastically over the years, initially beginning with near-field and far-field microphone arrays, flow intrusive probe measurements, and path integrated flow imaging (i.e. shadowgraph and Schlieren photography). Due to advances in laser diagnostics, such as Laser Doppler Anemometry (LDA), Doppler Global Velocimetry (DGV), and Particle Image Velocimetry (PIV), highly resolved spatial or temporal resolution measurements of the jet flow field have provided a much richer understanding of jet turbulence. Unfortunately, due to the high flow speeds in supersonic jets and the current technical limitations of experimental equipment, achieving the holy grail of high spatially and temporally resolved three-dimensional velocity measurements simultaneously has not been achieved.

Due to this limitation, researchers have turned to computational fluid dynamics (CFD) to complete the picture and advance jet noise research. The many advances made in computational predictions of jet noise have allowed for high fidelity, three dimensional visualization and analysis of the turbulence and acoustic fields of supersonic jet flows. However, the ever present limitations of turbulence modelling still require investigators to turn to experiments for validation of conclusions and improvements. The experimental and computational efforts, when used in conjunction, have resulted in significant progress in identifying the key parameters that affect noise radiated from supersonic jets and in producing analytical and empirical models for predicting said noise.

The culmination of the aforementioned efforts has resulted in the following parameters being identified, in different combinations, as key metrics to target in the effort to reduce jet noise: the nozzle geometry, the convection velocity, the velocity ratio, and the density or temperature ratio. These values all have a significant impact on the length and time scales of turbulence structures in the jet shear layer, the coherence of said turbulent structures, and the formation of shocks in the jet potential core, all of which affect the three types of supersonic jet noise; screech tones, broadband shock-associated noise (BBSAN), and turbulent mixing noise.

The research presented herein investigates the novel idea of introducing thermal non-uniformities into a heated supersonic jet flow to reduce turbulent mixing noise. In introducing locally reduced temperature plumes into an otherwise heated jet flow, it is hypothesized that the noise produced large-scale coherent turbulence in the shear layer of supersonic jets will be lessened due to a reduction in their coherence, a redistribution of turbulent kinetic energy into less acoustically efficient turbulence structures, and slowing of the convection speeds within the jet shear layer.

1.1 Structure and Contents

The dissertation is presented in five parts, as described below:

Chapter 1 introduces the subject matter to the audience, outlines the structure of the paper, and describes the unique contributions of the Ph.D. candidate to the jet noise community.

Chapter 2 contains the literature review for supersonic jet noise as it applies to the study presented herein.

Chapter 3 is a research study published in the AIAA Journal entitled "The Mean Flow and Turbulence Characteristics of a Heated Supersonic Jet with an Offset Total Temperature Non-Uniformity", (doi: 10.2514/1.J058163). The study analyzes the global changes in the velocity and turbulence profiles of a supersonic jet containing an offset total temperature non-uniformity and the potential impact the changes may have on far-field radiated noise.

Chapter 4 is a research study titled "Statistical Flow Structure in Heated Supersonic Jets with Offset Temperature Non-Uniformities" to be submitted for publication in the AIAA Journal. The study investigates the changes in the statistical turbulence structure of a supersonic jet with an offset temperature non-uniformity using a unique application of quadrant analysis, a conditional averaging technique mostly used in analyzing wall-bounded turbulent flows.

Chapter 5 summarizes the findings of the studies presented in this dissertation and recommends additional work which may be pursued in the future to advance the research further.

The formatting in each chapter will vary according to the publication guidelines for the journals in which they have been, or will be, submitted.

1.2 Achievements

The major accomplishments of the work presented include:

- Experiments were conducted on two perfectly expanded, Mach 1.5 heated jet flows, one with a uniform velocity and temperature profile at the nozzle exhaust operated at a total temperature ratio (TTR) of 1.9, which serves as the baseline flow, and the other with a uniform Mach number profile at the nozzle exhaust with a TTR 2.0 heated jet flow and a locally offset reduced temperature plume with a TTR of 1.3.

- One-of-a-kind stereo PIV measurements were conducted on both jet flows to obtain spatially resolved three-component velocities in both jet flows to investigate the changes in the mean velocity and turbulence profiles and structures that result from the presence of the thermal non-uniformity

- The introduction of the offset thermal non-uniformity revealed, compared to the uniform jet flow, a local reduction in the axial velocity profile of ~15% near the nozzle exhaust, small but significant alterations of the mean turbulence structure in the jet flow throughout the shear layer in the developmental region of the jet.

- The application of quadrant analysis to the shear layer of the supersonic jet flow revealed significant alterations in the statistical Reynolds shear stress structures in the shear layer of the thermally offset jet. Reductions in the axial length scales and increases in the radial length scales of the structures were observed. Streamlines of the conditionally averaged fluctuating velocity field revealed a dramatic shift in the nature of the three-dimensional turbulence field, providing evidence of the presence of stream-wise vortical structures and de-coherence of the resolved shear stress structures.

1.2.1 Claims

The key contributions and main claims of this work are as follows:

- Introducing a reduced temperature non-uniformity into a heated jet flow induces global changes in the axial and radial turbulence profiles in the developmental region of the supersonic jet shear layer akin to what is observed in asymmetric multi-stream jets.

- The offset temperature non-uniformity induces the formation of locally intermittent stream-wise vortical structures which reduces the correlation level of turbulent shear stress structures in the jet.

1.2.2 List of Publications

What follows are a list of the scientific publications produced by the author during his time as a Ph.D. student.

Peer-reviewed Journal Publications:

- Mayo Jr., D.E., Daniel, K.A., Lowe, K.T., and Ng, W.F., "*The Flow and Turbulence Characteristics of a Heated Supersonic Jet with an Offset Total Temperature Non-Uniformity*," *AIAA Journal*, May 2019

- Mayo Jr., D.E, Daniel, K.A., Lowe, K.T., and Ng, W.F., "*Statistical Flow Structures in Heated Supersonic Jets with Offset Temperature Non-Uniformities"*, AIAA Journal, (not yet published)

- Daniel, K.A., Mayo Jr., D.E., Lowe, K. T., and Ng, W. F., 2019, "*Use of Thermal Non-Uniformity to Reduce Supersonic Jet Noise,"* AIAA Journal, 2019 (not yet published)

Conference Proceedings:

- Mayo Jr., D.E, Daniel, K.A., Lowe, K.T., and Ng, W.F., "*Statistical Flow Structures in Heated Supersonic Jets with Offset Temperature Non-Uniformities",* 25th AIAA/CEAS Aeroacoustics Conference, (AIAA 2019-2708)

- Daniel, K.A., Mayo Jr., D.E, Lowe, K.T., and Ng, W.F., "*Space-time Description of Density Near-Field in a Non-Uniformly Heated Jet",* 25th AIAA/CEAS Aeroacoustics Conference, (AIAA 2019-2474)

- Daniel, K.A., Mayo Jr., D.E, Lowe, K.T., and Ng, W.F., "*Experimental Investigation on the Acoustic Field and Convection Velocity of Structures in a Heated Jet with Centered Thermal Non-Uniformity,"* AIAA SciTech 2019 Forum, (AIAA 2019-1300)

- Mayo Jr., D.E, Daniel, K.A., Lowe, K.T., and Ng, W.F., "*The Flow and Turbulence Characteristics of a Heated Supersonic Jet with an Offset Total Temperature Non-Uniformity",* 24th AIAA/CEAS Aeroacoustics Conference, AIAA AVIATION Forum, (AIAA 2018-3144)

- Daniel, K.A., Mayo Jr., D.E., K., Lowe, K.T., and Ng, W.F., " *Experimental Investigation of the Very Near Pressure Field of a Heated Supersonic Jet with a Total Temperature Non-Uniformity",* 24th AIAA/CEAS Aeroacoustics Conference, AIAA AVIATION Forum, (AIAA 2018-3145)

- Mayo Jr., D.E, Daniel, K. A., Lowe, K.T., and Ng, W.F., "*Experimental Investigation of a Heated Supersonic Jet with Total Temperature Non-Uniformity",* 23rd AIAA/CEAS Aeroacoustics Conference, AIAA AVIATION Forum, (AIAA 2017-3521)

2. Literature Review

2.1 Introduction to Supersonic Jet Noise

There exist three major components which make up the noise generated from supersonic free jets: broadband shock associated noise, screech tones, and turbulent mixing noise. With the exception of perfectly expanded jets (i.e. jet flows in which a nozzle is designed using the method of characteristics to expand the flow in such a way that no shocks are formed), all three noise mechanisms are exhibited by supersonic jets. A basic overview of the three mechanisms are given in this section.

2.1.1 Broadband Shock Associated Noise and Screech Tones

Broadband shock associated noise (BBSAN) is produced by the interaction of turbulence in the jet shear layer with shock waves present within the jet flow. BBSAN consists of primarily high frequency components and radiates at all polar angles from the jet axis, but typically has peak narrowband spectra values towards the downstream jet flow direction. Ribner [1] originally proved that a turbulent eddy which passed through a shock would produce entropy, velocity fluctuations, and a sound wave as a result of the interaction. This lead Harper-Bourne and Fisher [2] to successfully develop the first source model for BBSAN. Using the model, Harper-Bourne and Fisher found that turbulent eddies which had axial correlation length scales that extended over many shock cell lengths exhibited the highest acoustic radiation efficiency. The most successful model for predicting BBSAN noise was invented by Tam [3], who used instability wave theory to develop a robust model for predicting narrowband spectra produced from BBSAN in supersonic jets.

Screech tones are caused by a feedback loop formed between the shock cell structures within a supersonic jet, the turbulence in the jet shear layer, and the nozzle lip thickness. When screech is present, intense oscillations can be detected in the flow field that are either toroidal or helical in nature [4]. Screech produces a distinct, high amplitude tone at a fundamental frequency (defined by the nozzle geometry and the flow conditions) which radiates primarily in the forward flight direction and occasionally resonates at higher harmonic frequencies. Screech tones were first experimentally investigated by Powell [5], followed by many other studies [4,6–9]. Both Tam [10] and Morris et al. [11], using instability wave theory, have produced reliable models for predicting the fundamental screech tone frequency and directivity, though prediction of the amplitude is still subpar.

The focus of the studies presented in this dissertation is understanding the mechanisms of sound generated from the self-interaction of turbulence. Thus, the nozzle was carefully designed to remove, as much as physically possible, the presence of shocks from the jet exhaust. In doing so, the dominant noise producing sources are caused by turbulent mixing noise.

2.1.2 Turbulent Mixing Noise

Turbulent mixing noise is caused by the self-interaction and convection of turbulence. In jet flows, turbulence mixing noise is produced by fine-scale and large-scale turbulent structures. Fine scale turbulent mixing noise is characterized by broadband noise that radiates at all polar angles equally. In high speed subsonic and supersonic jets, the highest intensity mixing noise source is produced by large-scale turbulent structures present in the shear layer of the jet. One of the earliest studies to identify the presence of large scale coherent turbulent structures in jet flows was performed by Mollo-Christensen [12]. He hypothesized that in the shear layer of turbulent jets, there existed structures made up of discrete physical wavenumbers and were axially coherent over multiple jet diameters. These turbulent structures would be very efficient sources of sound when undergoing rapid distortion.

Many experimental studies have been conducted on perfectly expanded supersonic jet flows operating at various total temperature ratios [13–17]. From these investigations, general characteristics of the far-field noise spectra produced by large and fine scale turbulence can be observed. Large-scale turbulent noise exhibits peak far-field intensities that are detected at polar angles ranging from 125° to 140° as measured from the forward flight direction, with comparatively less sound radiated in forward flight directions that are attributed to fine-scale turbulence, as it is broadband in nature and radiates evenly at all directivity angles. The Strouhal (fD/U_j) numbers associated with the aforementioned peak noise levels are typically centered between 0.1 and 0.25. The directivity angle, the decibel level,

and the Strouhal number associated with the peak large-scale radiated noise are all functions of the jet temperature ratio, the nozzle exit diameter, and the jet Mach number.

2.2 Modeling Large-Scale Turbulent Mixing Noise

Throughout the history of jet aeroacoustics, researchers have investigated many approaches for modeling the noise produced by large scale turbulent mixing noise. Each approach has added another piece to fill in holes in the theories of jet noise prediction by attempting to link perturbations in jet turbulence plume to the resulting pressure field. The three major modeling approaches can be categorized into Lighthill based analogy models, instability wave models, and wavepacket models.

2.2.1 Lighthill Acoustic Analogy Based Models

The Lighthill equation is the foundation for all of aeroacoustics [18,19]. Lighthill rearranged the compressible Navier-Stokes equation such that the resulting form is similar to an inhomogeneous wave equation (Eq.1),

$$\frac{\partial^2 \rho}{\partial t^2} - c_\infty^2 \nabla^2 \rho = \frac{\partial^2 \left(\rho U_i U_j - \sigma_{ij} + (p - c_\infty^2 \rho)\delta_{ij}\right)}{\partial x_i \partial x_j} \tag{1}$$

where ρ is the density, t is time, c_∞, is the ambient speed of sound, u is velocity, σ is the viscous portion of the stress tensor, and p, is the thermodynamic pressure. The term in the brackets on the right hand side of the equation is the Lighthill stress tensor ($\tau_{ij} = \rho U_i U_j - \sigma_{ij} + (p - c_\infty^2 \rho)\delta_{ij}$). When aeroacoustics is evaluated for flows with large temperature gradients or other temperature non-homogeneities, as is present in hot supersonic jets, the Lighthill equation is often derived in terms of the pressure instead of the density (Eq.2).

$$\frac{1}{c_\infty^2}\frac{\partial^2 p}{\partial t^2} - \frac{\partial^2 p}{\partial x_j^2} = \frac{\partial^2}{\partial x_i \partial x_j}\left(\rho U_i U_j + \frac{1}{c_\infty^2}\frac{\partial^2}{\partial t^2}\left(p - c_\infty^2 \rho - \sigma_{ij}\right)\right) \tag{2}$$

The transformation provides a link between fluid dynamics and acoustics. In the general wave equation, the left hand side describes the propagation of waves and the right hand side contains the forces that produce said waves. In the Lighthill equation, this generality is not explicitly true as the density is present on both sides of the equation which means that the propagation of the "waves" emitted by the "forces" on the right hand side can affect the forces themselves and vice versa. This leads to phenomena such as pressure waves produced by the same sources as acoustic waves that decay faster $(1/r^3)$ than sound waves (which decay as $1/r$), which is known as hydrodynamic noise. Most of the solutions to this equation and others based on Lighthill's methodology assume that the fluid flow is insensitive to the effects of the induced sound field.

There are four terms on the right hand side of the Lighthill equation which produce three different types of noise sources. Monopole sources are produced by the p term, dipole sources are produced by the $c_\infty^2 \rho$ term, and quadrupole sources are produced by the $\rho U_i U_j$ and σ_{ij} terms. The first two terms only exist when the flow comes in contact with a solid object and the last two terms are produced by the self-interaction of turbulence.

For flow fields with large Reynolds numbers ($\rho U_j D/\mu \gg 1$), the viscous shear stress tensor, σ_{ij}, can be neglected and even for jet flows where solid surfaces exist, if the Mach number ($U_j/c_\infty \ll 1$) is sufficiently small, the $(p - c_\infty^2 \rho)\delta_{ij}$terms can be ignored. As a result, the noise produced by the convective turbulence term, $\rho U_i U_j$, will dominate. The result is a homogeneous wave equation which can be solved using Green's functions if the velocity and density field fields are known. The previous two assumptions used to obtain a tractable solution to Lighthill's equation are known as Lighthill's Analogy. In plain terms, the analogy replaces the turbulent field in a flow with spatially distributed quadrupole sources that produce the same far-field noise signature.

Unfortunately, the assumption of low Mach number flows leads to inaccurate predictions of jet noise using the Lighthill analogy. Additionally, the low Mach number assumption also makes solutions of the equation invalid for flows containing large temperature gradients, as found in heated jets, as it removes the contributions to the noise field caused by density changes.

To address the convection limitations of Lighthill's analogy, Curle [20] and Ffowcs-Williams [21], each extended Lighthill's analogy to include the effects of solid boundaries and uniform convection effects respectively. Soon after,

Ffowcs-Williams & Hawkings [22] developed an analogy which included the effects of both solid boundaries and uniform convection effects simultaneously. The Ffowcs-Williams-Hawkings (FW-H) equation is currently the most commonly used acoustic analogy in jet aeroacoustics as, in computational jet flows, it is used to model a radiator surface which surrounds a jet flow and captures a space-time history of the pressure or density fluctuations emitted. The effects recorded by the surface are then used to propagate the linear acoustic field to the far-field at a fraction of the computational cost which would otherwise be necessary. Since the surrounding surface is stationary and captures all of the effects of the encased turbulent field, the predicted far-field is theoretically accurate for all linear acoustic sources, which include effects of temperature.

Scaling analysis applied to the Lighthill's equation reveals an important method to estimate the total acoustic power for jet noise. In layman terms, the far-field acoustic power emitted by the developmental region of a turbulent jet is proportional to the eighth power of the jet velocity (Eq. 3). P is the acoustic power, ρ_0 is the density, U_j is the jet exit velocity, c_∞ is the ambient speed of sound, and x is the axial jet distance.

$$P \sim \frac{\rho_0 U_j^8}{c_\infty^5 x} \tag{3}$$

In order to make noise predictions using the analytical solutions of the Lighthill or FW-H equations, the cross-correlation function of the noise sources must be obtained. Many studies have developed models for the source cross-correlation function [23–27] which are based on experimental [28,29] or computational [30] two-point correlations of the velocity field. The models reveal the presence of a convective amplification effect which increases acoustic intensities associated with large-scale turbulence radiated at polar angles closer to the downstream jet direction caused by the Doppler effect. Unfortunately, the amplification predicted still did not match what was observed in experimental measurements.

The differences observed in the far-field spectra between the acoustic analogy derived models and experimental data at narrow angles to the jet axis were attributed to refraction effects [31]. To address the problem, researchers began extending Lighthill's analogy further to incorporate the effects of a convecting shear flow which surrounded the point quadrupole sources. Phillips [32] was the first to incorporate the effects of a uniformly convecting mean flow to the acoustic analogy. Lilley [33] extended Phillips's work by decoupling the mean flow interactions from the source terms, resulting in the now famous Lilley Equation. The assumptions used in deriving solutions to Lilley's equation are typically valid for supersonic Mach numbers and high temperature jets. Both equations were developed by assuming the convecting shear flow being modelled was fully parallel, which is not true in real jets as the shear layer grows with downstream distance from the source.

From analysis of Lilley's equation, the major findings for jet noise were that refraction effects on the far-field acoustics mostly impacted high frequency noise and that, for polar angles $\theta < 1/(1+M)$, where M is the Mach number, the radiated sound at high frequencies experiences an exponential decay which results in a cone of relative silence caused by the refraction effects [33]. Due to the previously mentioned parallel flow assumption, the relative cone of silence is not constant as predicted by Lilley's equation, but changes as a function of axial distance in real jets.

Even with all of the improvements and corrections made to acoustic analogies to address the discrepancies observed between acoustic analogy based models and experiments, predictions of far-field sound radiated in peak noise directions remain subpar. After reviewing the acoustic analogies, the most important conclusions to take away are that, in shock free jet flows, the primary source of noise generation is due to turbulent self-noise, the majority of which is produced by large-scale turbulence which is axially coherent over multiple jet diameters. While the aforementioned theories have had great success in predicting far-field noise radiated in directions where small-scale turbulence dominates, without additional empirical correction, the acoustic analogies have been subpar in predicting sound pressure levels in peak noise directions. The limitations in acoustic analogy theories in accurately predicting turbulent mixing noise have lead researchers to investigate alternative methods of supersonic jet noise modeling which better encapsulate the effects of noise at peak noise directivity angles.

2.2.2 Stochastic Instability Wave and Wavepacket Models

The mounting experimental evidence for the presence of large-scale coherent turbulent structures in the shear layers of supersonic jets prompted some researchers to explore methods for modeling the turbulence structures instead of replacing them with equivalent source terms. This lead to the development of instability wave and wavepacket theories to model the large-scale turbulence field which were then used to predict the far-field radiated sound.

The wavy wall analogy states that statistically, the large scale turbulent structures in a free shear layer are the same as instability waves. The wavy walls which model the turbulent structures are made up of an infinite series of azimuthal modes which each have a discrete frequency and wavenumber and convect at a constant wave speed. If the phase speed of the wavy wall is faster than the ambient speed of sound, intense Mach wave radiation will be emitted. The angle of the highest intensity noise radiation is computed from the Mach angle relation, $\theta = \cos^{-1}(1/M_c)$ (with $\theta = 0°$ being the forward flight direction) [34].

In observing the nature of the coherent structures that were found in the shear layers of supersonic jet flows, it was found that the spreading rate of the shear layers were weak functions of axial distance in the developmental region. As a consequence, it could be assumed that, locally, changes in the turbulence statistics were negligible axially in space and in time. Under this assumption, the shear layer is in a quasi-equilibrium state, which allows for fluctuations about the mean flow to be statistically modeled as a superposition of wave modes.

The developmental region of supersonic jet flows is observed to be self-similar and have no natural initial length and time scale which means that any variables which have a length or time component will scale proportionally to the axial distance from the nozzle, x, or axial distance divided by the jet velocity x/U_j respectively. This characteristic of jet shear layers allows for the pressure field predicted from the instability wave model to be statistically ensemble averaged. The aforementioned observations led to the development of the model presented in Eq. 4 by Tam & Chen (1979), where p is the local pressure, $a_n(\omega)$ is the instability wave amplitude, n is the azimuthal mode number, ω is the angular frequency, $\hat{p}$ is the instability wave eigenfunction, $\theta_n = \int_0^x k_n(x,\omega)dx$, $k_n(x,\omega)$ is wavenumber, $r_{0.5}$ is the radial location in the shear layer where the local mean velocity is half of the centerline mean velocity, and $r, \theta, x,$ and t are the independent variables for the radial, azimuthal, axial, and time coordinates respectively. The instability wave amplitude is dependent on the area of the of two-point pressure correlation function. Additional improvements to the model were developed which corrected and extended their usage in various other mixing layer and jet flows [3,11,35–41].

$$p(r,\phi,x,t) = \sum_{n=-\infty}^{\infty} \int \frac{a_n(\omega)\,\hat{p}_n(r,x,\omega)}{|\hat{p}_n(r_{0.5},0,\omega)|} e^{i(\theta_n + n\phi - \omega t + \pi/2)}\, d\omega \qquad (4)$$

The model presented in Eq.4 has limitations caused by the fact that the equation was derived using local stability theory. Under this assumption, the multiple-scales expansion was shown to be invalid outside of the jet flow [42]. To extend the solution to predict far-field noise, a global solution was needed and was derived by Tam & Burton [36], who used the method of matched asymptotic expansions to compute the correct far-field pressure. Essentially, the matched asymptotic expansions method used the stochastic instability wave theory as an inner solution to model the jet pressure field and a Fourier transform model as an outer solution to predict the linear acoustic region surrounding the jet. Each of the solutions were computed and the outer boundary of the inner solution was used to set the boundary conditions for the inner boundary of the outer solution to predict the far-field.

Many experimental and numerical investigations have found excellent results in using the instability wave theory to model far-field sound radiated by large-scale turbulent structures from supersonic jets operating over a wide range of jet Mach numbers and temperature ratios [17,38,43,44]. However, for subsonic jets, the theory did not perfectly model the turbulent mixing noise spectra and for supersonic jets, the model did not capture the lowest and highest frequency radiated content.

To address the discrepancies between the instability wave model and experimental data, researchers began to suggest that modifying the instability wave model to account for the growth and decay of instability waves in the developmental region of the supersonic jet [35].The subsequent efforts pursued by researchers to include these variations led to the proliferation of wavepacket theory.

Initially, researchers began incorporating growth and decay parameters into the stochastic instability wave model and initially found better agreement between subsonic jet far-field spectra and experimental data [38,43,45–48]. It was eventually discovered that linear stability theory, the backbone of the stochastic instability wave model, was theoretically incapable of accurately predicting noise at non-peak frequencies for subsonic jets. The inadequacy of the model was due to the absence of nonlinear interactions and not accounting for shear layer growth in the model [49].

Modern wavepacket models follow a similar derivation path as that used for stochastic instability wave models, with the following differences. Instead of using linear stability equations as the foundation, parabolic stability equations are used which allow for the growth of the shear layer to be included in the model. To account for self-similarity in the developmental region of the jet, the root-mean-square pressure of the wavepacket now scales with axial distance from the nozzle times the instability angular wavenumber ($\hat{p}(\alpha x)$).

The majority of the improvements that wavepacket theory brings to jet noise prediction mostly affect subsonic turbulent jets where the convection velocities of the large scale turbulent structures is predominately subsonic. It has been found that, for jets dominated by supersonic phase speed coherent structures, the far-field predictions obtained from wavepacket analysis provide a solution that is nearly identical to the modified instability wave model with a which accounts for small angle flow divergence developed by Tam [34,49].

The success of instability wave and wavepacket models in estimating the large-scale turbulent mixing noise produced by supersonic jets have informed experimental and computational scientists that reducing convection velocity and/or the two-point fluctuating pressure correlations of the large-scale structures in the turbulence plume is the key to reducing jet noise. The following section will discuss the noise control techniques developed over the years for supersonic and high-subsonic jets and how each technique impacts the aforementioned parameters in favorable ways.

2.3 Methods for Jet Noise Suppression

The goal of jet noise research is to identify and understand the fundamental physical mechanisms which cause efficient sound radiation and to develop techniques to reduce the noise. In the previous section, the low-order models which are used to predict the far-field sound pressure were presented. From those models, the key turbulence parameters which most affect the large-scale turbulence mixing noise radiated from supersonic jets were identified. From the findings, many active and passive jet noise control techniques have been developed by engineers and scientists for both subsonic and supersonic jet flows. In studying the fluid dynamic and acoustic changes caused by the noise control modifications, the physical changes that occur within the jet turbulence plumes which lead to favorable or adverse noise augmentation can be identified.

2.3.1 Nozzle and Engine Modifications

Modifications to the nozzle geometry have been established as an effective method to reduce jet noise emitted by subsonic commercial jets by changing the turbulence characteristics which form in the jet shear layer. Chevrons are saw-tooth like patterns manufactured into the lip of the nozzle exhaust which serve to increase mixing near the nozzle exhaust by inducing the formation of stream-wise vortices. They are widely used in subsonic commercial subsonic jets as a method for reducing emitted jet noise. The vortices impact low-frequency noise content, reducing the overall sound pressure level (OASPL) of far-field radiated sound. However, when chevrons interact with higher speed flow, the increase in turbulent mixing causes an increase in high frequency turbulent mixing noise. Additionally, in imperfectly expanded supersonic flows, the enhanced mixing results in a substantial increase of broadband shock associated noise (BBSAN), which negates nearly all of the benefits obtained from the reduction of large-scale mixing noise [50].

Increasing the bypass ratio of subsonic turbofan jets has resulted in a significant reduction in turbulent mixing noise. So much so, that the interaction between the jet turbulence plume and the trailing edge of the wing it is mounted upon generates more noise. Increased bypass ratios reduce turbulence self-noise in subsonic commercial jets by increasing the mass flow rate through the slower bypass and decreasing the mass flow rate through the jet core while increasing or maintaining the same level of thrust as older turbofan engines. The alterations to the engine design were initially driven by the desire for increased fuel efficiency. Luckily, the decreased jet velocity resulted in a large acoustic benefit, as the emitted sound from convected turbulent eddies scale with the eighth power of the convection velocity [18]. However, as nearly all supersonic jets currently in operation are for military purposes, engine performance is prioritized over efficiency and thus, the turbofans still maintain small bypass ratios. Additionally, the afterburners installed on many tactical aircraft produce significant noise by substantially increasing the flow velocity of the jet plume.

2.3.2 Fluid Injections

Fluid injections have been studied for years as a method for reducing jet noise. Fluid injections are a technique where a series of micro-jets are mounted either inside or outside of the nozzle and inject fluid into the jet plume/boundary layer. Liquid injections into gaseous jet flows have been investigated in the past and are highly effective in reducing noise produced by rockets. Aqueous injections affect noise production by decreasing the jet plume temperature and velocity through evaporation and momentum transfer between the jet and the injected water.

However, in air-breathing engine applications, the large volumes of water and high injection pressures required to achieve notable sound reductions make real world application of the system economically unviable [51].

Gaseous injections, while less effective than aqueous injections, have proven to be a more feasible injection method for controlling noise emissions from subsonic and supersonic jet flows. Gaseous injections produce noise reductions by introducing stream-wise vorticity into the jet plume which promotes rapid mixing near the nozzle which inhibits the formation of coherent structures. The modifications made to the turbulence have a beneficial effect on all three modes of supersonic noise production, with proper implementation of active control schemes for the injected gas. Injection of air into single and multi-stream high-subsonic and supersonic jet flows have produced far-field noise reduction of up to 5 dB in laboratory scale jets [52–55]. Application of fluidic injections in real engines will have an impact on performance, as to supply the required air for injections, bleed air will most likely need to be pulled from the jet compressor.

2.3.3 Axisymmetric and Asymmetric Multi-Stream Jets

Asymmetric multi-stream jets have been investigated in recent years as a potential method for reducing jet noise. In asymmetric round multi-stream jets, instead of the core and bypass jet nozzles being concentric with one another, one of the nozzle is radially shifted such that the nozzles are eccentric. The shift in the relative nozzle positions alters the velocity profile of the jet. The geometric augmentation results in a reduction of the potential core length of the core jet flow and global changes to turbulent mixing in the outer shear layer of the bypass jet flow. The changes serve to decrease peak radiated turbulent mixing noise levels at azimuthal angles where the bypass jet velocity is reduced. Experimental evidence suggests that the noise benefit is due to a reduction in convection velocities of the large scale turbulence structures [56]. Unfortunately, the noise levels are considerably increased on the opposing side of the asymmetric jet, where the bypass velocity has increased due to the reduction in the nozzle exit area [57,58].

Another technique to reduce noise levels in supersonic multi-stream jet flows are inverted velocity profile (IVP) jets. While most multi-stream jets are operated with so-called normal velocity profiles (NVP), where the core jet stream has higher axial velocities than the bypass stream, IVP jets redistribute the bypass and core streams such that the core flow velocity is less than the bypass flow. Far-field acoustic studies on NVP and IVP jets have shown that IVP jets produce less noise than NVP jets for a range of conditions when both jets have the same effective mass flow rates, thrust, and exit areas [59–66]. Since the exit areas are matched for these jets, the core stream in an NVP jet must have a higher velocity and the IVP jet a lower velocity than their fully-mixed equivalent jet baseline. The noise reductions achieved can be attributed to the reduction in the outer bypass mean velocity. The lower mean speed of the outside jet plume causes a reduction in convection velocities of the large scale turbulence structures in the bypass-to-ambient shear layer. While the noise benefits obtained were substantial using IVP jets, the practical application of such a technique in tactical aircraft is nearly impossible due to the impact on vehicle performance and the incredible engineering challenges which need to be overcome in designing and developing an engine where the outer fan stream operates at a higher velocity than the core.

While the IVP technique for noise reduction in supersonic jets is impractical, the lessons learned from such a technique can still be applied to tactical air vehicles. By introducing a lower temperature flow stream into an otherwise heated supersonic jet flow, it is hypothesized that localized or global reductions in radiated jet noise can be achieved. By locating the temperature non-uniformity in the center of the jet core, global reductions in peak jet noise can be achieved, similar to that achieved in IVP jets. If the temperature reduction is offset, it is hypothesized that localized reductions can be obtained at specific azimuthal angles. To achieve the desired results in tactical afterburning aircraft, fuel nozzles within the afterburner can be turned on or off at azimuthal locations where emitted noise reductions are desired. While during flight, the loss of additional thrust is not ideal, the technique can be implemented during takeoff from aircraft carriers which may significantly reduce service crew's exposure time to the intense noise.

The use of total temperature non-uniformities in a heated jet is the noise reduction concept being investigated in the current study. Due to the efforts put forth by the current author and collaborators [67–71] at Virginia Tech, other researchers in the jet noise community have begun investigating the viability of applying the technique and have obtained similar or better results with higher velocity jet flows operating at larger temperature ratios [72].

2.4 Compressible Shear Layer Characteristics

In order to influence the convection velocity and two-point correlations of the large-scale turbulent structures in jet flows, it is important to understand how shear layers form and evolve both spatially and temporally. In this section, an overview of compressible shear layer characteristics will be given.

A shear layer is a region of viscous fluid that occurs when a velocity gradient exists. Free shear layers form at the interface of two or more parallel streams of viscous fluid that are moving at different velocities in the absence solid boundaries. Profiles of the axial velocity of free shear layers always contain an inflection point that occurs which indicate inherent instability in the flow. The dominant large scale instabilities present in free shear layers manifest themselves as instability waves which grow with axial distance from the source of the flow, the most common of which is the Kevin-Helmholtz instability. For round jets, the near-nozzle growth of the shear layer can be scaled in the same manner as a mixing layer as long as the thickness of the shear layer, δ, is much smaller than the radius, r, of the jet nozzle orifice. Figure 2.1 shows a diagram of a typical mixing layer.

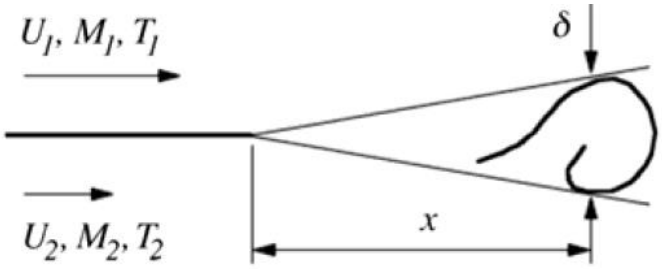

Figure 2.1. Diagram of a mixing layer

As mentioned in Section 2.2.2 of the literature review, the instability waves are equivalent to the large-scale turbulent structures in the context of turbulent mixing noise analysis. In the developmental region of the jet, the flow properties are self-similar, which means that the profiles all scale with the local velocity and length scales in the shear layer (The local velocity scale of the shear layer is the velocity difference between the two free streams, $\Delta U = U_1 - U_2$, and the local length scale is the thickness of the layer, δ). Due to the self-similarity of the flow and the lack of intrinsic scales in the mixing layer, only changes in the relative properties between the two streams matter.

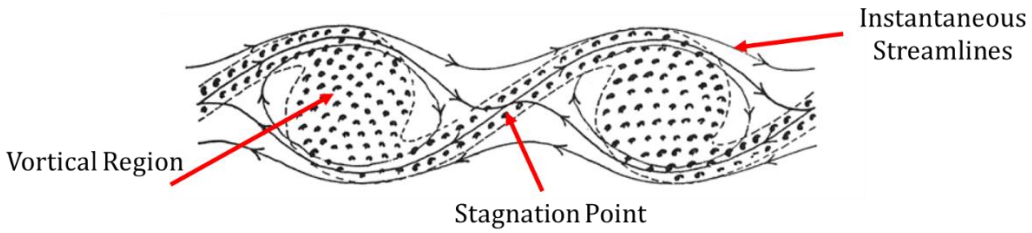

Figure 2.2. Diagram of a subsonic, compressible, two-dimensional periodic mixing layer. (Image modified from Corcos and Sherman [73]**)**

At this point, the convection Mach number must be defined prior to discussing scaling, the analysis presented here being summarized from Smits & Dussauge [74]. Starting with a two-dimensional subsonic, compressible, and periodic mixing layer, (like the one shown in Figure 2.2) a frame of reference is selected which moves with two eddies and impose the following assumptions: two-non-dispersive vortical eddies, constant convection velocity of the eddy, variable density, and a fixed stagnation point between two vortices maintaining a fixed distance from one another. At the stagnation point, the pressures for both eddies are the same (Eq. 5). p is the pressure, M_c is the convection Mach number for each eddy, and γ is the adiabatic ratio.

$$p_1 = p_2 \rightarrow \left(1 + \frac{\gamma_1 - 1}{2} M_{c1}^2\right)^{\gamma_1/(\gamma_1 - 1)} = \left(1 + \frac{\gamma_2 - 1}{2} M_{c2}^2\right)^{\gamma_2/(\gamma_2 - 1)} \tag{5}$$

For shock-free supersonic mixing layers, the evolution of the event along the streamlines can be considered isentropic if the eddy turnover time is much larger than the fluid travel time along the streamlines from the external parts of the flow to the stagnation point (Eq. 6).

$$\frac{\sqrt{k}}{\Delta U}\frac{\delta}{\Lambda} \ll 1 \tag{6}$$

For the case where both gasses are the same ($\gamma_1 = \gamma_2$), and the same convection Mach number for each eddy is assumed ($M_{c1} = M_{c2} = M_c$), the convection Mach number and velocity is derived (Eqs. 7 and 8). It is important to note that the convection velocity derived here is not necessarily the same as those obtained from two-point space time correlations on experimental and computational data.

$$M_c = \frac{\Delta U}{c_1 + c_2} \tag{7}$$

$$U_c = \frac{c_2 U_1 + c_1 U_2}{c_1 + c_2} \tag{8}$$

Extensive research into the mean flow and Reynolds shear stress scaling of compressible mixing layers has been conducted over the years [74–80]. Brown and Roshko [75] proposed the following mean flow scaling for subsonic shear layer growth rates by assuming the convective time scale for large scale turbulence, t_c, is the same order as the turbulence diffusion time scale, t_t, so that (Eqs. 9-11),

$$t_c \sim \frac{x}{U_c} \tag{9}$$

$$t_t \propto \frac{1}{\partial U/\partial y} \sim \frac{\delta}{\Delta U} \tag{10}$$

$$t_c = t_t, \frac{\delta}{x} \propto \frac{\Delta U}{U} \tag{11}$$

The scaling shows that spreading rate of a mixing layer is inversely proportional to U_c. Papamoschou and Roshko [76] extended the scaling to encompass compressible mixing layers by including velocity, q, and density ratio, s, effects as well as adding a normalized spreading function $\Phi(M_c)$ which is determined from experimental or computational data (Eq. 12). Despite the fact that the formulation above was developed for temporal growth, it can be derived identically for spatial growth, with the only difference being a change in the normalized spreading function used $\Phi(s, q)$.

$$\frac{\partial \delta}{\partial x} = \left(\frac{\partial \delta}{\partial x}\right)_{U_2=0} \frac{(1-q)\left(1+\sqrt{s}\right)}{2\left(1+q\sqrt{s}\right)} \Phi(M_c) \tag{12}$$

Scaling of the Reynolds shear stress has also been pursued using the scaling convection velocity as a basis. Barre et al. [79] developed a method for determining the scales of the Reynolds stresses. The time scale for the coherent turbulent eddies can be hypothesized as (Eq. 13),

$$t_t \sim \frac{\delta^2}{\nu_t}, \tag{13}$$

Assuming the turbulent viscosity is constant radially allows results in (Eq. 14),

$$\nu_t = \frac{\overline{u_x' u_r'}}{\partial U/\partial y} \propto \frac{u_\tau^2 \delta}{\Delta U}, \tag{14}$$

where u_τ^2 is the maximum shear stress, and ultimately leads to (Eq. 15),

$$t_t \sim \frac{\delta \Delta U}{u_t^2}. \tag{15}$$

Recalling that $x = U_c t$, we find that the transverse growth rate of the eddies grows linearly with axial distance (Eq. 16),

$$\frac{d\delta}{dx} = \frac{1}{K(s,q,M_c)} \frac{u_t^2}{U_c \Delta U'} \tag{16}$$

where $K(s, q, M_c)$ is an empirical function which accounts for density, velocity, and convective Mach number changes.

Papamoschou & Roshko [76] developed the relationship for the Reynolds shear stress growth rate given in Eq. 17.

$$\frac{d\delta}{dx} = \frac{1}{2}\left(\frac{\partial \delta}{\partial x}\right)_{U_2=0} \Phi(M_c) \frac{\Delta U}{U}. \tag{17}$$

Using the scaling in Eq. 17 along with the time scale hypothesis from Barre et al [79] results in Eq. 18.

$$\frac{u_t^2}{(\Delta U)^2} = \frac{1}{2} K(s, q, M_c) \left(\frac{\partial \delta}{\partial x}\right)_{U_2=0} \Phi(M_c). \tag{18}$$

K being a function of M_c implies that the scaling applies to both self-preserving and developing shear layers, though the K function is empirical and must be defined for each flow case to best fit the data. The Papamoschou & Roshko [76] formulation implies that if there is a weak dependence of M_c in the K function, the maximum shear stress will still vary based on the dimensionless spreading function, $\Phi(M_c)$, which does not occur in the Barre scaling. Also of note, since the Reynolds shear stress depends on M_c, the eddy viscosity will also depend on M_c. Thus, in free shear flows, the eddy viscosity scales as, $v_t = C\Phi(M_c)\Delta U \delta(x)$, where C is a constant.

The scaling analysis presented reveals that the two major variables which affect compressible shear layer development are the velocity ratio, density ratio, and the convection Mach number. In jet flows where the co-flowing streams are the same fluid (i.e. air), the first two parameters directly influence the convection velocity of the large scale turbulent structures. By introducing a cold secondary plume into a heated supersonic jet, the turbulence development in the shear layer of the jet can be manipulated to reduce the convection velocity and increase turbulent mixing which can favorably impact radiated noise.

2.5 Concluding Remarks

The literature review presented has established that, for supersonic jets, large scale coherent turbulent structures which propagate at supersonic phase speeds are responsible for the majority of turbulent mixing noise. The most important fluid dynamic variables which affect turbulent mixing noise generated by supersonic jets are the convection velocity and the two-point pressure correlation in the turbulence plume, and reducing the convection speed or the correlation will reduce the intensity of radiated sound. The readily tunable properties which engineers have access to that affect the aforementioned properties are the temperature ratio, velocity ratio, and the nozzle geometry.

Many noise suppression techniques have been investigated to control jet noise emission, such as fluid injections, chevrons, asymmetric multi-stream jets, inverted velocity profile jets, and total-temperature non-uniformities. All of the noise control schemes impact the turbulence plume in ways which either reduce the convection velocities of or de-correlate the turbulence in the developmental region of the jet plume. When applied to supersonic jets, all of the techniques present unique benefits and drawbacks which limit their applicability to full-scale engines used for tactical aircraft.

The studies presented in sections 3 and 4 investigate introducing a total temperature non-uniformity to a heated supersonic jet, a novel technique for noise reduction. The technique impacts the development of large scale coherent turbulent structures by affecting the convection velocity and changing the three dimensional structure. Practical

implementation of the technique into full-scale afterburning jet engines can be achieved by controlling which fuel nozzles are activated during takeoff and flight.

References

[1] Ribner, H. S., "Cylindrical Sound Wave Generated by Shock-Vortex Interaction," AIAA J., 23(11), pp. 1708–15.

[2] Harper-Bourne, M., and Fisher, M. J., 1973, "The Noise from Shock Waves in Supersonic Jets."

[3] Tam, C. K. W., 1987, "Stochastic Model Theory of Broadband Shock Associated Noise from Supersonic Jets," J. Sound Vib., 116(2), pp. 265–302.

[4] Norum, T. D., 1983, "Screech Suppression in Supersonic Jets," AIAA J., 21(2), pp. 235–240.

[5] Powell, A., 1953, "The Noise of Choked Jets," J. Acoust. Soc. Am., 25(3), pp. 385.

[6] Sherman, P. M., Glass, D. R., and Duleep, K. G., 1976, "Jet Flow Field during Screech," Appl. Sci. Res., 32(3), pp. 283–303.

[7] Westley, R., and Woolley, J., 1975, "The near Field Sound Pressures of a Choked Jet When Oscillating in the Spinning Mode," *2nd Aeroacoustics Conference*.

[8] Rosfjord, T. J., and Toms, H. L., 1975, "Recent Observations Including Temperature Dependence of Axisymmetricjet Screech," AIAA J., 13(10), pp. 1384–1386.

[9] Seiner, J., Manning, J., and Ponton, M., 1987, "Model and Full Scale Study of Twin Supersonic Plume Resonance," *25th AIAA Aerospace Sciences Meeting*.

[10] Tam, C. K. W., 1988, "The Shock-Cell Structures and Screech Tone Frequencies of Rectangular and Non-Axisymmetric Supersonic Jets," J. Sound Vib., 121(1), pp. 135–147.

[11] Morris, P. J., Giridharan, M. G., and Lilley, G. M., 1990, "On the Turbulent Mixing of Compressible Free Shear Layers," Proc. R. Soc. London A Math. Phys. Eng. Sci., 431(1882).

[12] Mollo-Christensen, E., 1967, "Jet Noise and Shear Flow Instability Seen From an Experimenter's Viewpoint," J. Appl. Mech., 34(1), pp. 1.

[13] Yu, J. C., and Dosanjh, D., 1971, "Noise Field of Coaxial Interacting Supersonic Jet Flows," *9th Aerospace Sciences Meeting*.

[14] Tanna, H. K., 1977, "An Experimental Study of Jet Noise Part I: Turbulent Mixing Noise," J. Sound Vib., 50(3), pp. 405–428.

[15] Lau, J. C., Morris, P. J., and Fisher, M. J., 1979, "Measurements in Subsonic and Supersonic Free Jets Using a Laser Velocimeter," J. Fluid Mech., 93(01), pp. 1.

[16] Norum, T. D., and Seiner, J. M., 1982, "Measurements of Mean Static Pressure and Far Field Acoustics of Shock Containing Supersonic Jets."

[17] Seiner, J. M., Ponton, M. K., Jansen, B. J., and Lagen, N. T., 1992, "The Effects of Temperature on Supersonic Jet Noise Emission," *DGLR/AIAA 14th Aeroacoustics Conference*.

[18] Lighthill, M. J., 1952, "On Sound Generated Aerodynamically. I. General Theory," Proc. R. Soc. A Math. Phys. Eng. Sci., 211(1107), pp. 564–587.

[19] Lighthill, M. J., 1954, "On Sound Generated Aerodynamically. II. Turbulence as a Source of Sound," Proc. R. Soc. A Math. Phys. Eng. Sci., 222(1148), pp. 1–32.

[20] Curle, N., 1955, "The Influence of Solid Boundaries upon Aerodynamic Sound," Proc. R. Soc. London. Ser. A. Math. Phys. Sci., 231(1187), pp. 505–514.

[21] Williams, J. E. F., 1963, "The Noise from Turbulence Convected at High Speed," Philos. Trans. R. Soc. A Math. Phys. Eng. Sci., 255(1061), pp. 469–503.

[22] FFowcs Williams, J. E., and Hawkings, D. L., 1969, "Sound Generation by Turbulence and Surfaces in Arbitrary Motion," Philos. Trans. R. Soc. A Math. Phys. Eng. Sci., 264(1151), pp. 321–342.

[23] Proudman, I., 1952, "The Generation of Noise by Isotropic Turbulence," Proc. R. Soc. London A Math. Phys. Eng. Sci., 214(1116).

[24] Ribner, H. S., 1969, "Quadrupole Correlations Governing the Pattern of Jet Noise," J. Fluid Mech., 38(01), pp. 1.

[25] Balsa, T. F., and Gliebe, P. R., 1977, "Aerodynamics and Noise of Coaxial Jets," AIAA J., 15(11), pp. 1550–1558.

[26] Lilley, G. M., 1996, "Radiated Noise from Isotropic Turbulence with Applications to the Theory of Jet Noise," J. Sound Vib., 190(3), pp. 463–476.

[27] Khavaran, A., 1999, "Role of Anisotropy in Turbulent Mixing Noise," AIAA J., 37(7), pp. 832–841.

[28] Davies, P. O. A. L., Fisher, M. J., and Barratt, M. J., 1963, "The Characteristics of the Turbulence in the Mixing Region of a Round Jet," J. Fluid Mech., 15(3), pp. 337–367.
[29] Chu, W. T., 1966, "Turbulence Measurements Relevant to Jet Noise," J. Acoust. Soc. Am., 39(6), pp. 1250–1250.
[30] Karabasov, S. A., Afsar, M. Z., Hynes, T. P., Dowling, A. P., McMullan, W. A., Pokora, C. D., Page, G. J., and McGuirk, J. J., 2010, "Jet Noise: Acoustic Analogy Informed by Large Eddy Simulation," AIAA J., 48(7), pp. 1312–1325.
[31] Atvars, J., and Ribner, H., 1965, "Refraction of Sound from a Point Source Placed in an Air Jet," *2nd Aerospace Sciences Meeting*.
[32] Phillips, O. M., 1960, "On the Generation of Sound by Supersonic Turbulent Shear Layers," J. Fluid Mech., 9(01), p. 1.
[33] Lilley, G. M., 1972, "The Generation and Radiation of Supersonic Jet Noise. Volume I. Summary," I (AFAPL-TR-72-53).
[34] Tam, C. K. W., 1995, "Supersonic Jet Noise," Annu. Rev. Fluid Mech., 27(1), pp. 17–43.
[35] Tam, C. K. W., and Burton, D. E., 1984, "Sound Generated by Instability Waves of Supersonic Flows. Part 1. Two-Dimensional Mixing Layers," J. Fluid Mech., 138(1), p. 249.
[36] Tam, C. K. W., and Burton, D. E., 1984, "Sound Generated by Instability Waves of Supersonic Flows. Part 2. Axisymmetric Jets," J. Fluid Mech., 138(1), p. 273.
[37] Viswanathan, K., and Morris, P. J., 1992, "Predictions of Turbulent Mixing in Axisymmetric Compressible Shear Layers," AIAA J., 30(6), pp. 1529–1536.
[38] Tam, C. K. W., and Chen, P., 1994, "Turbulent Mixing Noise from Supersonic Jets," AIAA J., 32(9), pp. 1774–1780.
[39] Plaschko, P., 1981, "Stochastic Model Theory for Coherent Turbulent Structures in Circular Jets," Phys. Fluids, 24(2), p. 187.
[40] Plaschko, P., 1983, "Axial Coherence Functions of Circular Turbulent Jets Based on an Inviscid Calculation of Damped Modes," Phys. Fluids, 26(9), p. 2368.
[41] Liou, W. W., and Morris, P. J., 1992, "Weakly Nonlinear Models for Turbulent Mixing in a Plane Mixing Layer," Phys. Fluids A Fluid Dyn., 4(12), pp. 2798–2808.
[42] Tam, C. K. W., and Morris, P. J., 1980, "The Radiation of Sound by the Instability Waves of a Compressible Plane Turbulent Shear Layer," J. Fluid Mech., 98(02), p. 349.
[43] Troutt, T. R., and McLaughlin, D. K., "Experiments on the Flow and Acoustic Properties of a Moderate-Reynolds-Number Supersonic Jet," J. Fluid Mech., 116, pp. 123–56.
[44] Viswanathan, K., 2004, "Parametric Study of Noise from Dual-Stream Nozzles," J. Fluid Mech., 521, pp. 35–68.
[45] Tam, C. K. W., and Hu, F. Q., 1989, "On the Three Families of Instability Waves of High-Speed Jets," J. Fluid Mech., 201(1), p. 447.
[46] Balakumar, P., 1998, "Prediction of Supersonic Jet Noise," *36th AIAA Aerospace Sciences Meeting and Exhibit*.
[47] Lin, R.-S., Reba, R. A., Narayanan, S., Hariharan, N. S., and Bertolotti, F. P., 2004, "Parabolized Stability Equation Based Analysis of Noise From an Axisymmetric Hot Jet," *Volume 1*, ASME, pp. 799–804.
[48] Piot, E., Casalis, G., Muller, F., and Bailly, C., 2006, "Investigation of the PSE Approach for Subsonic and Supersonic Hot Jets. Detailed Comparisons with LES and Linearized Euler Equations Results," Int. J. Aeroacoustics, 5(4), pp. 361–393.
[49] Jordan, P., and Colonius, T., 2013, "Wave Packets and Turbulent Jet Noise," Annu. Rev. Fluid Mech., 45(1), pp. 173–195.
[50] Rask, O., Kastner, J., and Gutmark, E., "Understanding How Chevrons Modify Noise in a Supersonic Jet with Flight Effects," AIAA J., 49(8), pp. 1569–76.
[51] Henderson, B., 2010, "Fifty Years of Fluidic Injection for Jet Noise Reduction," Int. J. Aeroacoustics, 9(1–2), pp. 91–122.
[52] Arakeri, V. H., Krothapalli, A., Siddavaram, V., Alkislar, M. B., and Lourenco, L. M., 2003, "On the Use of Microjets to Suppress Turbulence in a Mach 0.9 Axisymmetric Jet," J. Fluid Mech., 490.
[53] Krothapalli, A., Arakeri, A., Greska, B., Joseph, T., and Arakeri, V. H., 2002, "High Speed Jet Noise Reduction Using Microjets," *8th AIAA/CEAS Aeroacoustics Conference & Exhibit*.
[54] Alkislar, M. B., Krothapalli, A., and Butler, G. W., 2007, "The Effect of Streamwise Vortices on the Aeroacoustics of a Mach 0.9 Jet," J. Fluid Mech., 578, pp. 139.
[55] Powers, R. W., Kuo, C.-W., and McLaughlin, D. K., 2013, "Experimental Comparison of Supersonic Jets

Exhausting from Military Style Nozzles with Interior Corrugations and Fluidic Inserts," *19th AIAA/CEAS Aeroacoustics Conference*.
[56] Stuber, M., Lowe, T., and Ng, W., 2018, "Synthesis of Convection Velocity and Turbulence Measurements in Three-Stream Jets."
[57] Henderson, B. S., Leib, S. J., and Wernet, M. P., 2015, "Measurements and Predictions of the Noise from Three-Stream Jets," *21st AIAA/CEAS Aeroacoustics Conference*.
[58] Papamoschou, D., 2018, "Modelling of Noise Reduction in Complex Multistream Jets," J. Fluid Mech., 834, pp. 555–599.
[59] Tanna, H. K., and Tester, B. J., 1979, *The Noise and Flow Characteristics of Inverted-Profile Coannular Jets*, Marietta, GA.
[60] Tanna, H. K., 1980, "Coannular Jets—Are They Really Quiet and Why?," J. Sound Vib., 72(1), pp. 97–118.
[61] Tanna, H. K., and Morris, P. J., 1985, "The Noise from Normal-Velocity-Profile Coannular Jets," J. Sound Vib., 98(2), pp. 213–234.
[62] Maus, J. R., Goethert, B. H., and Sundaram, C. V., 1981, "Noise Characteristics of Coannular Flows with Conventional and Inverted Velocity Profiles," J. Aircr., 18(2), pp. 135–141.
[63] Dahl, M. D., and Morris, P. J., 1997, "Noise from Supersonic Coaxial Jets, Part 1: Mean Flow Predictions," J. Sound Vib., 200(5), pp. 643–663.
[64] Dahl, M. D., and Morris, P. J., 1997, "Noise from Supersonic Coaxial Jets, Part 2: Normal Velocity Profile," J. Sound Vib., 200(5), pp. 665–699.
[65] Dahl, M. D., and Morris, P. J., 1997, "Noise from Supersonic Coaxial Jets, Part 3: Inverted Velocity Profile," J. Sound Vib., 200(5), pp. 701–719.
[66] Dahl, M., and Morris, P. J., 1994, "Noise Radiation by Instability Waves in Coaxial Jets," *25th AIAA Fluid Dynamics Conference*, AIAA, Colorado Springs, CO.
[67] Quinn, A. M., Daniel, K., Lowe, K. T., and Ng, W., 2019, "Outdoor Acoustic Measurements of the Virginia Tech Heated Supersonic Jet Rig Using Ground Microphones," *AIAA Scitech 2019 Forum*.
perimental Investigation of the Very Near Pressure Field of a Heated Supersonic Jet with a Total Temperature Non-Uniformity," *2018 AIAA/CEAS Aeroacoustics Conference*.
[68] Daniel, K. A., Mayo Jr., D. E., Lowe, K. T., and Ng, W. F., 2019, "Use of Thermal Non-Uniformity to Reduce Supersonic Jet Noise," AIAA J.
[69] Daniel, K., Mayo, D., Lowe, K. T., and Ng, W., 2019, "Experimental Investigation on the Acoustic Field and Convection Velocity of Structures in a Heated Jet With Centered Thermal Non-Uniformity," *AIAA Scitech 2019 Forum*.
[70] Daniel, K., Mayo, D. E., Lowe, T., and Ng, W., 2018, "Experimental Investigation of the Very Near Pressure Field of a Heated Supersonic Jet with a Total Temperature Non-Uniformity," *2018 AIAA/CEAS Aeroacoustics Conference*.
[71] Tamm P, Bres GA, Towne A, L. S., Tamm, P., Bres, G. A., Towne, A., and Lele, S. K., 2018, "Leveraging Large-Eddy Simulations to Investigate the Influence of Temperature Non-Uniformity on Jet Noise," *Center for Turbulence Research Proceedings of the Summer Program 2018*, pp. 175–184.
[72] Corcos, G. M., and Sherman, F. S., 1976, "Vorticity Concentration and the Dynamics of Unstable Free Shear Layers," J. Fluid Mech., 73(02), p. 241.
[73] Smits, A. J., and Dussauge, J.-P., 2006, *Turbulent Shear Layers in Supersonic Flow*.
[74] Brown, G. L., and Roshko, A., 1974, "On Density Effects and Large Structure in Turbulent Mixing Layers," J. Fluid Mech., 64(04), p. 775.
[75] Papamoschou, D., and Roshko, A., 1988, "The Compressible Turbulent Shear Layer: An Experimental Study," J. Fluid Mech., 197(1), p. 453.
[76] Slessor, M. D., Zhuang, M., and Dimotakis, P. E., 2000, "Turbulent Shear-Layer Mixing: Growth-Rate Compressibility Scaling," J. Fluid Mech., 414, pp. 35–45.
[77] Dimotakis, P. E., 1986, "Two-Dimensional Shear-Layer Entrainment," AIAA J., 24(11), pp. 1791–1796.
[78] Barre, S., Quine, C., and Dussauge, J. P., 1994, "Compressibility Effects on the Structure of Supersonic Mixing Layers: Experimental Results," J. Fluid Mech., 259, pp. 47–78.
[79] Dimotakis, P. E., 1991, "Turbulent Free Shear Layer Mixing and Combustion," *High-Speed Flight Propulsion Systems*, American Institute of Aeronautics and Astronautics, Washington DC, pp. 265–340.

The Mean Flow and Turbulence Characteristics of a Heated Supersonic Jet with an Offset Total Temperature Non-Uniformity

David E. Mayo Jr,[1] Kyle E. Daniel,[2] K. Todd Lowe,[3] Wing F. Ng[4]
Advanced Propulsion and Power Laboratory, Virginia Tech, Blacksburg, VA, 24060, USA

An experimental investigation of the mean flow and turbulence characteristics of two Mach 1.5 heated jets, one with a uniform temperature profile and another with an offset non-uniform temperature profile, is presented. The thermal non-uniformity is generated by introducing a matched static pressure stream of low temperature air into the subsonic, converging section of a round contoured supersonic nozzle. The secondary plume, which is offset radially from the geometric centerline of the round jet nozzle, produces a jet with an altered velocity profile, modifying the turbulence throughout the jet plume. On the side of the jet where the cooler stream is introduced, the near-nozzle peak velocity is reduced to 83% of the heated jet exit velocity, associated with a reduction in the measured peak turbulent stress levels in the region between three to six jet diameters from the nozzle exit. Several aspects of the mean flow and turbulence structure in the developing plume with temperature non-uniformity are similar to those seen in multi-stream co-annular round jets with offset nozzles, indicating that alternative engineering approaches may be available for generating the characteristics of offset plumes desirable for jet noise reduction.

Nomenclature

D = Primary Jet Exit Diameter (m)

d = Secondary Jet Exit Diameter (m)

F = Isentropic Jet Thrust (N)

[1] Graduate Research Assistant, Department of Mechanical Engineering, AIAA Student Member
[2] Graduate Research Assistant, Department of Aerospace and Ocean Engineering, AIAA Student Member
[3] Associate Professor, Department of Aerospace and Ocean Engineering, AIAA Associate Fellow
[4] Christopher C. Kraft Endowed Professor, Department of Mechanical Engineering, AIAA Associate Fellow

M = Mach Number

$\dot{m}$ = Mass Flow Rate (kg/m^3)

Re = Jet Reynolds Number, $\rho U_j D/\mu$

T = Temperature (K)

t_0 = Relaxation Time (sec)

U = Velocity (m/s)

u' = Fluctuating Velocity (m/s)

x = Jet Axial Coordinate Axis (m)

y = Jet Transverse Coordinate Axis (m)

Δt = PIV Inter-Frame Time Delay (sec)

μ = Dynamic Viscosity ($kg/m\ s$)

ρ = Density (kg/m^3)

Subscripts

j = Uniform Jet Heated Plume Condition at Nozzle Exit

p = Thermally Offset Jet Primary Stream Condition at Nozzle Exit

part. = Particle

s = Thermally Offset Jet Secondary Stream Condition at Nozzle Exit

x = Axial Component

y = In-plane Transverse Component

I. Introduction

Reducing jet noise produced by afterburning tactical aircraft during take-off and landing is of great interest due to health risks that flight support personnel undertake from long-term exposure to this harsh environment [1]. Achieving this goal requires research into supersonic jet noise reduction concepts, while relying heavily upon analyses of the mean and unsteady flow fields that produce the intense sources of acoustic noise. In the current work, the mean flow and turbulence structure of a jet with an intentionally introduced temperature non-uniformity are scrutinized for similarities to other concepts known to reduce noise from high speed jets.

Previous studies have revealed measureable alterations in radiated jet noise by modifying the exit conditions of the jet flow, thereby modulating the turbulence scales and development in the jet shear layer (e.g., [2-13]). Existing methods for generating non-uniform jet exit conditions include fluid injections and inserts [2-5], multi-stream axisymmetric and asymmetric jets [6-8], inverted velocity profile jets (IVP) [9-13], and thermally non-uniform jets—the topic of the current work.

Fluid injection is an attempt to induce small-scale instabilities into the jet shear layer to promote faster mixing of the large-scale coherent turbulent structures. This is achieved by blowing compressed air into the shear layer—just beyond the nozzle lip [2–4] or into the diverging section of a supersonic jet nozzle [5]. The former method has been shown to increase entrainment in the shear layer, while the latter induces the formation of stream-wise vortices in the shear layer. Both methods lead to significant decreases in far-field noise in the peak radiation direction.

Multi-stream axisymmetric and asymmetric jets have been studied in recent years, showing promise for jet noise reduction. Recent studies [6–8] have indicated that asymmetric multi-stream jet profiles serve to reduce the potential core length of the primary jet, enhance turbulent mixing in the shear layer region opposite the offset jet plume, reduce convection velocities in this area, and induce the formation of stream-wise vortices. The combination of the aforementioned changes in the global flow field results in observed reductions between 2 and 6 dB in the radiated noise along affected directivity angles.

While most multi-stream jets are operated with so-called normal velocity profiles (NVP)—where the inner jet streams have higher axial velocities than the outer streams—inverted velocity profile (IVP) jets redistribute the fan and core streams such that the inner flow velocity is less than the concentric outer flow. Far-field acoustic studies [9–13] on NVP and IVP jets have shown that IVP jets produce less noise than NVP jets for a range of conditions when both jets have the same effective mass flow rates, thrust, and exit areas. Since the exit areas are matched for these jets, the core stream in an NVP jet must have a higher velocity and the IVP jet a lower velocity than their fully-mixed equivalent jet. This results in a comparatively shorter potential core length for the IVP jet, leading to increased turbulent mixing and entrainment in the shear layer, all of which have been associated with net reduction in aft-radiated jet noise.

Modification of the velocity profile can also be obtained by intentionally introducing total temperature variations in a circular nozzle, as is the focus of the current work. In past work by the authors [14], it has been shown that the addition of a thermal non-uniformity, when compared to a thrust-, mass flow-, and exit area-matched uniform profile

jet, alters the shear layer turbulence and reduces the potential core length without modifying the pressure profile of the jet. All of the previously mentioned techniques tailor the flow to cause favorable changes in turbulent mixing near the nozzle exit in order to reduce the size of noise-producing coherent structures and the length of the potential core—observations that have been accompanied in past work by noise reduction in aft-radiated directions [7,15].

To maximize the effectiveness of applying temperature non-uniformities for jet noise reduction, the links between the vortical flow physics and the radiated noise must be better understood. Previous researchers have made hypotheses regarding the reductions in turbulent mixing noise in supersonic jets based on convection velocity estimates calculated from microphone data [16,17], temporally-resolved velocity measurements [18,19], computational simulations [20,21], and wave-packet modeling of coherent structures in the near-field of jet flows [22–24]. The research presented herein aims to shed light on the mean flow and turbulence structure of a jet with non-uniform total temperature by comparison to a baseline case with uniformly distributed total temperature. It will be shown that the slower velocity from a colder temperature stream introduced into a heated jet flow changes the mean velocity field and leads to asymmetries in the turbulence characteristics of the jet similar to those observed in other offset multi-stream jet studies [15,25].

This paper is organized as follows: Section II describes the experimental facility and methods used to acquire the flow field results, which are analyzed and placed into context with other works in Section III. Conclusions from the work are summarized in Section IV, along with needs and opportunities for further study.

II. Experimental Methods

A. Virginia Tech Heated Jet Rig, Instrumentation and Experimental Conditions

The Virginia Tech Heated Jet Rig, shown schematically in Figure 1, at the Advanced Power and Propulsion Laboratory (APPL) was used to conduct the experiments presented in this study. A round contour nozzle, designed using the axisymmetric method of characteristics ($D = 38.1\ mm$) by Kuo et al. [26] from Penn State University, was scaled and manufactured for the rig. The nozzle provides a uniform Mach 1.5 exit profile at perfectly expanded conditions. A converging secondary jet nozzle ($d = 8.38\ mm$) internal to the plenum was designed, manufactured, and added to this rig to introduce a total temperature non-uniformity within the heated primary jet flow (see Figure 2).

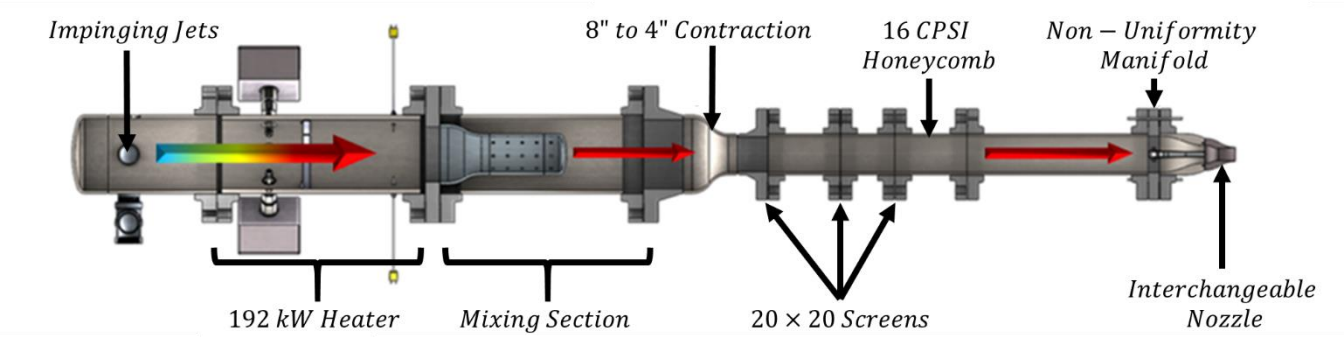

Fig. 1 Diagram of Virginia Tech Hot Jet Rig

The nozzle of the secondary jet stream was terminated at the inlet of the primary nozzle, upstream of the converging portion of the converging-diverging nozzle, as shown in Figure 2. Total pressure profiles taken across the exhaust plane of the jet revealed that the secondary jet had no discernable effect on the jet exit pressure profile for the thermally offset jet relative to the uniform jet, resulting in top-hat pressure and Mach number profiles with cross-sectional variation in total temperature. Further details regarding the design of this secondary jet stream can be found in the paper by Daniel et al. [27]

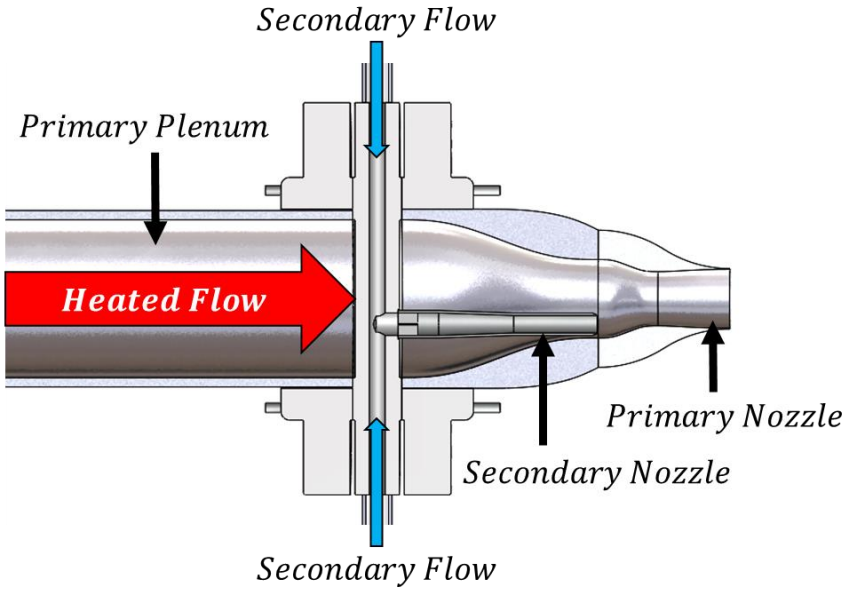

Fig. 2. Diagram of the coaxial jet geometry

The flow characteristics of the primary heated jet were determined from total pressure and temperature measurements taken in the primary jet plenum. Nozzle exit conditions, U_j, M_j and T_j, were determined by applying isentropic relations assuming ideal expansion to atmospheric pressure. Total pressure and temperature measurements from the secondary ambient flow plenum were used in conjunction with a Lambda-Square orifice meter to measure

and evaluate the mass flow rate of the secondary stream. Exit total temperature measurements were obtained using a vented thermocouple probe at a plane 0.04D (1.6 mm) downstream of the nozzle exit for both jet configurations. The probe was traversed in a square grid in 0.044D increments covering a square region of $1.1D \times 1.1D$. The data were recorded for 5 seconds at each point in order to ensure the probe reached thermal equilibrium.

A National Instruments (NI) 9213 thermocouple module in a NI cDAQ-9184 chassis was used to record total temperature data, while total pressures of both core and secondary streams were measured using a Scanivalve Corp. ZOC17IP/8Px-APC pressure scanner, digitized and recorded using the rig data acquisition system. This rig has been used in prior studies, the capabilities of which can be found in other references [14,27].

Table 1. Flow conditions for the uniform and thermally offset jets

Both cases			***Uniform***			
NPR_J	M_j	Re_j	TTR_j	$\dot{m}_j$	U_j	F_j
3.67	1.5	0.82×10^6	1.9	$0.587\frac{kg}{s}$	$578\frac{m}{s}$	$335\ N$

Thermally Offset								
$\frac{U_s}{U_p}$	$\frac{\rho_s}{\rho_p}$	TTR_p	TTR_s	NPR_s	$\dot{m}_p$	$\dot{m}_s$	U_p	F_{p+s}
0.72	1.9	2.0	1.0	4.77	$0.512\frac{kg}{s}$	$0.089\frac{kg}{s}$	$584\frac{m}{s}$	$342\ N$

The aero-thermodynamic conditions for the experiments, as calculated using isentropic compressible flow relations based upon the temperature and pressure measurements in the plenums, are presented in Table 1. The experiments were conducted for two cases: (1) a heated supersonic jet operating at a total temperature ratio (TTR) of 1.9 with a top hat temperature profile, and (2) a supersonic jet with TTR = 2.0 primary flow with a radially offset secondary jet introduced into the plenum at TTR = 1.1 The reported Reynolds number is for the uniform jet and is calculated using the primary jet exit conditions (U_j, μ_j, ρ_j). The Reynolds number for the primary plume of the thermally offset jet is very close to that of the uniform jet such that the Reynolds number most representative for dynamic scaling is nearly equal for both jets studied. For plots in section III, the mean velocities and Reynolds stresses are normalized using U_j for the uniform jet and U_p for the non-uniform, thermally offset jet. The aforementioned two conditions will be referenced as the uniform and thermally offset jet, respectively, throughout the remainder of the paper.

The difference between the TTR of the heated primary flow for the uniform and the offset jets was selected in an attempt to match, as closely as possible, the thrusts and mass flow rates of the two jets when calculated using isentropic relations. This accommodation resulted in matched mass flow rates for the two jet flows, while the thermally offset

jet produced a combined thrust (F_{p+s}) that was about 2.0% higher than the uniform jet (F_j). Thrust was computed by integration of the exit flow aero-thermodynamic conditions assuming ideal expansion.

B. Particle Image Velocimetry

Stereoscopic Particle Image Velocimetry (PIV) was the primary tool used to measure the vector mean velocity field and turbulent Reynolds stress distributions along the jet centerline. Two 5.5 megapixel LaVision Imager sCMOS cameras mounted with 50 mm focal length Nikon lenses and 532 nm band-pass light filters were used to image the laser-illuminated particles in the flow field. A Quantel EverGreen 200 mJ/pulse frequency-doubled Nd:YAG laser emitting 532 nm wavelength light was used and operated with a pulse delay of $\Delta t = 1\,\mu s$, chosen to balance uncertainties from inter-frame correlation and relative pixel-displacement errors.

PIV velocity planes were acquired on the center-plane of the jet in an axial-transverse plane, as depicted in Figure 3. Three planes were acquired each with 5.5 D axial spacing by traversing the laser/camera arrangement using a Velmex Bi-slide linear translation stage. Care was taken to acquire overlapping planes of data for cross-plane stitching in post-processing.

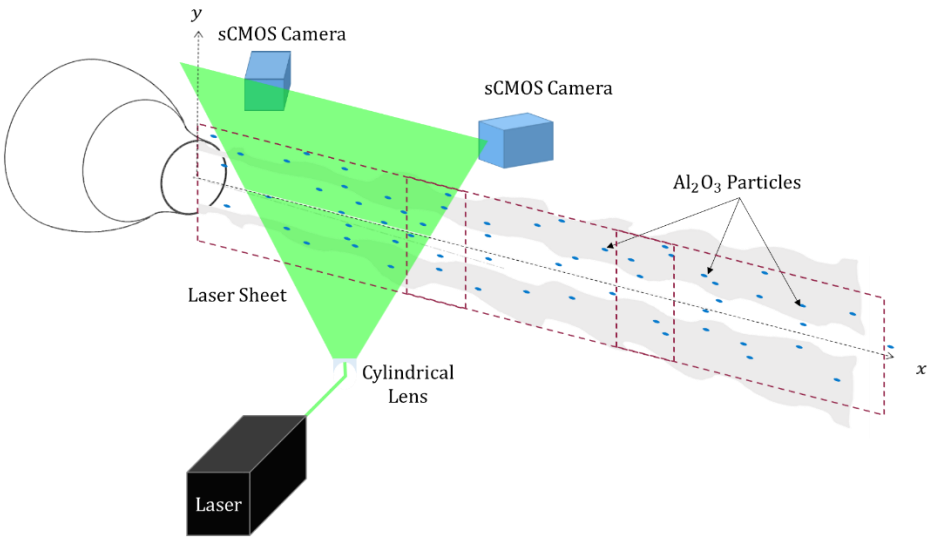

Fig. 3. Diagram of the PIV laser setup with the coordinate system labeled.

The characteristics of the particle seeding used for PIV are summarized in Table 2. The primary and secondary jet flows were seeded using 350 nm nominal size alumina (Al_2O_3) particles, and the entrainment region around the plume was seeded using a MDG MAX 3000 fog generator producing 500 -700 nm diameter mineral oil particles. The relaxation time for the aluminum oxide seeding yields a Stokes number based upon the integral scales of the jet of 0.03, such that large-scale fluctuations are well-captured, along with the majority of the turbulent fluctuation energy.

Table 2. Seeding Characteristics

Parameters	Al_2O_3	$Mineral\ Oil$
Density $\rho_{part.}$	3950 kg/m^3	800 kg/m^3
Diameter $D_{part.}$	300 nm (nominal)	500-700 nm
Relaxation time t_0	2.1 μs	0.8 μs
Seeding Port	Primary and secondary plenums	External entrainment

The PIV images were recorded and post-processed using LaVision DaVis 8.4 software. Two thousand image pairs were recorded at 15 Hz using the three overlapping axial camera positions. This arrangement captured the full developmental regions of both jet conditions studied. Stereo PIV self-calibration [28] was applied to improve the accuracy of the PIV velocities. In order to maximize the confidence in the velocity vector calculations, a total of five progressively refined image correlation passes was executed. Square 128 x 128-pixel interrogation windows with 50% overlap were used for the first two correlation passes, while the final three passes used 32 x 32-pixel adaptive correlation window-shape with 75% overlap between adjacent windows. The final pass resulted in a measurement resolution for the entire flow field image of 320 x 240 vectors; while each velocity vector had a nominal spatial resolution of 0.47 mm x 0.47 mm, or approximately 0.01D x 0.01D.

The integrity of each velocity vector sample was assured using image- and statistics-based validation. A threshold of two was set for the peak-ratio validation parameter—the ratio of the primary PIV correlation peak to the second-largest peak. This validation parameter provides a measure of the ambiguity present in the identification of the correlation peak. In addition, a two-pass median filter was used to find and replace spurious vectors with differences from nearest neighbors of greater than four standard deviations.

C. PIV Uncertainties

It was determined that the dominant velocity uncertainties are due to position uncertainties in the multi-plane stitching of the PIV data acquired by axial traversing. Although extensive care was taken during data acquisition, non-repeatability in the rig thermal expansion resulted in small misalignments between the traverse and the jet flow. A laser sheet thickness of approximately 4 mm, wider than used in many applications, was employed in order to reduce uncertainty of the data due to flow misalignment. Additional position uncertainties manifest themselves in the axial positions, especially with regards to the overlap region of these laser planes.

In order to quantify the uncertainty in the overlap between these positions, a perturbation analysis was performed on the data from each PIV traverse position. The raw planar velocity data were initially aligned using the experimentally determined axial positions and overlapping measurements compared. Next, the mean velocity magnitude image for each downstream camera position was cross-correlated with its immediate upstream neighbor, and the shift in distance found was taken as the x/D and y/D uncertainty of the downstream camera positions. The resulting PIV position uncertainties are presented in Table 3. While larger than the resolution of individual velocity vectors, these uncertainties are consistent with the precision of the instrument positioning hardware used in the experiment.

Table 3. Positional uncertainty in camera location

	x/D	y/D
Position 1 to Position 2	± 0.061	± 0.037
Position 2 to Position 3	± 0.074	± 0.037

Statistical standard error uncertainties with a 95% confidence interval were computed for the mean velocities and Reynolds stresses presented in this paper, and reported in Table 4, using the methods presented by Bendat & Piersol [29]. Since statistical uncertainties vary with the local statistical moments, only the maximum uncertainties encountered within the entire measurement domain, i.e., the worst cases, are reported.

Table 4. Standard Error Uncertainties with 95% Confidence Interval

$Property$	$Maximum$
$\overline{U_x}/U_j$	$\pm 7.0 \times 10^{-3}$
$\overline{u_x'u_x'}/U_j^2$	$\pm 1.5 \times 10^{-3}$
$\overline{u_y'u_y'}/U_j^2$	$\pm 0.65 \times 10^{-3}$
$\overline{u_x'u_y'}/U_j^2$	$\pm 0.44 \times 10^{-3}$

III. Results and Discussion

Unsteady flow field velocity measurements are presented to explain key facets of the mean velocity field and turbulence structure in a thermally non-uniform round jet, particularly in comparison to a uniform baseline jet at matched mass flow and exit Mach number conditions. Several observations are made that indicate common features shared among the thermally offset flow field and other flow fields reported in literature for eccentric multi-stream jets. The systematic presentation of the results to follow, starting with exit conditions and mean axial velocity contours and progressing to detailed Reynolds stress distributions, is intended to provide clear insights into the impacts that temperature non-uniformity have on the evolution of the turbulence field.

All velocity and turbulence data are non-dimensionalized on the isentropic exit velocity, U_j for the uniform jet, and U_p for the thermally offset jet. As both jet flows are plotted on the same graph for ease of comparison, U_j will be used as the scripting language on the plots for simplicity. The axial and transverse positions are always normalized on the primary nozzle exit diameter, D. The transverse regions of the thermally offset case will often be referred to using "thick side" and "thin side" terminology. The thick side refers to the side of the thermally offset jet containing the cooler temperature plume, while the thin side is radially opposite the thick side. For the cross-section plots to follow, the thin side of the offset jet is the spatial region where $y/D > 0$ and the thick side is the spatial region where $y/D < 0$, with $y/D = 0$ being the geometric centerline of the thermally offset jet.

A. Jet Exit Temperature Profiles

The flow conditions at the nozzle exit provide critical details for assessing behavior of the plume further downstream. TTR contours are provided in Figure 4 for the uniform (Figure 4(a)) and thermally offset (Figure 4(b)) plumes. The core of the uniform jet was assessed for temperature variation, and found to have 2.4% root-mean-square variation in TTR. The cooler temperature jet flow introduced into the thermally offset jet, as observed in Figure 4(b) produces a local minimum TTR =1.3, despite the initial temperature of this plume being measured as TTR = 1.1. The increase in TTR of the cold plume at the nozzle exit has been attributed to heating of the secondary nozzle by the surrounding primary flow within the plenum.

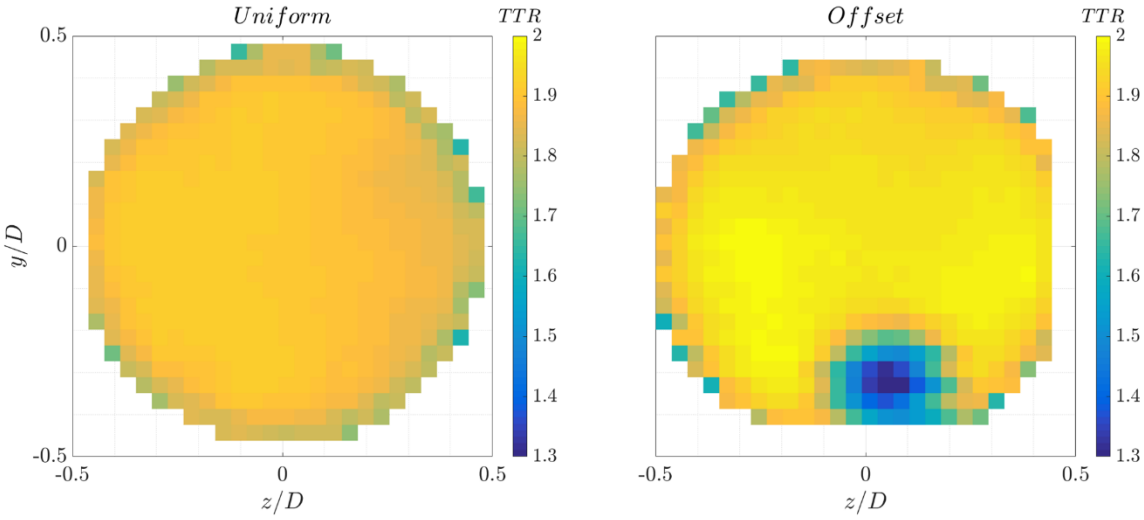

(a) **(b)**

Fig. 4. TTR contours for (a) the uniform jet and (b) the thermally offset jet.

B. Mean Velocity Field

Given the pressure-matched conditions between the primary and secondary flows, and the substantial differences in temperature, it is clear that the mean velocity distributions will be altered considerably by the introduced thermal non-uniformity. Contours and radial profiles of mean axial velocity are provided in Figures 5 and 6, respectively.

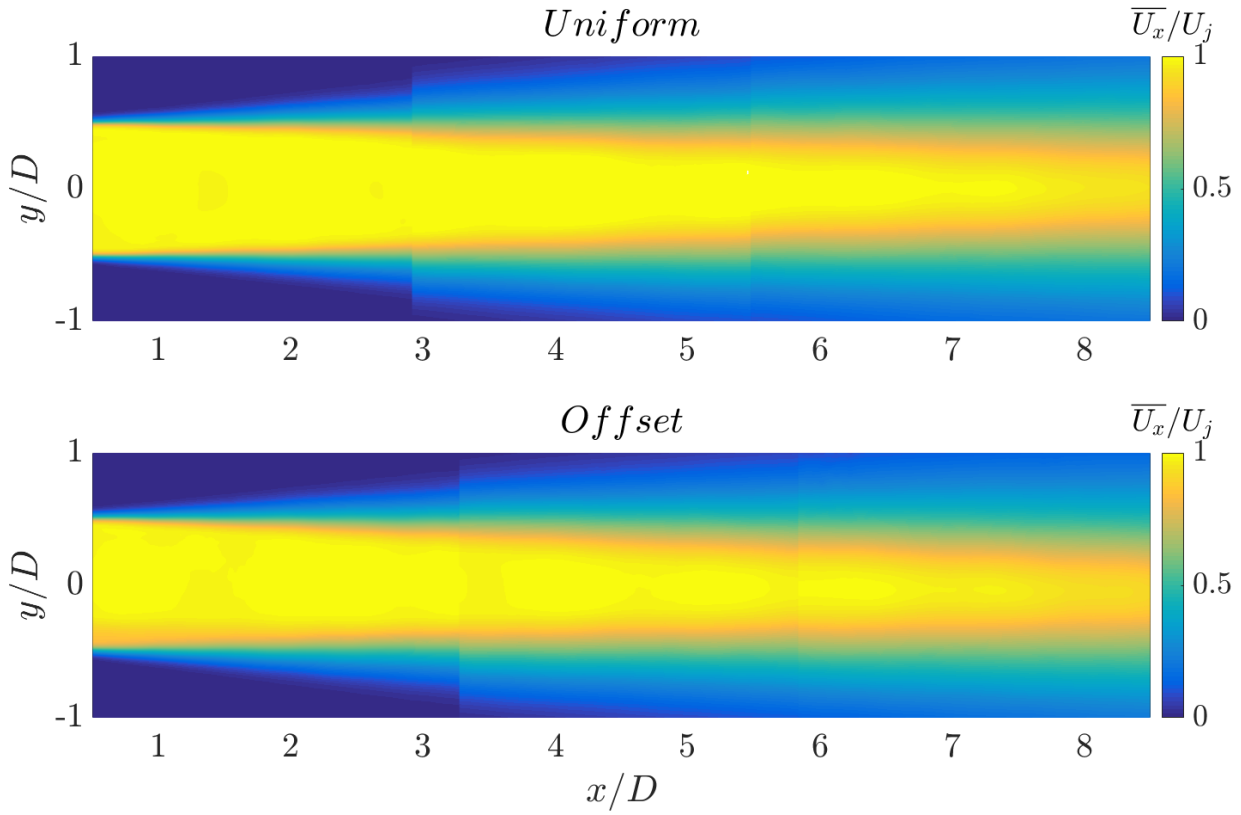

Fig. 5. Axial mean velocity contours for the uniform and thermally offset jet.

At first glance, the contours of Figure 5 appear to show little difference between the two jet flows; however, a number of subtle, yet significant, differences are present. Near the nozzle, the thermally offset plume exhibits a reduction in the mean velocity, effectively thickening the shear layer, on the lower half of the plume in the vicinity of the colder flow. At $x/D = 1$, particularly evident in the profile for that station shown in Figure 6, the velocity profile on the thin side of the thermally offset jet follows that of the uniform jet, whereas on the thick side, there is a 17% reduction in the velocity near the nozzle, owing to the lower sound speed in the region influenced by the $TTR = 1.3$ secondary flow stream. As the axial velocity profile evolves with downstream distance, deviations from the uniform jet profile on the thin side of the thermally offset jet begin to manifest, while the thick side profile assumes nearly the

same shear profile as the uniform jet for $x/D > 5$. Another notable difference in the contours is the decay of the centerline velocity is greater for $x/D > 7$ for the thermally offset jet, indicating that the length of the potential core has been reduced. The mechanisms driving the changes observed on the thin side of the jet are hypothesized to be due to asymmetric instabilities in the shear layer of the jet produced by the ambient temperature plume. It is particularly interesting to note that these same mean velocity behaviors are present in offset multi-stream jets such as those presented in refs. [14,29]. Further common characteristics to eccentric jets are visible in the plume turbulence structure and are discussed in the following subsections.

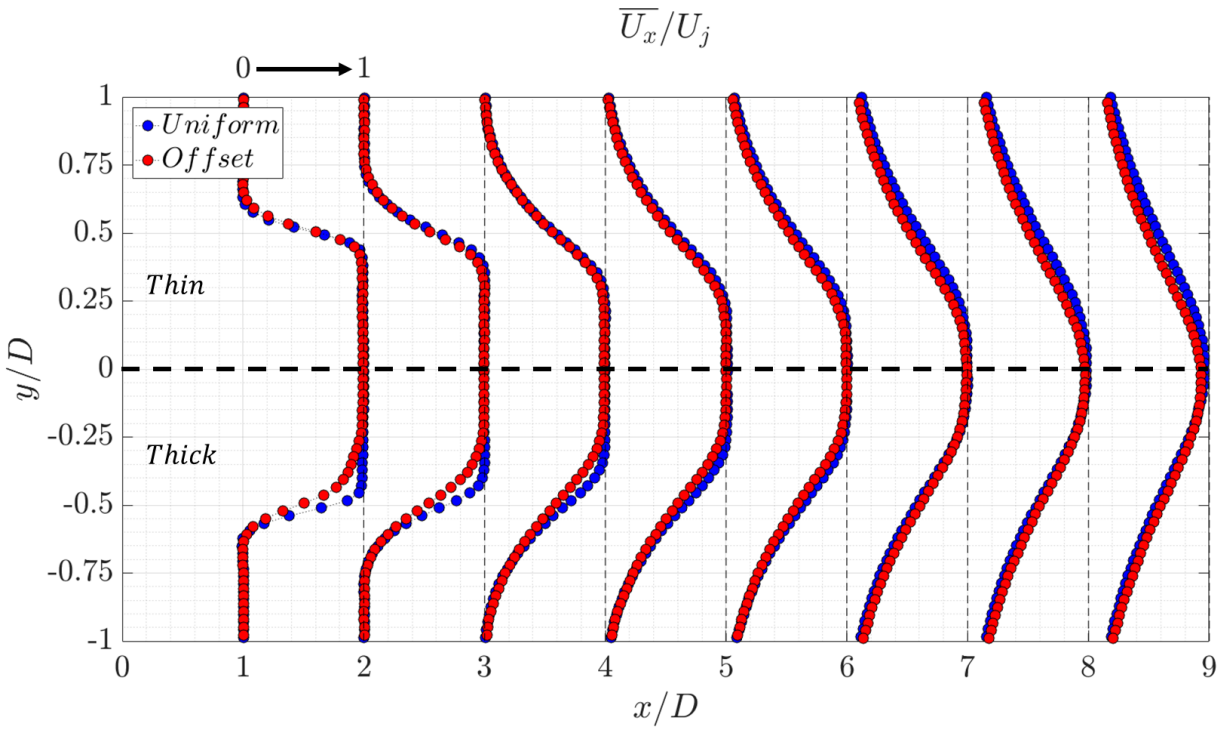

Fig. 6. $\overline{U_x}$ velocity radial profiles for the uniform (blue) and thermally offset (red) jets.

C. Turbulence Structure

The instantaneous PIV images enable one to obtain Reynolds stresses throughout the measurement domain for analysis of the detailed turbulence structure. The uncertainties reported in Table 4 indicate that the number of images acquired yield statistically converged results to the precision needed for meaningful conclusions when comparing the uniform and non-uniform datasets.

Radial profiles of the in-plane Reynolds normal stresses ($\overline{u_x'u_x'}$ and $\overline{u_y'u_y'}$) and the Reynolds shear stress ($\overline{u_x'u_y'}$) are provided in Figures 7-9 over the axial region $1 \leq x/D \leq 8$. The asymmetry caused by the non-uniform

temperature is apparent in each of the stresses. The first major observation of note is the location of the peak turbulence on both sides of the thermally offset jet. On the thick side ($y/D < 0$), the peak $\overline{u_x'u_x'}$ remains approximately at the nozzle lip line ($y/D = -0.5$) at all measured axial locations. In contrast, the peak $\overline{u_x'u_x'}$ locations move toward the jet centerline with increasing axial distance on the thin side ($y/D > 0$), while increases in the Reynolds stress values up to 25% at a given radius are seen at some downstream locations. The asymmetry of the flow field has resulted in a more rapid growth of the vortical layer toward the centerline on the thin side, apparent in each of the Reynolds stress components plotted. For instance, the zero-crossing for the Reynolds shear stress (see Figure 9) migrates below the centerline for the $x/D = 7$ and 8 stations.

The reduction in the peak axial Reynolds normal stress is greatest on the thick side for $3 \leq x/D \leq 6$ and is related to the reduced local shear present at those stations in the region $-0.5 \leq y/D \leq -0.2$. This is an intriguing behavior, likely indicating that the placement and extent of the cooler secondary flow region can be used to selectively reduce turbulence in an axial region of interest. In terms of the jet noise reduction application motivating this study, there is a close relationship between the frequency of radiated noise and the axial location in the jet where it is emitted due to the axial growth of turbulent length scales. Intentionally focusing turbulence intensity reductions at chosen axial positions can hypothetically create spectrally-targeted noise reductions in the peak emission directions.

Turbulence is enhanced for $x/D \leq 2$ due to rapid mixing that occurs near the nozzle between the primary hot stream and the cooler secondary stream (see Figures 10 and 11). The internal shear from the thermally offset non-uniformity has introduced turbulence in the region $-0.5 \leq y/D \leq -0.25$ and large relative differences in the transverse Reynolds normal stress near the nozzle (see $x/D \leq 2$ stations in Figures 7-11). The transverse normal stress ($\overline{u_y'u_y'}$) profile diffuses inward toward the centerline from the thin side, generating a significantly asymmetrical profile for $x/D \geq 6$. On the thick side, there is also an observable increase in the transverse stress magnitudes for the thermally offset jet, but this only occurs from the lower jet lipline towards ambient. The transverse motions indicated by $\overline{u_y'u_y'}$, particularly near the ambient edge of the jet, point toward asymmetric entrainment rates on the thick and thin sides of the jet.

Although not plotted explicitly, the Reynolds shear stress exhibits regions of reduced correlation coefficients with the normal stresses, $\overline{u_x'u_y'}/\sqrt{\overline{u_x'u_x'}\,\overline{u_y'u_y'}}$. The shear stress values are similar in magnitude between the uniform and offset cases, while $\overline{u_x'u_x'}$ and $\overline{u_y'u_y'}$ are increased on the thin side at stations $x/D \geq 6$ for the offset case. As such, the

turbulent motions contributing to $\overline{u_x'u_y'}$ are slightly less active in regions of the offset case—i.e., less energy in these motions contribute to shear stresses that interact more significantly with the mean flow in the Reynolds-averaged momentum equation. Given that the non-axisymmetric mean flow itself will reduce the azimuthal coherence of motions from the thermally offset nozzle, the reduced coherence appears to result in more inactive motions with greater three-dimensionality than present in the uniform case.

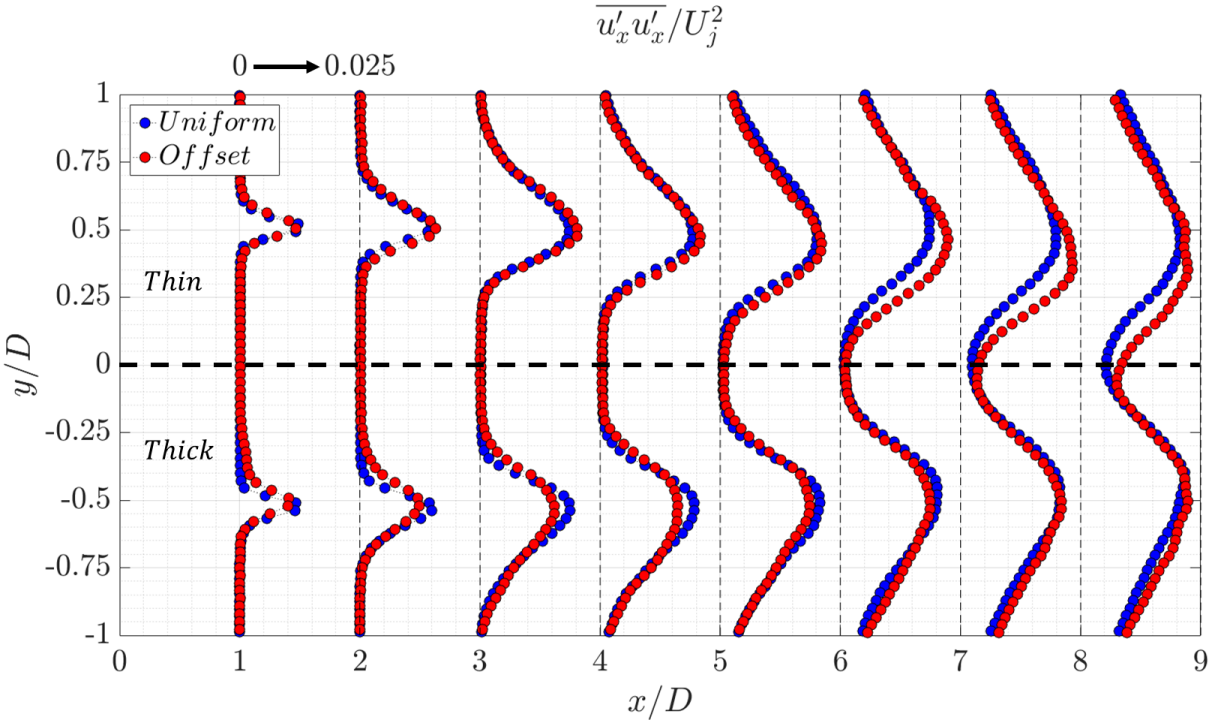

Fig. 7. $\overline{u_x'u_x'}$ axial Reynolds normal stress profiles for the uniform and thermally offset jets.

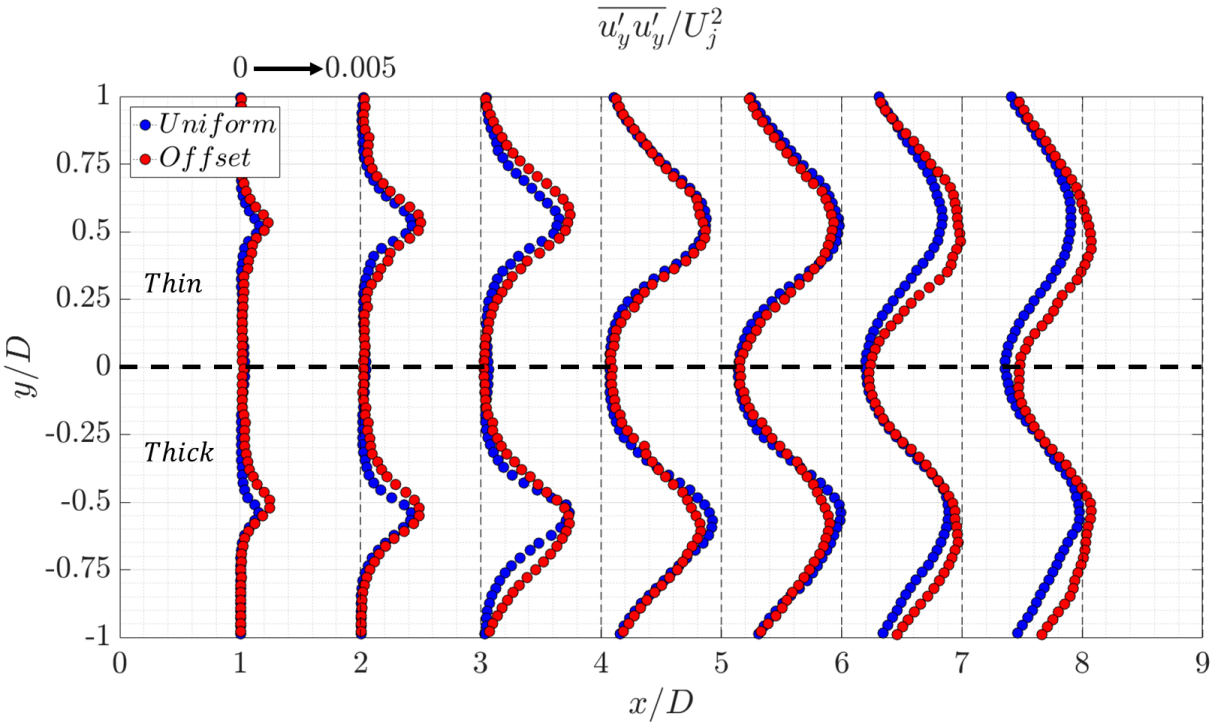

Fig. 8. $\overline{u'_y u'_y}$ transverse Reynolds normal stress cross-sections for the uniform and thermally offset jets.

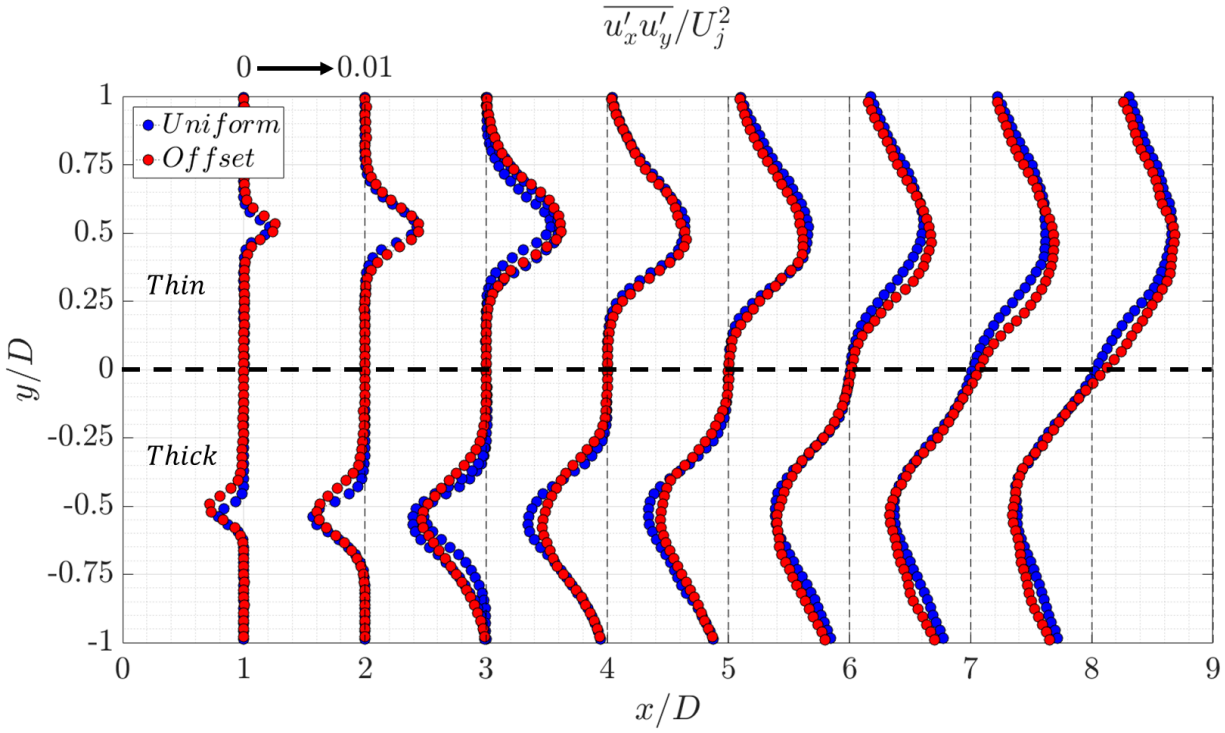

Fig. 9. $\overline{u'_x u'_y}$ Reynolds shear stress profiles for the uniform and thermally offset jets.

Examining the axial development of turbulence more closely near the nozzle exit (Figures 10 and 11), the changes to the mean axial and shear stress from the presence of the ambient temperature offset plume are more apparent. The

cooler temperature region has the practical effect of broadening the shear layer on the thick side and promoting turbulent diffusion of lower momentum flow toward the centerline. For $x/D = 0.5$ there is a secondary inflection point at $y/D \approx -0.4$ where the shear stress closely approaches zero and increases slightly toward the centerline, stemming from the low mean velocity gradient near the center of the cooler temperature plume that causes locally-reduced mixing. Close observation of Figure 10 reveals a flat feature in $\overline{u_x'u_x'}$ at the same station arising for the same reason. As is apparent from the turbulence profiles further downstream (referring back to Figures 7-9), the complexity of the flow field quickly increases as the uniform primary and secondary streams mix and the shear layer thickness is no longer much smaller than the jet diameter.

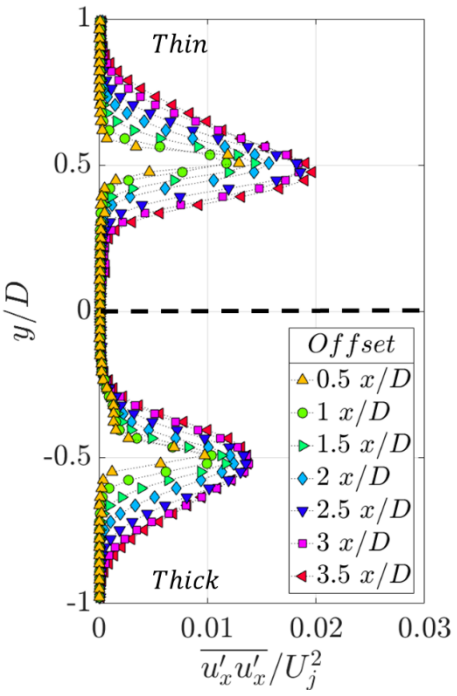

Fig. 10. Near nozzle $\overline{u_x'u_x'}$ velocity profiles for the thermally offset jet.

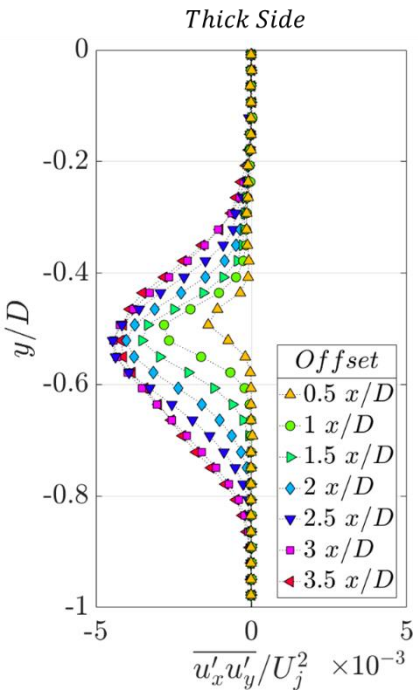

Fig. 11. Near nozzle $\overline{u_x'u_y'}$ Reynolds shear stress profiles for the thermally offset jet.

D. Similarities to and insight for multi-stream offset jets

The observations made above are very similar in nature to those reported by Henderson et al. [8], Henderson & Wernet [25] and Papamoschou [15] for multi-stream offset jets shown to offer major reductions in far-field large-eddy mixing noise. From the current study, the presence of the thermal non-uniformity serves to alter flow characteristics throughout the developmental regime of the jet. The cooler temperature plume causes an asymmetric shift in the mean

velocities and Reynolds stresses in the jet. As with multi-stream offset jets, the thin side of the plume exhibits a regions with greater turbulence, while the thick side has a significant axial extent with reduced Reynolds normal stress values.

The data support that the presence of the temperature non-uniformity affects the turbulence development by augmenting the entrainment rate of the jet shear layer, particularly given notable increases in the transverse Reynolds stresses (Figure 8). The changes occur not only on the side where non-uniformity has been introduced, but also the opposite side. The same asymmetric features are observed in multi-stream offset jets, clearly being driven by three-dimensional effects related to the shape of the jet profile. Physical interpretations or simplified modeling/scaling concepts informed solely by local flow features in this flow, for example reasoning the features and physical interpretation of the thin side of the jet based on usual local shear layer parameters such as thickness, velocity ratio and density ratio, fail due to the importance of three-dimensional interactions throughout the jet. Given the changes affected by the non-uniformity in the mean velocity field, the instability field will be non-axisymmetric; and the base flow will promote the growth of structures with varying scales and fluctuation energies around the azimuth of the plume—quite different from the dominant instabilities of the equivalent uniform round jet.

The motivation for the current work has been to use flow non-uniformity to alter turbulence development, ultimately with the goal of reducing radiated jet noise. Although the current results show relatively subtle changes in the flow structure, they have been achieved with similarly modest differences in temperature between the primary and secondary streams. Scaling the concept for greater differences between the heated primary stream and the cooler offset stream would create larger effects. For instance the large-eddy simulations of over-expanded jets with thermal non-uniformities conducted by Tamm et al. [30] for a primary stream at $TTR = 7$ and the secondary at $TTR = 3$ showed significant changes in the flow field which caused significant reductions in radiated noise. The results from this recent computational study suggest that increasing the TTR difference between the two jet streams can potentially lead to significant reductions radiated noise in high speed jets.

IV. Conclusion

An experimental study has been conducted to compare the flow fields of heated Mach 1.5 jets with and without total temperature non-uniformity. PIV measurements were collected on both jet flows to a distance of ten jet diameters from the nozzle exit, and the mean axial velocity and turbulence profiles were analyzed to explore and identify the changes in the flow field arising from temperature non-uniformity.

The presence of the temperature non-uniformity alters flow characteristics throughout the developmental regime of the jet. There are non-axisymmetric changes in the mean velocity development of the non-uniform plume that persist throughout the region examined. Peak turbulence levels show shifts in position and magnitude when non-uniformity is present. The peak axial Reynolds normal stresses are reduced for stations in the range $3 \leq x/D \leq 6$, related to the reduced local shear present at those stations in the transverse region $-0.5 \leq y/D \leq -0.2$ due to the presence of the temperature non-uniformity. The peak normal stresses on the side opposite the thermal non-uniformity are consistently greater than for the uniform jet, and the axial Reynolds normal stress peak locations shift toward the centerline as the vortical layer growth appears augmented in that region of the plume.

These observations are all consistent with features previously observed by other researchers studying multi-stream eccentric co-annular plumes. A potential impact of the current work is as a step toward generalizing the offset stream approach to a broad class of tailored non-uniform nozzle exit flow distributions. For instance, the non-uniform flow field examined herein could be used to target a specific range and directivity pattern for the noise spectrum by affecting the turbulence in the $3 \leq x/D \leq 6$ region of the plume. One could imagine the possibility of more sophisticated tailoring that could affect different regions or varying azimuths of the plume for targeted changes. In future work, it is hoped that the role of linear instabilities on the development of the plume turbulence can be used to guide choices for tailored exit profiles to achieve desired outcomes.

Acknowledgments

This work was sponsored by the U.S. Office of Naval Research, program manager Dr. Steven Martens, via grants N00014-16-1-2444 and N00014-14-1-2836.

References

[1] NARC, 2009, *Report on Jet Engine Noise Reduction*.

[2] Alkislar, M. B., Krothapalli, A., and Butler, G. W., 2007, "The Effect of Streamwise Vortices on the Aeroacoustics of a Mach 0.9 Jet," J. Fluid Mech., **578**, p. 139.

[3] Arakeri, V. H., Krothapalli, A., Siddavaram, V., Alkislar, M. B., and Lourenco, L. M., "On the Use of Microjets to Suppress Turbulence in a Mach 0.9 Axisymmetric Jet," *Journal of Fluid Mechanics*, Vol. 490, Oct. 2003, pp. 75–98. doi: 10.1017/s0022112003005202

[4] Krothapalli, A., Greska, B., and Arakeri, V., "High-Speed Jet Noise Reduction Using Microjets," *Combustion Processes in Propulsion*, 2006, pp. 231–244. doi: 10.1016/b978-012369394-5/50026-3

[5] Powers, R. W., Kuo, C.W., and Mclaughlin, D. K., "Experimental Comparison of Supersonic Jets Exhausting from Military Style Nozzles with Interior Corrugations and Fluidic Inserts," *19th AIAA/CEAS Aeroacoustics Conference*, May 2013. doi: 10.2514/6.2013-2186

[6] Stuber, M., Ng, W. F., and Lowe, K. T., "Synthesis of Convection Velocity and Turbulence Measurements in Three-Stream Jets for Investigation of Noise Sources," *23rd AIAA/CEAS Aeroacoustics Conference*, June 2017. doi: 10.2514/6.2017-4045

[7] Papamoschou, D., and Phong, V. C., "The Very Near Pressure Field of Single- and Multi-Stream Jets," *55th AIAA Aerospace Sciences Meeting*, January 2017. doi: 10.2514/6.2017-0230

[8] Henderson, B. S., and Leib, S. J., "Measurements and Predictions of the Noise from Three-Stream Jets," *21st AIAA/CEAS Aeroacoustics Conference*, May 2015. doi: 10.2514/6.2015-3120

[9] Tanna, H. K., Tester, B. J., Lau, J.C., "The Noise and Flow Characteristics of Inverted-Profile Coannular Jets," NASA-CR-158995, February 1979

[10] Tanna, H. K., "Coannular Jets—Are They Really Quiet and Why?," *Journal of Sound and Vibration*, Vol. 72, No 1, September 1980, pp. 97–118. doi: 10.1016/0022-460X(80)90710-5

[11] Tanna, H. K., and Morris, P. J., "The Noise from Normal-Velocity-Profile Coannular Jets," Journal of Sound and Vibration, Vol. 98, No. 2, January 1985, pp. 213–234. doi: 10.1016/0022-460X(85)90386-4

[12] Maus, J. R., Goethert, B. H., and Sundaram, C. V., "Noise Characteristics of Coannular Flows with Conventional and Inverted Velocity Profiles," *Journal of Aircraft*, Vol. 18, No. 2, February 1981, pp. 135–141. doi: 10.2514/3.57474

[13] Dahl, M. D., *The Aeroacoustics of Supersonic Coaxial Jets*, NASA-TM-106782, November 1994.

[14] Mayo Jr, D. E., Daniel, K., Lowe, K. T., and Ng, W. F., "Experimental Investigation of a Heated Supersonic Jet with Total Temperature Non-Uniformity," *23rd AIAA/CEAS Aeroacoustics Conference*, June 2017. doi: 10.2514/6.2017-3521

[15] Papamoschou, D., "Modelling of Noise Reduction in Complex Multistream Jets," *Journal of Fluid Mechanics*, Vol. 834, November 2017, pp. 555–599. doi: 10.1017/jfm.2017.730

[16] Tinney, C. E., and Jordan, P., "The Near Pressure Field of Co-Axial Subsonic Jets," *Journal of Fluid Mechanics*, Vol. 611, September 2008, pp. 175–204. doi: 10.1017/S0022112008001833

[17] Glauser, M. N., Leib, S. J., and George, W. K., "Coherent Structures in the Axisymmetric Turbulent Jet

Mixing Layer," *Fifth International Symposium on Turbulent Shear Flows*, August 1985. doi: 10.1007/978-3-642-71435-1_13

[18] Kerhervé, F., Jordan, P., Gervais, Y., Valière, J. C., and Braud, P., "Two-Point Laser Doppler Velocimetry Measurements in a Mach 1.2 Cold Supersonic Jet for Statistical Aeroacoustic Source Model," *Experiments in Fluids*, Vol. 37, No. 3, September 2004, pp. 419–437. doi: 10.1007/s00348-004-0815-1

[19] Lau, J. C., "Laser Velocimeter Correlation Measurements in Subsonic and Supersonic Jets," *Journal of Sound and Vibration*, Vol. 70, No. 1, May 1980, pp. 85–101. doi: 10.1016/0022-460X(80)90556-8

[20] Towne, A., Colonius, T., Jordan, P., Cavalieri, A. V., and Brès, G. A., "Stochastic and Nonlinear Forcing of Wavepackets in a Mach 0.9 Jet," *21st AIAA/CEAS Aeroacoustics Conference*, May 2015. doi: 10.2514/6.2015-2217

[21] Towne, A., Brès, G. A., and Lele, S. K., "A Statistical Jet-Noise Model Based on the Resolvent Framework," *23rd AIAA/CEAS Aeroacoustics Conference*, June 2017. doi: 10.2514/6.2017-3706

[22] Cavalieri, A. V. G., Rodríguez, D., Jordan, P., Colonius, T., and Gervais, Y., "Wavepackets in the Velocity Field of Turbulent Jets," *Journal of Fluid Mechanics*, Vol. 730, September 2013, pp. 559–592. doi: 10.1017/jfm.2013.346

[23] Papamoschou, D., "Wavepacket Modeling of the Jet Noise Source," *17th AIAA/CEAS Aeroacoustics Conference*, June 2011. doi: 10.2514/6.2011-2835

[24] Sinha, A., Rodríguez, D., Brès, G. A., and Colonius, T., "Wavepacket Models for Supersonic Jet Noise," *Journal of Fluid Mechanics*, Vol. 742, March 2014, pp. 71–95. doi: 10.1017/jfm.2013.660

[25] Henderson, B. S., and Wernet, M., "Characterization of Three-Stream Jet Flow Fields," *54th AIAA Aerospace Sciences Meeting*, January 2016, doi: 10.2514/6.2016-1636

[26] Kuo, C.W., Mclaughlin, D. K., Morris, P. J., and Viswanathan, K., "Effects of Jet Temperature on Broadband Shock-Associated Noise," *AIAA Journal*, Vol.53, No. 6, June 2015, pp. 1–16. doi: 10.2514/1.J053442

[27] Daniel, K.A., Mayo, Jr., D. E., Lowe, K.T., and Ng, W.F., "Experimental Investigation of the Very Near Pressure Field of a Heated Supersonic Jet with a Total Temperature Non-Uniformity," *2018 AIAA/CEAS Aeroacoustics Conference*., June 2018, doi: 10.2514/6.2018-3145

[28] Wieneke, B., "Volume Self-Calibration for 3D Particle Image Velocimetry," Experiments in Fluids, Vol.45, No. 4, June 2008 pp. 549–556. doi: 10.1007/s00348-008-0521-5

[29] Bendat, J.S., Allan, G. P., *Random Data: Analysis and Measurement Procedures,* 4th ed., Wiley, New York, February 2010. doi: 10.1002/9781118032428

[30] Tamm, P., Bres, G. A., Towne, A., and Lele, S. K., "Leveraging Large-Eddy Simulations to Investigate the Influence of Temperature Non-Uniformity on Jet Noise," *Center for Turbulence Research Proceedings of the Summer Program 2018,* December 2018.

Statistical Flow Structures in Heated Supersonic Jets with Offset Temperature Non-Uniformities

David E. Mayo Jr.[1], Kyle A. Daniel[2], K. Todd Lowe[3], and Wing F. Ng[4]
Advanced Propulsion and Power Laboratory, Virginia Tech, Blacksburg, VA, 24061, USA

Recent research has revealed that introducing total temperature non-uniformities into heated supersonic jets can alter the turbulence characteristics, resulting in far-field noise reductions. In this study, the large-scale turbulent structures in the shear layers of two round, perfectly-expanded Mach 1.5 heated jet flows are compared and analyzed: a uniformly heated jet and heated jet with an offset cold temperature plume. Quadrant analysis, a conditional averaging technique which identifies statistical flow structures contributing to local mean shear stress, was applied to PIV measurements at a probe point located at $x/D = 2$ and the radial location of peak $\overline{u_x' u_y'}$ stress in each jet. The resultant structures confirmed that the dominant mechanisms for shear stress generation were reverse entrainment ($u_x' < 0, u_y' > 0$) and forward ejection ($u_x' > 0, u_y' < 0$) motions that had a negative magnitude and cumulatively made up 80% of the observed events. The forward entrainment ($u_x' > 0, u_y' > 0$) and reverse ejection ($u_x' < 0, u_y' < 0$) motions were associated with pinching events, characterized by a strong positive shear stress structure centered on the probe point and lobes of weaker negative shear stress bracketing the probe point. The evidence indicates an increase in the three-dimensionality of the turbulence due to the introduction of the cold plume.

I. Nomenclature

$\boldsymbol{C}$ = Two-Point Cross-Correlation Coefficient Matrix

D = Primary Jet Exit Diameter (m)

d = Secondary Jet Exit Diameter (m)

[1] Graduate Research Assistant, Department of Mechanical Engineering, AIAA Student Member
[2] Graduate Research Assistant, Crofton Department of Aerospace and Ocean Engineering, AIAA Student Member
[3] Associate Professor, Crofton Department of Aerospace and Ocean Engineering, AIAA Associate Fellow
[4] Alumni Distinguished Professor, Department of Mechanical Engineering, AIAA Fellow

f = Frequency $(1/sec)$

F = Isentropic Jet Thrust (N)

I = Quadrant Analysis Piecewise Filter Function

L = Integral Length Scale (m)

M = Mach Number

$\dot{m}$ = Mass Flow Rate (kg/m^3)

Q = Quadrant $(Q1, Q2, Q3, Q4)$

QF = Quadrant Fraction

$\boldsymbol{r}$ = Location Vector for Integral Length Scale

R = Ideal Gas Constant for Air $\left(\frac{J}{kgK}\right)$

$\mathcal{R}$ = Integration Range for the Integral Length Scale

Re = Jet Reynolds Number $(\rho U_j D/\mu)$

St = Strouhal Number (fD/U_j)

T = Temperature (K)

t_0 = Relaxation Time (sec)

U = Velocity (m/s)

u' = Fluctuating Velocity (m/s)

x = Axial Coordinate Axis (m)

y = Transverse Coordinate Axis (m)

$\delta_{\bar{\Omega}_\theta}$ = Vorticity Thickness (m)

Δt = PIV Inter-Frame Time Delay (sec)

μ = Dynamic Viscosity $(kg/m \cdot s)$

Ω = Vorticity $(1/sec)$

ρ = Density (kg/m^3)

γ = Heat Capacity Ratio

Subscripts

a,b = Matrix Indices

c = Convection

j = Uniform Jet Heated Plume Condition at Nozzle Exit

m, α, β = Quadrant Number (1,2,3,4)

n = Sample Number

p = Thermally Offset Jet Primary Stream Condition at Nozzle Exit

s = Thermally Offset Jet Secondary Stream Condition at Nozzle Exit

x = Axial Component

y = Transverse Component

θ = Azimuthal Component

Superscripts

$\bar{}$ = Mean Variable

$'$ = Fluctuating or Mean-Subtracted Variable

$\tilde{}$ = Conditionally-Averaged Mean Variable

II. Introduction

Recent developments have suggested that total temperature non-uniformity in supersonic jets can cause favorable turbulence modifications and noise reduction [1,2]. For instance, the introduction of a lower temperature plume into an otherwise heated supersonic free jet flow produces far-field noise reductions which scale with the total temperature ratio (TTR) difference between them. The current work seeks to shed light on the subtle changes in statistical turbulent flow structures that are associated with non-uniform heated supersonic jets.

Modifying the exit conditions of jet flows has been shown in many prior studies to alter the radiated noise characteristics through modulation of the turbulent scales and development in the jet shear layer [3-13]. Fluid injections and inserts [2-5], multi-stream axisymmetric and asymmetric jets [6-8], inverted velocity profile jets (IVP) [9-13], and thermally non-uniform jets are among the methods currently used to modulate the flow field of jet exhausts.

Recent experimental and computational studies of multi-stream axisymmetric and asymmetric jets have shown favorable reductions in radiated far field noise [5–7]. It has been found that the potential core length in the primary jet of asymmetric multi-stream jets is shorter, which enhances turbulent mixing in the shear layer region opposite the secondary jet plume. As a result, convection velocities are reduced and stream-wise vortices form, altering the global

mean flow field and being associated with far field noise reductions in the range of 2 to 6 dB along affected directivity angles.

Introducing total temperature variations into the nozzle of a jet can be used to intentionally vary the velocity and turbulence profiles. Recent work by the authors [2,14] has revealed that adding a cooler region to an otherwise heated jet flow alters turbulence development in the shear layer and reduces the length of the potential core when compared to a thrust-, mass flow-, and exit area-matched heated jet flow. Tamm et al.[15] performed LES on a jet flow exhausted from a military style nozzle at realistic operating conditions containing a temperature non-uniformity and found a 1.6 dB reduction in peak overall sound pressure level (OASPL), with up to 5 dB reductions in peak spectral narrowband sound pressure levels.

In the current work, we seek to use statistical analysis on flow data gathered using particle image velocimetry (PIV) to better understand the subtle difference in the turbulent structures caused by cross-sectional temperature variation. Given the role that Reynolds shear stress plays in determining the Reynolds-averaged mean flow, in addition to the links it has to jet noise radiation [16] we have chosen to use a conditional averaging approach that isolates events producing and counteracting peak Reynolds shear stress—quadrant analysis. Quadrant analysis was originally developed to identify turbulent structures that contribute to shear stress production in boundary layers [17] and has since been applied to a wide variety of turbulent flows as noted in the review by Wallace [18]. The technique has occasionally been applied to free shear flows such as wakes [19] and mixing layers [20], and rarely, to free jets [21–23]. Örlü & Alfredsson [21] used quadrant analysis to study the shear layer of a swirling free jet and identify the mechanisms that facilitated enhanced turbulence evolution compared to non-swirling jets. Sreenivasan & Antonia [23] used quadrant analysis to analyze the joint probability distributions of the fluctuating velocities and temperatures in a subsonic jet to a model Gaussian distribution. Most recently, Viggiano et al. [22] applied quadrant analysis to PIV data acquired on vertical, low Reynolds number, variable density jets that simulate geophysical flows. To the authors' knowledge, this is the first study presenting quadrant analysis to velocity data collected on supersonic heated jets.

The goal of the current study is to identify changes in conditionally-averaged turbulent structures present in a thermally non-uniform round supersonic jet which may contribute to a reduction in radiated noise. In an acoustic study by Daniel et al. on the thermally offset jet flow, a 1.5 dB reduction was observed in the peak jet noise direction. The reduction observed is small, but statistically significant and acoustic benefit is expected to scale with the TTR difference between the primary and secondary plumes [15]. In this paper, it will be shown that introducing a small,

cold region of flow near the edge of the plume causes a net increase in entrainment of ambient fluid into the shear layer compared to the uniform baseline. The increased entrainment in the thermally offset jet is associated with radially larger turbulent structures and lower conditionally-averaged Reynolds stress amplitudes in conditionally-averaged structures in the outer shear compared to the uniform jet. The quadrant analysis revealed the presence of counter-rotating vortical structures and an increase in the three dimensionality of the turbulence for the offset jet, which are likely to have an impact on noise-producing events.

This paper is organized as follows: Section III describes the experimental facility and methods used to acquire the flow field results. Section IV describes the mathematics of the quadrant analysis technique in the context of experimental jet flow data, and Section V presents the results and analysis of the two jet flows. Section VI summarizes the conclusions from the study.

III. Experimental Methods

A. Virginia Tech Heated Jet Rig, Instrumentation and Experimental Conditions

The Virginia Tech Heated Jet Rig (Fig. 1), located at the Advanced Power and Propulsion Laboratory was used to obtain the data presented in this study. A round 1.5 design Mach number primary nozzle, (D = 38.1 mm), developed by Kuo et al. using the axisymmetric method of characteristics, was rescaled and constructed for this rig. A secondary, offset converging nozzle (d = 8.38 mm), terminating at the inlet of the primary nozzle, was installed to produce a reduced total temperature plume in the heated jet flow (Fig. 2). Details regarding the construction of the secondary jet stream can be found in Daniel et al [14]. and analysis of the exit total temperature profiles of both the uniform and the thermally offset jets can be found in Mayo et al [2].

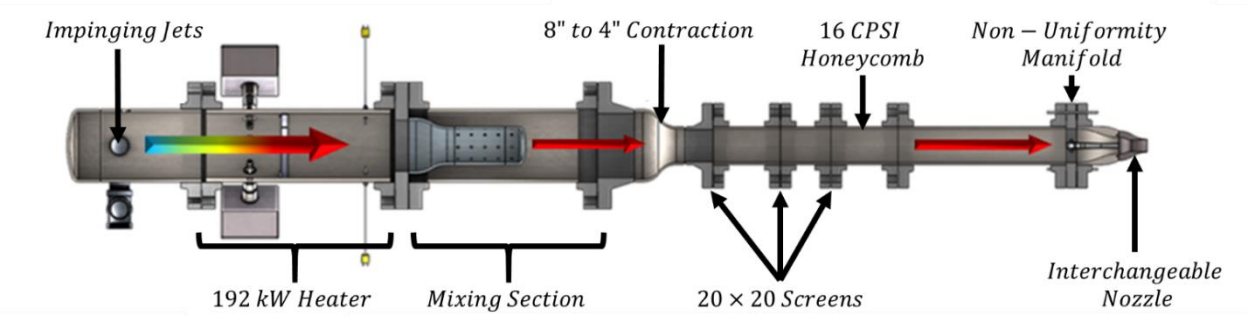

Fig. 1 Diagram of Virginia Tech Hot Jet Rig

All pressure values were measured using a Scanivalve Corp. ZOC17IP/8Px-APC pressure scanner and all temperature values measured with K-type thermocouples/probes and recorded with a NI 9213 module in a NI cDAQ-

9184 chassis. The experiments were conducted for two cases: (1) a heated supersonic jet operating at a total temperature ratio (TTR) of 1.9 with a uniform temperature profile, and (2) a supersonic jet with TTR = 2.0 primary flow with a radially offset secondary jet introduced into the plenum at TTR = 1.1 The aero-thermodynamic flow conditions for the primary and secondary jet streams were calculated with isentropic compressible flow relations and the aforementioned measured pressure and temperature values, are presented in Table 1. The reported Reynolds number is for the uniform jet and is calculated using the primary jet exit conditions (U_j, μ_j, ρ_j). The Reynolds number for the primary plume of the thermally offset jet is close enough to the uniform jet that the Reynolds number most representative for dynamic scaling is nearly equal.

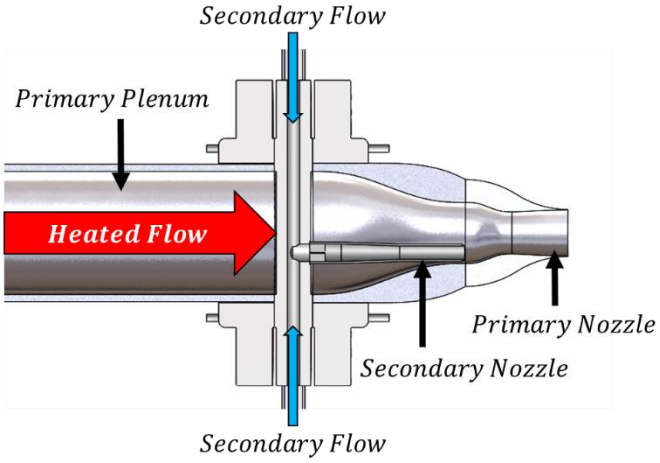

Fig. 2. Diagram of the coaxial jet geometry

Table 1. Flow conditions for the uniform and thermally offset jets

Both Cases			**Uniform**			
NPR_J	M_j	Re_j	TTR_j	$\dot{m}_j$	U_j	F_j
3.67	1.5	0.82×10^6	1.9	$0.587\frac{kg}{s}$	$578\frac{m}{s}$	$335\ N$
Thermally Offset						
$\frac{U_s}{U_p}$	$\frac{\rho_s}{\rho_p}$	TTR_p	TTR_s	NPR_s	$\dot{m}_p$	$\dot{m}_s$	U_p	F_{p+s}
0.72	1.9	2.0	1.1	4.77	$0.512\frac{kg}{s}$	$0.089\frac{kg}{s}$	$584\frac{m}{s}$	$342\ N$

B. Particle Image Velocimetry

Stereo Particle Image Velocimetry (PIV) measurements were collected on both the uniform and thermally offset jet flows. Two 5.5 megapixel LaVision Imager sCMOS cameras mounted with 50 mm focal length Nikon lenses and 532 nm band-pass light filters were used to image the laser-illuminated particles in the flow field. A Quantel EverGreen 200 mJ/pulse frequency-doubled Nd:YAG laser emitting 532 nm wavelength light was used and operated with a pulse delay of $\Delta t = 1\ \mu s$, chosen to balance uncertainties from inter-frame correlation and relative pixel-displacement errors.

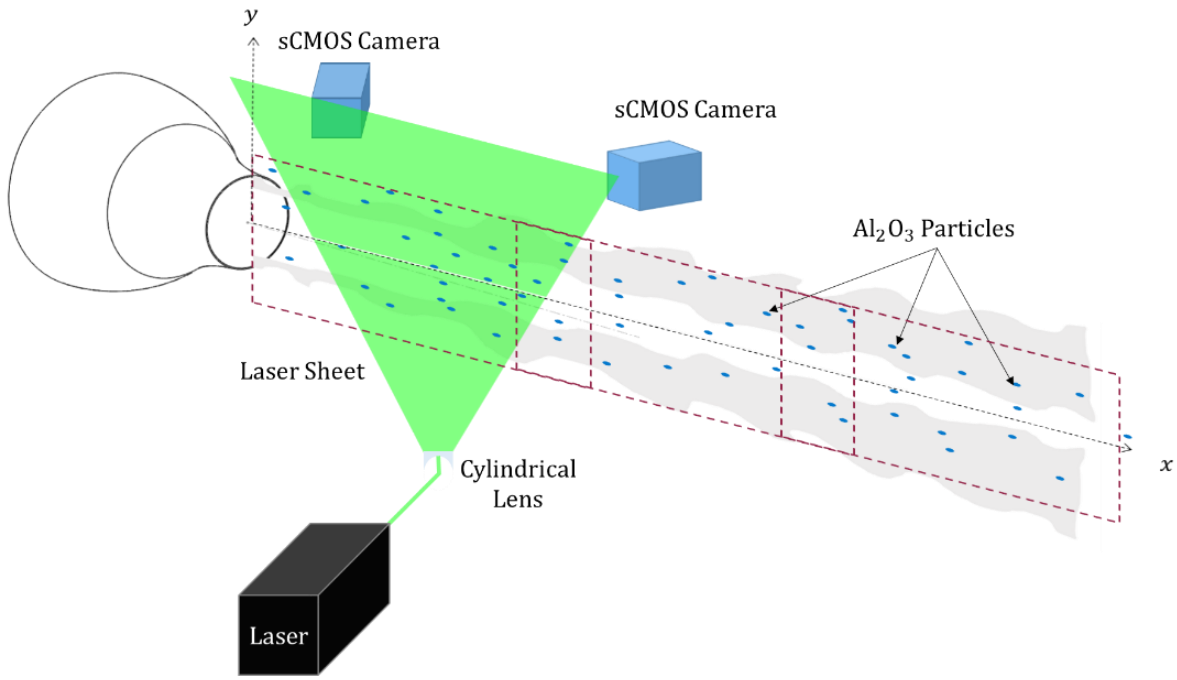

Fig. 3. Diagram of the PIV laser setup with the coordinate system labeled.

PIV velocity planes were acquired on the center-plane of the jet in an axial-transverse plane, as depicted in Fig. 3. Three planes were acquired each with 5.5 D axial spacing by traversing the laser/camera arrangement using a Velmex Bi-slide linear translation stage. Care was taken to acquire overlapping planes of data for cross-plane stitching in post-processing. Details regarding the seeding characteristics and data processing technique can be found in Mayo et al. [2]. Statistical standard error uncertainties with a 95% confidence interval were computed for the mean velocities and Reynolds stresses presented in this paper, and reported in Table 4, using the methods presented by Bendat & Piersol [24]. Since statistical uncertainties vary with the local statistical moments, only the maximum uncertainties encountered within the entire measurement domain, i.e., the worst cases, are reported.

Table 2. Standard Error Uncertainties with 95% Confidence Interval

$Property$	$Maximum$
$\overline{U_x}/U_j$	$\pm 7.0 \times 10^{-3}$
$\overline{u_x' u_x'}/U_j^2$	$\pm 1.5 \times 10^{-3}$
$\overline{u_y' u_y'}/U_j^2$	$\pm 0.65 \times 10^{-3}$
$\overline{u_x' u_y'}/U_j^2$	$\pm 0.44 \times 10^{-3}$

IV.Data Analysis Techniques

A. Spatial Two-Point Correlation and Integral Length Scales

One method for evaluating the local spatial structure of turbulence in spatially resolved data is performing two-point correlations and find the associated integral length scales. The integral length scale is a metric representing the average of the turbulent scales in the flow, lower bounded by the spatial resolution of the measurements and upper bounded by the size of the measurement domain. The full domain is used to evaluate the integral length scales for this study as both correlations and anti-correlations are expected to contribute to the turbulence structure in the domain space due to the use of the cross-correlation coefficient.

The spatial two-point cross-correlation coefficient for the shear stress, $\boldsymbol{C}(\boldsymbol{x}_a, \boldsymbol{y}_b)$is defined as,

$$\boldsymbol{C}(\boldsymbol{x}_a, \boldsymbol{y}_b) = \frac{cov[\boldsymbol{U_x}(x,y), \boldsymbol{U_y}(\boldsymbol{x}_a, \boldsymbol{y}_b)]}{var[\boldsymbol{U_y}(x,y)] \cdot var[\boldsymbol{U_y}(\boldsymbol{x}_a, \boldsymbol{y}_b)]}, \tag{1}$$

where x, y defines the fixed probe point and $\boldsymbol{x}_a, \boldsymbol{y}_b$ is point (a, b) in the position matrix of the measured flow field. From the resulting cross-correlation coefficient field, the integral length scales of the shear stress can be evaluated as

$$L_r/D = \int_{r=0}^{\mathcal{R}} \boldsymbol{C}(\boldsymbol{r})\,/D\,, \tag{2}$$

where $\boldsymbol{r}$ is the range of $\boldsymbol{x}$ at the probe y location or the range of $\boldsymbol{y}$ at a probe x location, and $\mathcal{R}$ is the extent of the measurement domain in the axial and transverse directions respectively.

B. Quadrant Analysis

Quadrant analysis is a conditional averaging technique which classifies and filters events in a turbulent flow into four quadrants based on the sign of the fluctuating velocity at a singular point of interest. The quadrant analysis conditional average is defined as,

$$\widetilde{u_x'u_y'}(\boldsymbol{x},\boldsymbol{y})_m = \frac{1}{N}\sum_{n=1}^{N} u_x'(\boldsymbol{x},\boldsymbol{y},\boldsymbol{t}_n)u_y'(\boldsymbol{x},\boldsymbol{y},\boldsymbol{t}_n)I_m[\,u_x'(x,y,\boldsymbol{t}_n),u_y'(x,y,\boldsymbol{t}_n)], \tag{3}$$

where m is the quadrant (1,2,3,4), **x**, and **y**, are the position vectors, x and y are the probe point location, t is the sample vector, n is the sample number, N is the total number of samples, and I_m is the piecewise function,

$$I_m\big[u_x'(x,y,\boldsymbol{t}_n),u_y'(x,y,\boldsymbol{t}_n)\big] = \begin{cases} 1, if\ \left(u_x',u_y'\right) \text{ is in quadrant } m \\ 0, \text{ otherwise.} \end{cases} \tag{4}$$

The method for performing this decomposition is as follows. One, select a point of interest in the flow field, which will be referred to as a probe point throughout this paper. Two, filter the entire flow field into four bins of data based on the sign of the fluctuating velocities at the probe point. The four bins are called quadrants and each quadrant is associated with a dominant motion at the probe point. Once the turbulence data has been decomposed, then the average shear stress in each bin is computed to resolve the statistical shear stress structure associated with the motion at the probe point.

Quadrant analysis has historically been used in evaluating the shear stress structure of boundary layer flows. When applied to wall-bounded flows, the four quadrants are defined as follows (assuming a coordinate system with x in the streamwise direction and y positive normal to the wall): Q1 ($u_x' > 0, u_y' > 0$) outward interaction, Q2 ($u_x' > 0, u_y' < 0$) ejections, Q3 ($u_x' < 0, u_y' < 0$) inward interactions, Q4 ($u_x' > 0, u_y' < 0$) sweeps [17,18]. Summing the averages from all four quadrants will return the mean shear stress.

An important metric in quadrant analysis is the quadrant fraction, QF_m—the frequency of observing events in each quadrant—defined as,

$$QF_m = \frac{\sum_{n=1}^{N} I_m\big[u_x'(x,y)_n; u_y'(x,y)_n\big]}{\sum_{m=1}^{4}\sum_{n=1}^{N} I_m\big[u_x'(x,y)_n; u_y'(x,y)_n\big]}. \tag{5}$$

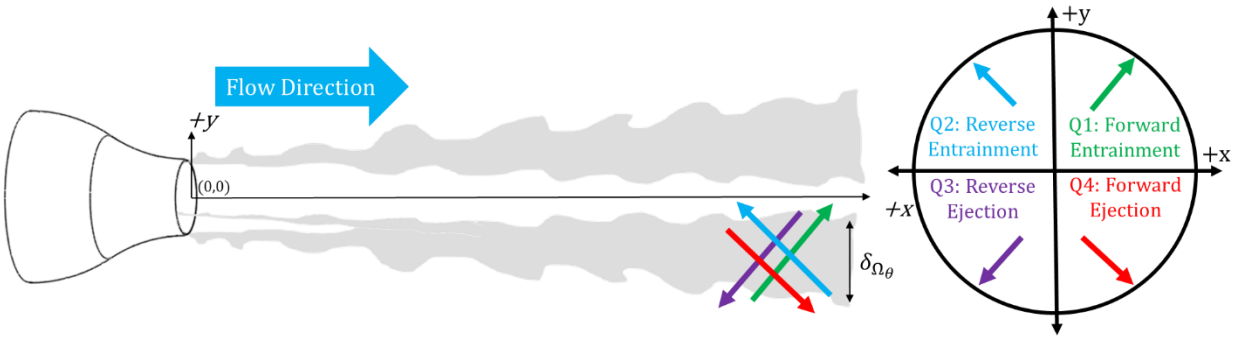

Fig. 4. Diagram of the four quadrants and their definitions as applied to half of the free jet.

In applying quadrant analysis to a free jet, the physical meanings of the four quadrants differ from that observed in wall-bounded flows. For this study, the four quadrants are interpreted as: Q1 ($u'_x > 0, u'_y > 0$) forward entrainment, Q2 ($u'_x > 0, u'_y < 0$) reverse ejection, Q3 ($u'_x < 0, u'_y < 0$) reverse ejection, Q4 ($u'_x > 0, u'_y < 0$) forward ejection, as labeled in Fig. 4. Entrainment motions transport turbulence from the ambient into the jet and ejection motions transport turbulence from the potential core towards the ambient. Forward and reverse motions describe whether the turbulence motions move downstream or upstream in the shear layer. The new interpretation of the events were introduced by Viggano et al. [22], and for this study, the definitions only apply to velocity data where $y/D < 0$. Note that Q2 and Q4 motions are dominant in producing the net shear stress for this coordinate system.

V. Results and Discussion

A. Jet Exit Temperature Profiles

The flow conditions at the nozzle exit provide critical details for assessing behavior of the plume further downstream. TTR contours are provided for the uniform, Fig. 5 (a), and thermally offset, Fig. 5 (b), plumes. The core of the uniform jet was assessed for temperature variation, and found to have 2.4% root-mean-square variation in TTR. The cooler temperature jet flow introduced into the thermally offset jet, as observed in Fig. 4 (b) produces a local minimum TTR =1.3, despite the initial temperature of this plume being measured as TTR = 1.1. The increase in TTR of the cold plume at the nozzle exit has been attributed to heating of the secondary nozzle by the surrounding primary flow within the plenum.

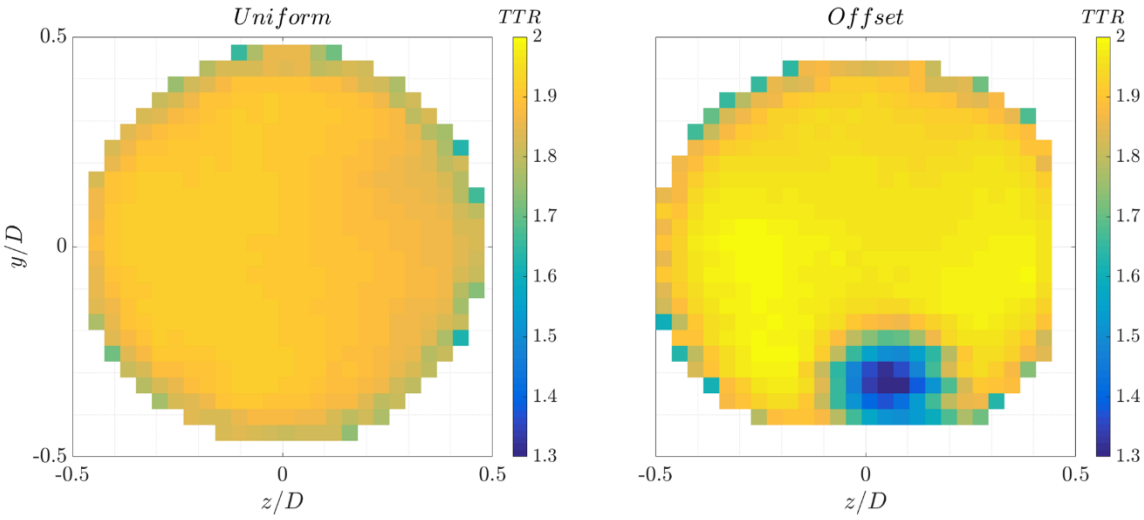

(a) **(b)**

Fig. 5. TTR contours for (a) the uniform jet and (b) the thermally offset jet.

B. Changes in the Mean Velocity and Shear Layer

An in-depth analysis of the mean velocity and Reynolds stress profiles for both the uniform and thermally offset jets were originally published by Mayo et al. [2] A brief summary of the results from that study will be provided here to establish a basis for the discussions in further subsections.

Figure 6 contains cross-section profiles of the mean axial velocity for the uniform and offset jets. At $x/D = 1$, the velocity profile on the thin side of the offset jet follows that of the baseline jet, whereas on the thick side, there is a maximum local velocity reduction of 17% compared to the uniform jet , due to the reduced speed of sound associated with the nearby colder secondary flow. Near the potential core collapse region ($x/D > 7$), the velocity profile on the thin side of the offset jet begins to deviate from the uniform jet profile.

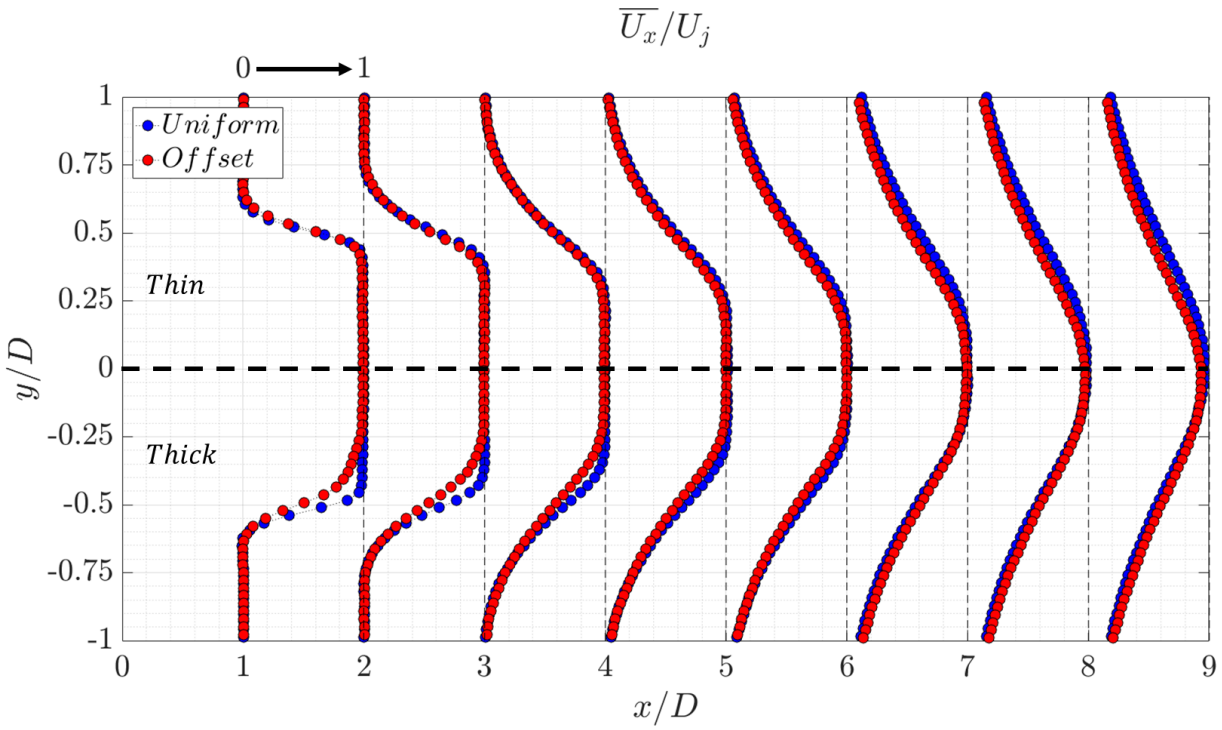

Fig. 6. $\bar{U}_x$ **velocity profiles for the uniform (blue) and thermally offset (red) jets.**

Cross-jet profiles of Reynolds shear stress, $\overline{u_x' u_y'}$, are plotted in Fig. 7. Near the nozzle ($x/D \leq 2$), one notices a transverse broadening of the shear layer for the thick side of the offset jet compared to the uniform baseline. This thickening of the shear layer can be attributed to the vorticity of the cold plume and the associated increase in turbulent mixing it facilitates. However, the thickening of the shear layer is not associated with a significant increase in the peak shear stress intensity. For $x/D \geq 5$, the subtle differences observed between the two jet flows become negligible. On the thin side near the potential core collapse region, the peak shear stress location of the offset jet moves closer to the jet centerline compared to the uniform jet. The shift in the peak causes deviations in the shear stress profiles between the two jet cases to manifest between $0 < y/D < 0.5$.

From the brief overview of the mean axial velocity and shear stress profiles, it has been established that there are small, but notable differences between the uniform and thermally offset jets. Understanding the changes in the structure of the large scale turbulence in the shear layer will provide insight into what physical metrics have changed which may lead to a reduction in far-field radiated noise.

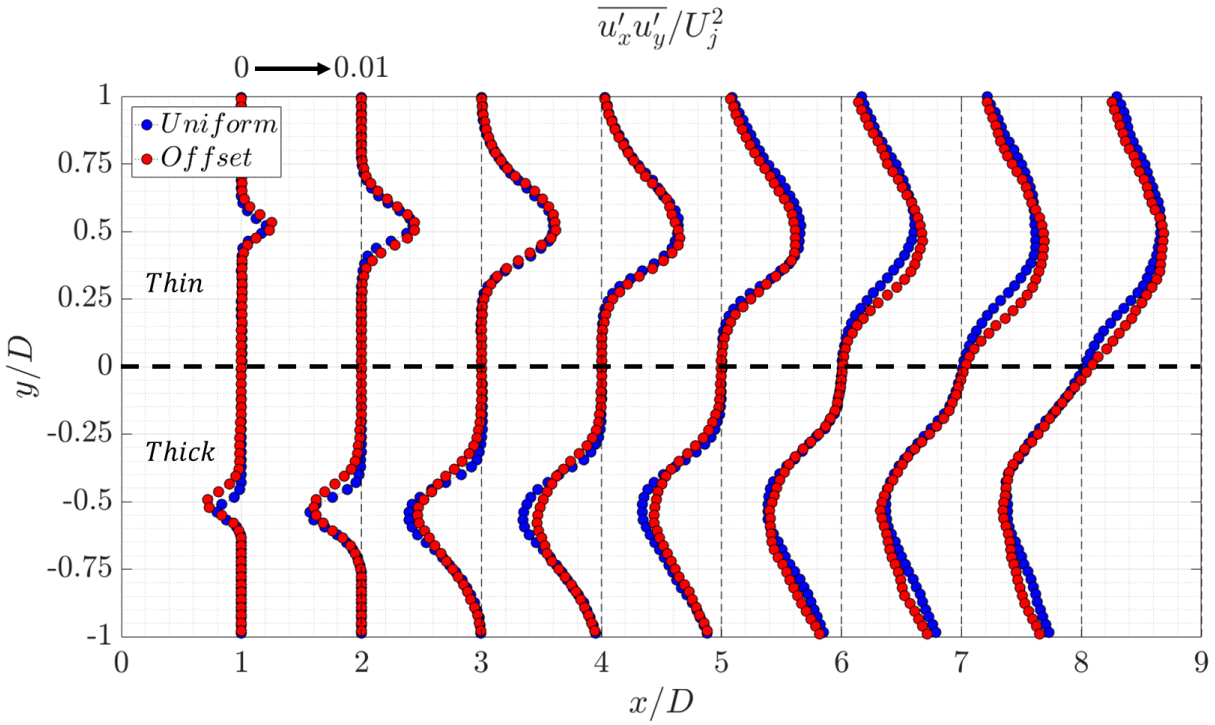

Fig. 7. $\overline{u'_x u'_y}$ Reynolds shear stress profiles for the uniform and thermally offset jets.

To quantify the differences observed in the mean axial velocity, Reynolds shear stress, and shear stress production profiles near the nozzle, the vorticity thickness was computed for $1 < x/D < 3$, which can be observed in Fig. 8. The vorticity thickness, $\delta_{\bar{\Omega}_\theta}$, for this study is defined as,

$$\frac{\delta_{\bar{\Omega}_\theta}(x)}{D} = \frac{U_j}{max(\partial \bar{U}_x/\partial y) \cdot D} \tag{5}$$

where $\bar{\Omega}_\theta$ is the mean azimuthal vorticity [25].

Immediately, one notices in Fig. 8 that the shear layer of the offset jet is much thicker than the uniform jet in the near nozzle region—as expected from the velocity statistics of Figs. 6 and 7. Additionally, the vorticity layer growth rate is slightly larger for the offset jet compared to the uniform case. The changes observed can be directly attributed to the presence of the cold plume in the offset jet. The plume serves to increase the size of the region containing turbulent mixing near the shear layer, causing the vortical layer in the offset jet to be thicker, while the reduced local velocities associated with the cold plume region also reduce the axial growth rate of the vortical layer. Analyses in sections V.F and V.G will provide a deeper view into how turbulent structures differ in the two cases, ultimately affecting the local entrainment and ejection frequencies and mechanisms.

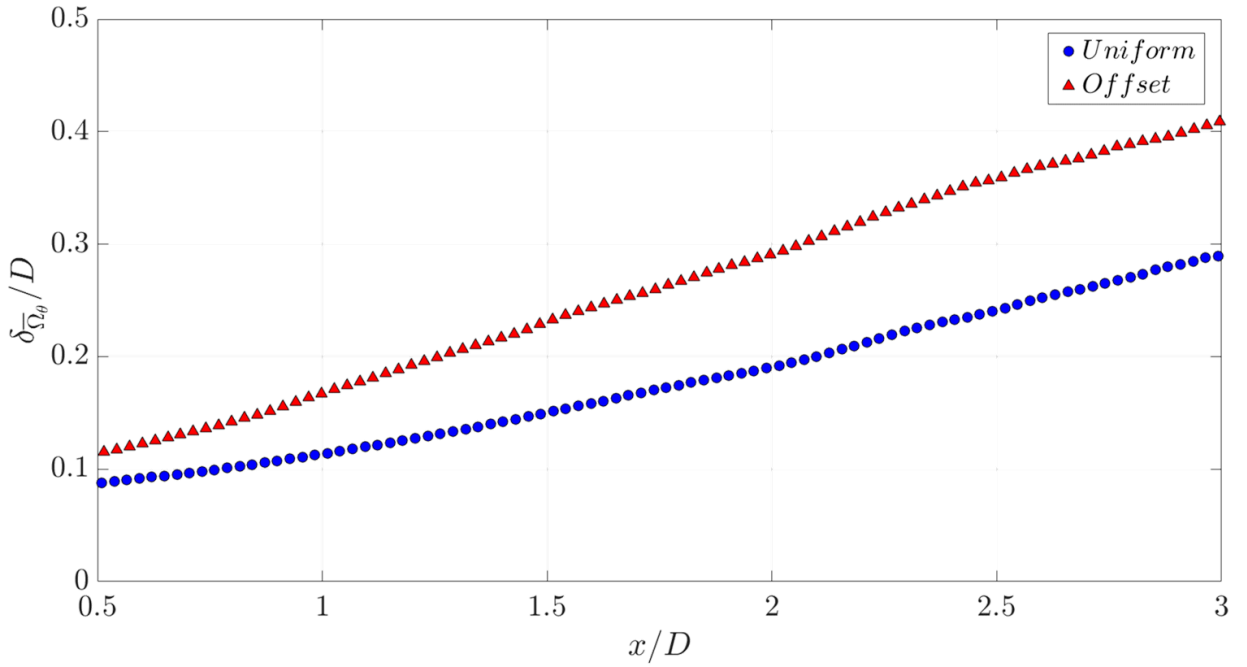

Fig. 8. Vorticity thickness of the shear layer in the uniform and offset jets with the vorticity layer growth rate labeled.

C. Mean Shear Stress Turbulence Structure in the Near Nozzle Region of the Jet

The maximum transverse shear stress location at $x/D = 2$ for both the uniform and offset jets was selected for analysis. The axial location was chosen because this is the furthest upstream location where the effects of the secondary plume still persist and the conditionally averaged structures could be fully resolved. The transverse location was selected because recent studies [6,16] have provided compelling evidence that the large scale structures centered on the outermost peak shear stress surface of the jet are the largest contributors to noise radiated to the far-field in peak directions. Based on these criteria, the probe point location of the peak shear stress were found to be $(x/D, y/D) = (2, -0.53)$ for both jets. To evaluate the mean shear stress structure in the shear layer of both jets, the two-point spatial correlation was computed at the probe point selected for each jet, the results of which are displayed in Fig. 9.

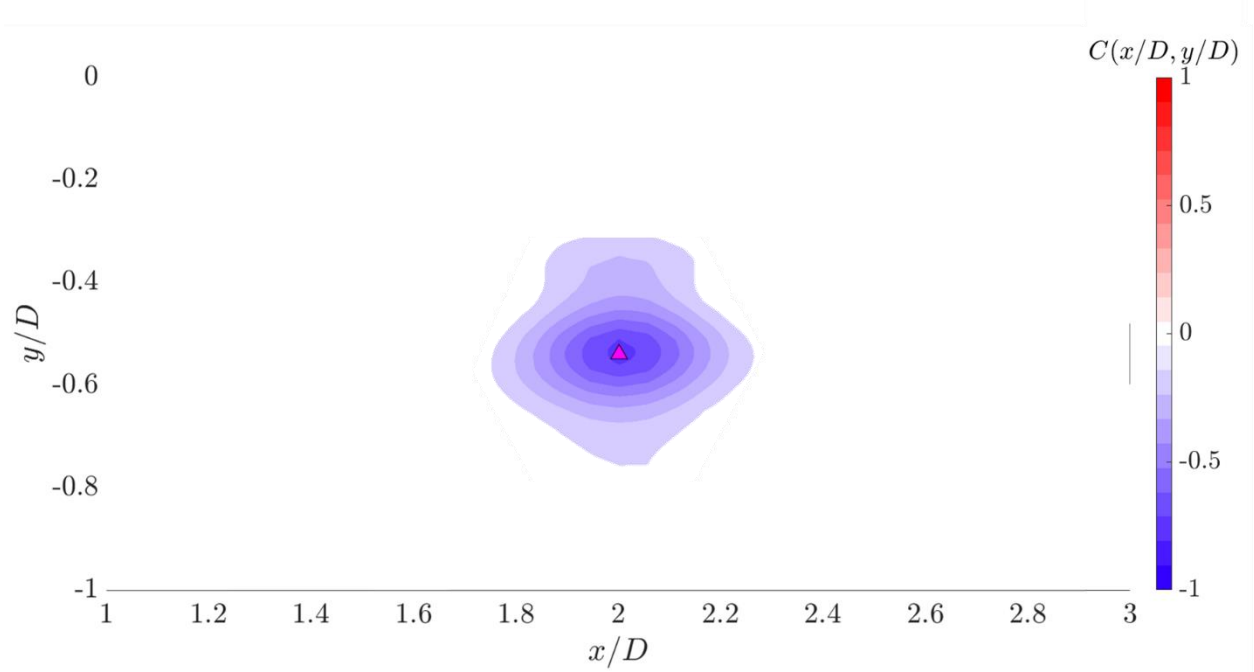

(a)

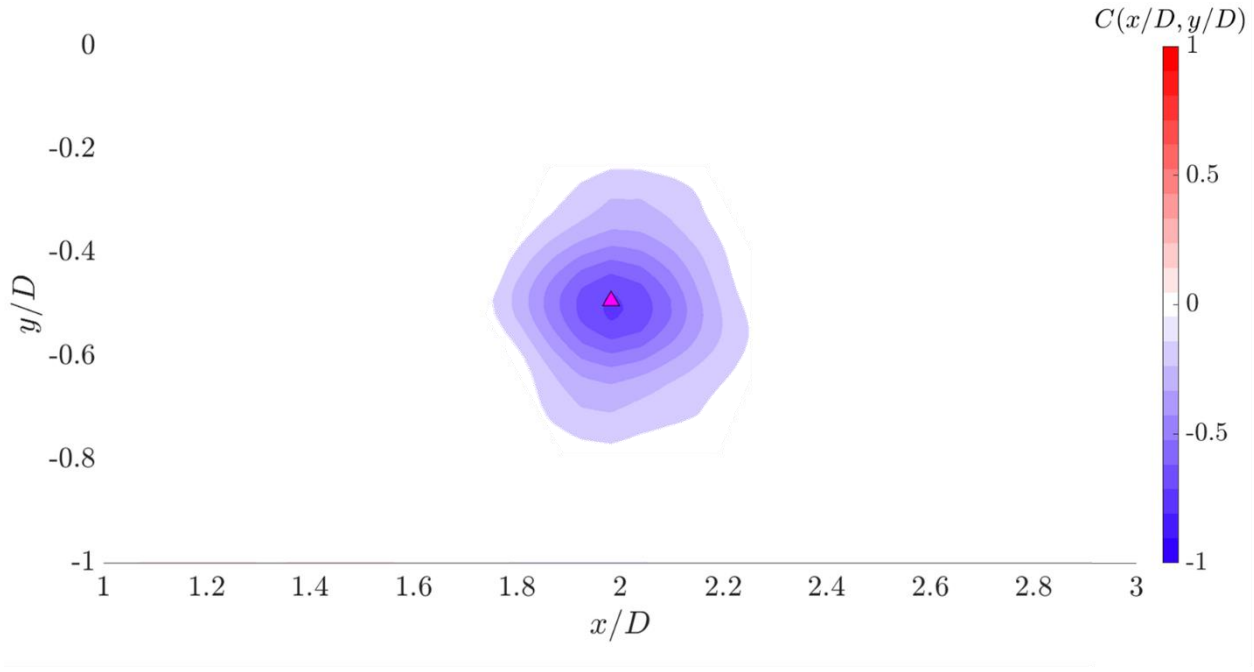

(b)

Fig. 9. Two-point cross-correlation coefficient maps for the uniform (a) and thermally offset (b) jets with the probe point for both jets marked (magenta)

Figure 9 contains the two-point correlation coefficient distributions for both the uniform (a) and offset (b) jets at the probe point marked in magenta. Table 3 contains the cross-correlation coefficient and the axial and transverse integral length scales for both the uniform and offset jets computed from the two-point correlation at the probe point

using Eq. 1. The first observation of note is that the peak correlation value for both jets ($C(r/D = 0)$) are both anti-correlated and have similar values which implies that the axial fluctuations are increasing in intensity faster than the transverse fluctuations, which is to be expected in high-speed jet flows. More interesting is that, due to both jets having the same correlation value, the intensities of the integrated turbulence structure at the probe location are evolving at the same rate.

Table 3. Correlation coefficient and integral length scales for the uniform and thermally offset jets at the probe point

	$Uniform$	$Offset$
$\boldsymbol{C}(x/D, y/D)$	-0.76	-0.74
L_x/D	0.23	0.22
L_y/D	0.095	0.12

The axial length scale , L_x/D is effectively unchanged between thermally offset and uniform jets. Conversely, the transverse length scale, L_y/D, is 26% longer in the offset jet compared to the uniform. The difference in L_y/D between the two jets is expected as the shear layer is thicker for the offset jet at x/D = 2. The similarity in the L_x/D and the peak correlation value provides evidence that the evolution of the axial turbulence is driven by scaling between U_j and the ambient and is no longer dictated by the secondary plume velocity, U_s. Quadrant analysis will be employed to evaluate the statistical nature of the mean turbulence structure.

D. Quadrant Fraction Statistics in the Near Nozzle Developmental Region

Given the sample sizes available, the statistical error in the conditional averages were decreased by reducing the spatial resolution by half, doubling the number of samples represented at each resolved vector location. After applying the technique to the data, the effective number of samples at each location increased to 4,000.

Before investigating results of the quadrant analysis at the selected probe points, a transverse sensitivity study at $x/D = 2$ was performed. The quadrant fraction is the ratio of the number of samples in a quadrant, at the selected probe point, to the total number of samples at the probe point. Fig. 10 presents the transverse evolution of the quadrant fraction as one moves from ambient, on the left, towards the centerline on the right and their values are given on the right ordinate. Overlaid on this plot are the axial velocity profiles of the uniform and offset jets for reference of the mean velocity behavior, the scale of which is given on the left ordinate and the transverse location of the probe point is marked by the vertical dashed line. The first observation of note is that at the transverse probe point location, the Q1 vs Q3 and Q2 vs Q4 events occur equally often in the jet shear layer—i.e., both are contributing a maximum

amount. Entrainment motions are observed more often towards ambient and ejection motions occur more often towards the centerline from the probe point. This implies that fluid is being drawn towards the peak shear stress location both from the ambient as well as from the potential core. This behavior is expected as entrainment is the primary mechanism for shear layer growth in free jets [26]. Towards the centerline of the jet, smaller ejection peaks can be observed in the offset jet which are not present in the uniform jet which are caused by the turbulence introduced by the secondary plume.

The peak in the number of detected forward ejection (Q4) events in both jets coincides with the maxima of the $\partial \bar{U}_x/\partial y$ velocity gradient in both jets (y/D ~ 0.52 in the uniform jet and y/D ~ 0.45 in the offset jet). The $\partial \bar{U}_x/\partial y$ gradient is closely associated with the Q4 events since the forward ejection occurrence increases in the region the gradient slope is negative and decays when the gradient has a positive slope. The observations about the relationships between local velocity gradient changes and Q4 events are consistent with the physics of ejection events which have been observed in boundary layer flows [17,27,28].

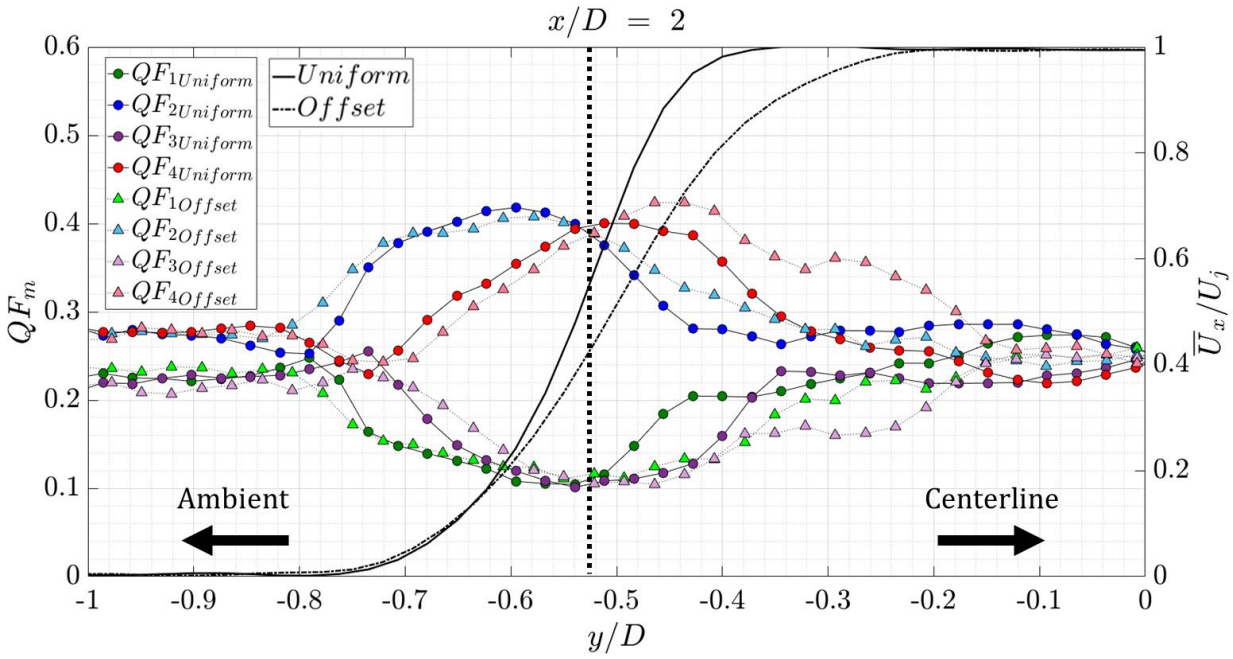

Fig. 10. Transverse evolution of the quadrant fraction in the uniform and thermally offset jets at x/D = 2 with the probe point location marked (---)

Figure 11 presents phase plots between the fluctuating axial and transverse velocities in the uniform and offset jets at the probe point. The data points in each quadrant are color coded based on the quadrants in which each data point lies after performing quadrant analysis. The legends provide the quadrant fractions for both jets and as noted

before, the opposing motions, Q1 vs Q3 and Q2 vs Q4, occur equally often. The reverse entrainment and forward ejection events combined (Q2 and Q4) are observed nearly 80% of the time in both jets, their conditionally averaged structure will be negatively valued, and they contribute the majority of the $\overline{u_x' u_y'}$ shear stress in the shear layer of both jets. The forward entrainment and reverse ejection events (Q1 and Q3) occur a combined 20% of the time and their conditionally averaged structure at the probe point is positive, which acts against the mean shear stress and serves to lower the peak value. It is important to note that summing the conditionally averaged shear stresses together recovers the total shear stress in the flow field.

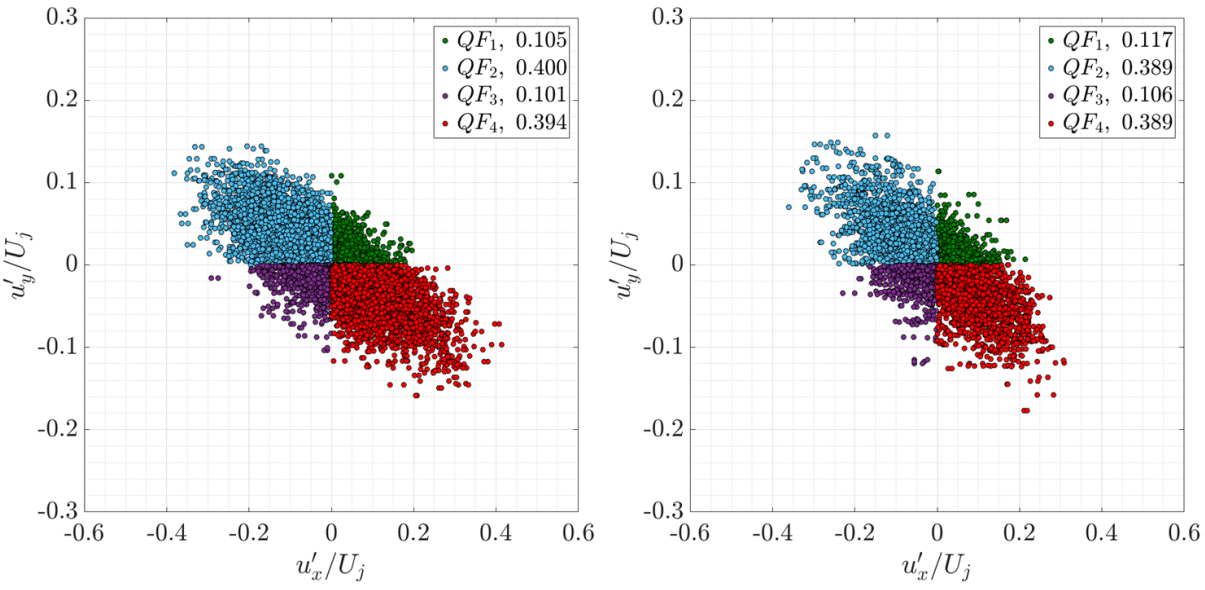

(a) **(b)**

Fig. 11. Fluctuating velocity scatterplots of the uniform (a) and thermally offset (b) jets.

E. Structure of Dominant Q1 and Q3 Events

To gain insight into the underlying statistical structure of the shear stress, the conditional average was computed and analyzed for each of the four quadrants, and the dominant motions are compared with one another. Figure 10 contains forward entrainment (Q1) and reverse ejection (Q3) conditionally averaged shear stress structures for the uniform (a and d) and thermally offset (b and e) jets. The streamlines[29] in Figs. 12 and 14 are computed from the conditionally averaged $\widetilde{u_x'}$ and $\widetilde{u_y'}$ vectors associated with each quadrant. The initial conditions for the streamlines were seeded at x/D = 0 and seeding was evenly spaced along the entire y/D domain thus ensuring that the spacing between the streamlines is indicative of changes of the in-plane flow rate.

The spatial structure revealed by the conditional averages reveal an interesting wavepacket-like pattern in both jets. A positive shear stress event occurs at the probe point located at the center of each plot. Upstream and downstream of the positive stress structure, two lobes of negative stress are present in the flow field. The rapid shift in the transverse signs of the shear stress event reveal an axially varying wavepacket-like structure in the Q1 and Q3 structures. The streamlines in the uniform jet are consistent with the presence of azimuthally rotating vortices which surround the shear stress event and accelerate the flow between them, producing a pinching motion. For the uniform jet, the vortices observed in the Q1 structure are all sources and in the Q3 structure are all sinks –i.e. the vortices respectively transport turbulence into or out of the measurement plane.

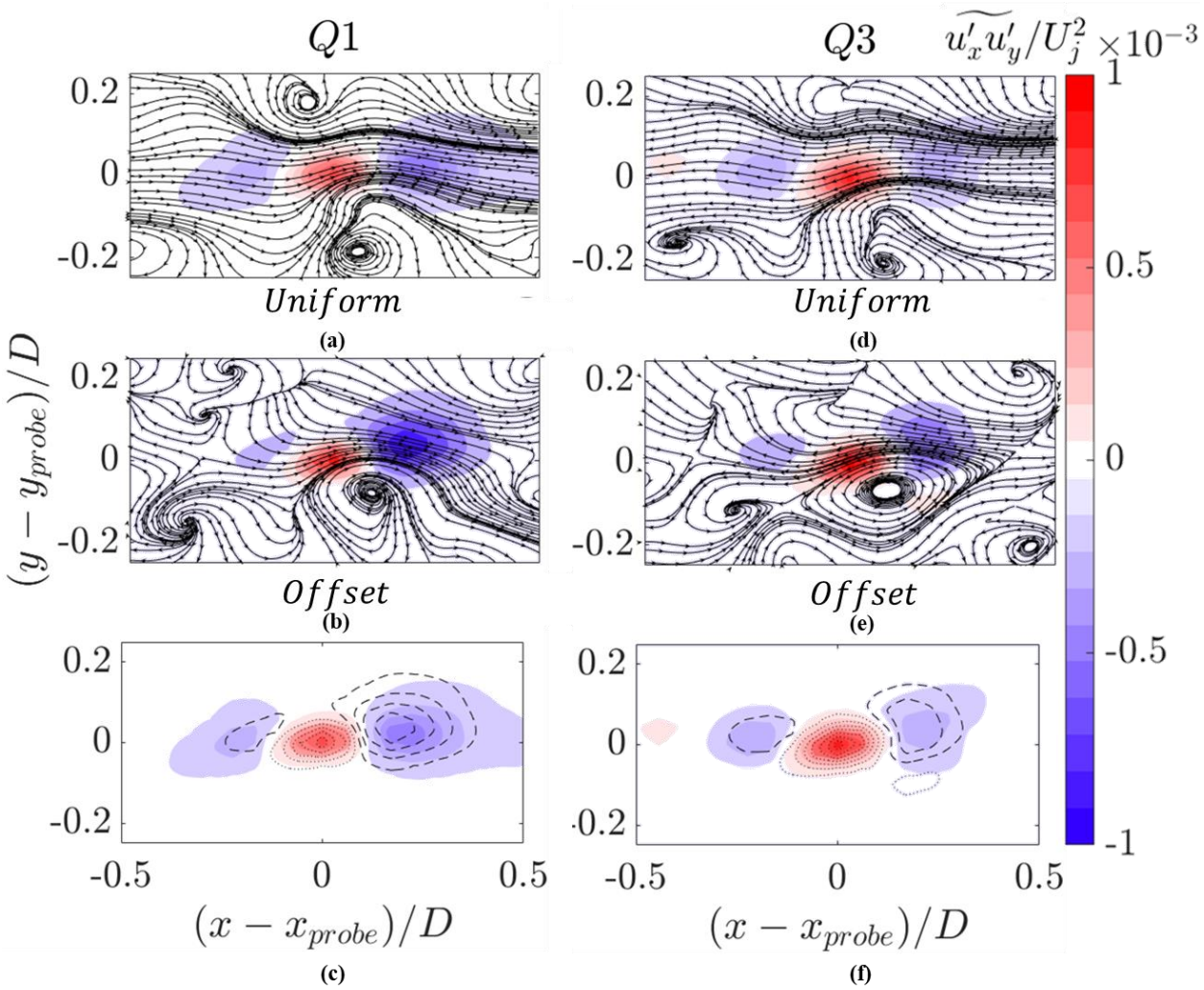

Fig. 12. Conditionally averaged plots for the forward entrainment (Q1) and reverse ejection (Q3) shear stress events in the uniform, (a) and (d), and offset, (b) and (e), jets at the probe point. Figures (c) and (f) show the offset contour (dashed) overlaid on top of the uniform contour (colored) for each case.

The Q1 (forward entrainment) and Q3 (reverse ejection) shear stress structures are overlaid in Figs. 12 (c) and (f) respectively for the uniform and offset jets, revealing notable differences. The upstream forward ejection lobe in the uniform jet has a smaller peak magnitude and larger spatial extent compared to the same lobe in the offset jet, whereas the opposite is true for the downstream forward ejection lobes. These observations could suggest that more fluid is being entrained into the pinching motion in the offset jet compared to the uniform case while still producing the same magnitude of peak positive shear stress. Ultimately, the mean flow motions of the Q1 shear stress structures for both jets reveal a general transport of momentum in the stream-wise direction, with little radial transport into or out of the structure.

In the offset jet (Figs. 12 (b) and (e)), the streamlines exhibit more chaotic behavior than in the uniform case. In the offset jet figures, there are regions where the streamlines converge, either to a point or follow a singular path. The point convergences are nodes, and they occur when flow in the axial/transverse plane is being turned into the azimuthal direction or vice versa. The path convergences are typically associated with the presence of stream-wise vortical structures in a flow field. The prevalence of these structures in the offset jet structures show that there is an increase in the three-dimensionality of the turbulence in the offset jet caused by the asymmetry introduced compared to the uniform jet. Additionally, source and sink vortices populate the observable domain of both the Q1 and Q3 structures in the offset jet, unlike the changes revealed in the uniform jet.

The overall structure of the reverse ejection (Q3) events shown in Fig. 12 (d)-(f) is similar to the forward ejection (Q1) events, but opposite in motion. The peak values and spatial extent of the leading and trailing reverse entrainment motions are significantly smaller than their Q1 counterparts. The reduction in the reverse entrainment lobe sizes may be due to the associated motions acting opposite of the local mean $\partial \overline{U}_x/\partial x$ gradient.

Figure 13 shows a hypothesized mechanism for the production of stream-wise vortices in the offset jet. In the near nozzle region of the uniform jet, azimuthal vortices are formed due to Kelvin-Helmholtz instability in the shear layer (Fig. 13 (a)). When an offset cold plume is introduced into the flow field, the azimuthal vortices that form convect at a slower speed in this region which causes the vortex to be stretched axially, forming short lived stream-wise vortices shown in Fig. 13 (b).

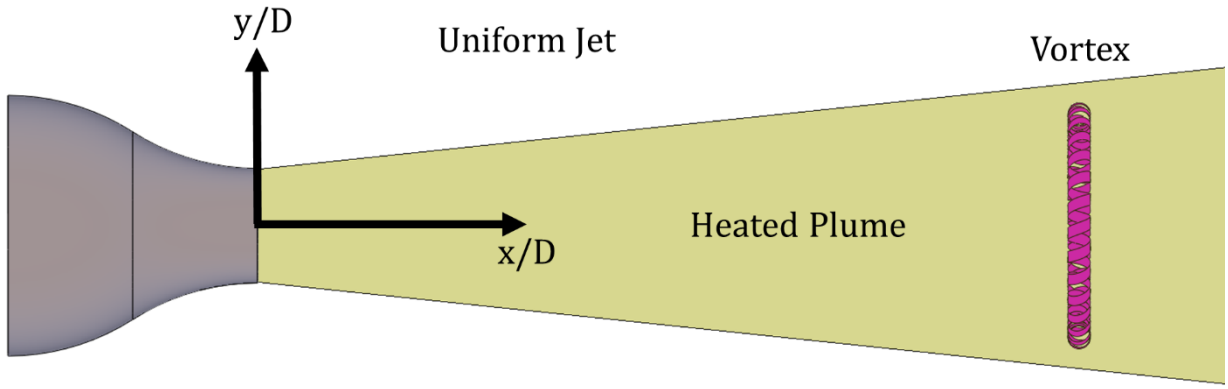

(a)

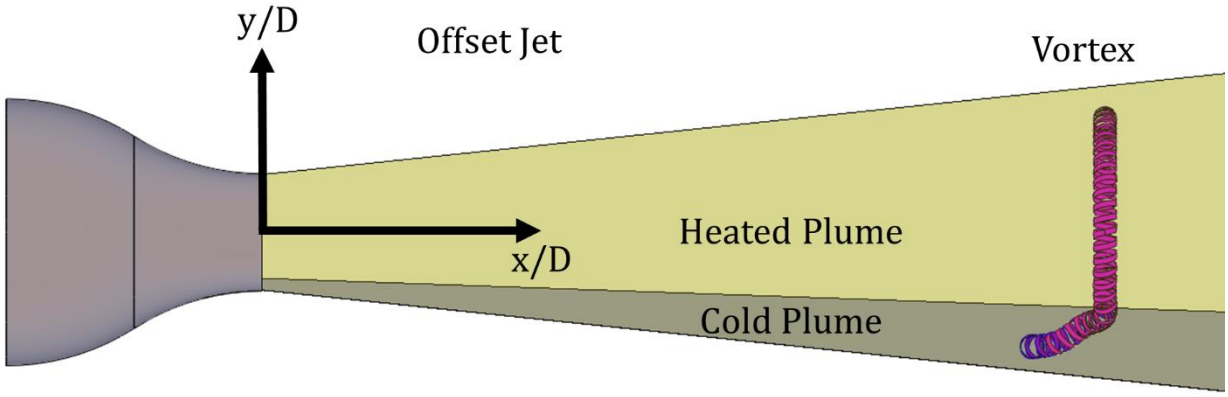

(b)

Fig. 13. Hypothetical mechanism for the formation of stream-wise vortices in the offset jet

The authors suppose that the local acceleration between the vortical structures result in turbulent motions with supersonic phase speeds which produce shear stress opposite the sign of the mean at that location [30] (positive shear stress in a mean negative shear stress region). The event converts some of the turbulent kinetic energy into acoustic energy that is radiated to the far-field due to the local acceleration of the turbulence between the vortices [31]. The cooler secondary plume present in the thermally offset jet reduces the strength of the vortices by increasing the entrainment of colder, lower momentum fluid into the shear layer compared to the uniform jet, which reduces the size and intensity of the shear stress turbulent structures and results in a reduction of noise produced by the Q1 and Q3 events.

F. Structure of Dominant Shear Stress Producing Events (Q2 and Q4 Events)

Figure 14 shows the conditionally averaged contour plots of the reverse entrainment (Q2) and the forward ejection (Q4) events of the uniform, (a) and (d), and offset, (b) and (e), jets. The overlaid streamlines reveal the statistical mean structure of the $\widetilde{u_x'}$ and $\widetilde{u_y'}$ conditional averages associated with quadrants analyzed. The initial seeding for the overlaid streamlines were equally spaced so the variations in the spacing directly reflect increases or decreases in flow rate. The Q2 and Q4 structures are compared with one another as the direction of the motions oppose one another.

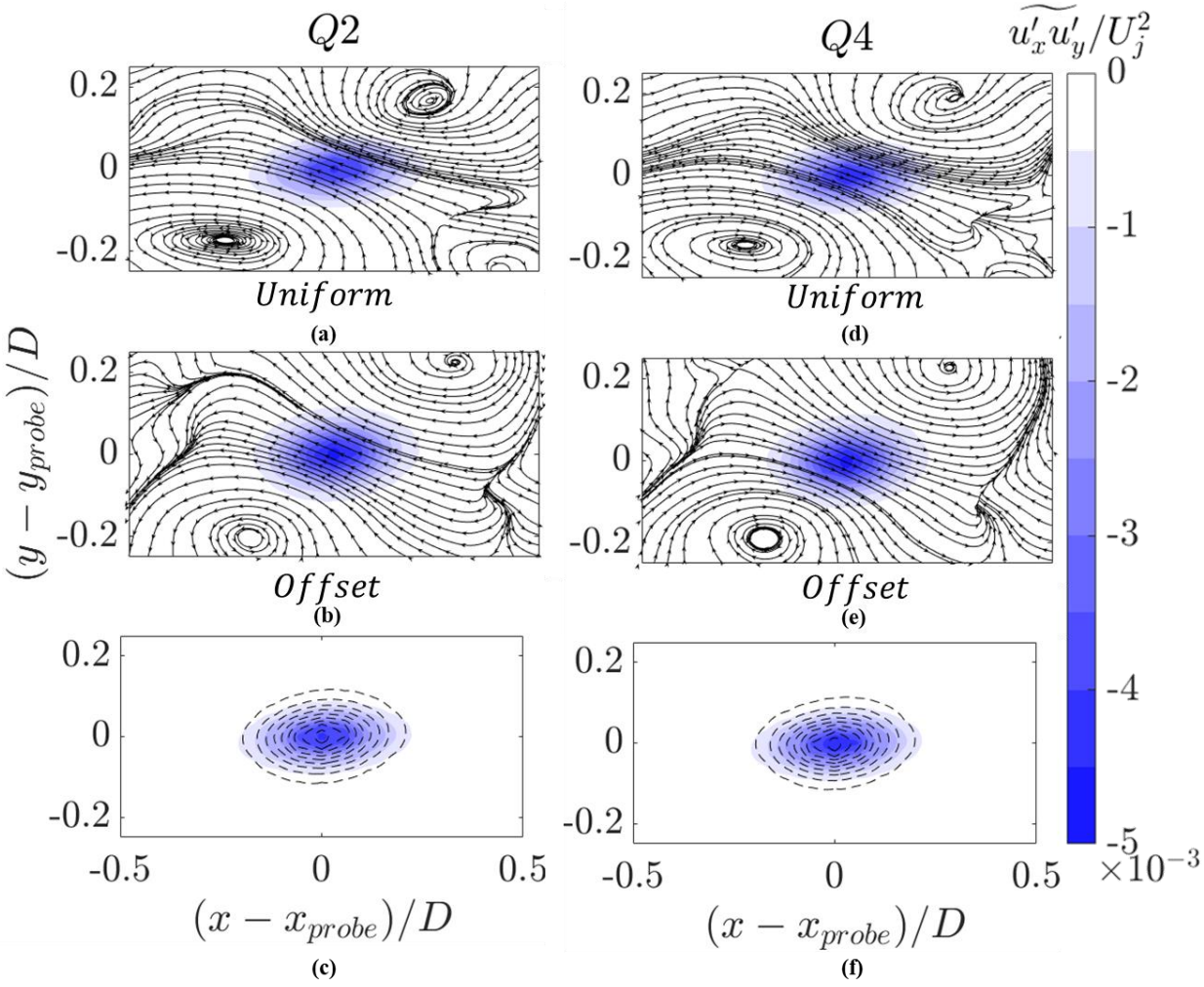

Fig. 14. Conditionally averaged plots for the reverse entrainment (Q2) and forward ejection (Q4) shear stress events in the uniform, (a) and (d), and offset, (b) and (e), jets at the probe point. Figures (c) and (f) show the offset contour (dashed) overlaid on top of the uniform contour (colored) for each case.

Reverse entrainment (Fig. 14 (a) and 14 (b)) and forward ejection (Fig. 14 (d) and 14 (e) motions dominate the domain of the shear stress structures in both jets, with a counter-rotating vortex pair bracketing the conditionally averaged Q2 and Q4 structures. In comparing the spacing of the streamlines of the uniform jet structures (Fig. 14 (a)

and 14 (d)), it can be observed that the streamlines in the center of the plots are denser for the Q4 event compared to the Q2 event, indicating a greater influence on entrainment in the downstream portion of the lobe that correlates with the condition at this probe point.

A counter-rotating vortex pair bracket the conditionally averaged Q2 and Q4 structures in both jet flows. In the offset jet (Fig 14 (b) and (e)), the vortices are larger and their associated streamline spacing is less dense than in the uniform jet, which indicates a reduction in vortex strength associated with these motions. Ultimately, the presence of the slower velocity cold plume in the offset jet changed the turbulence length scales, which is evidenced by the longer transverse and shorter axial extent of the conditionally averaged structures in the offset jet compared to the uniform, which can be seen in Fig. 14 (c) and 14 (f).

VI.Conclusion

An experimental study of conditionally averaged shear stress events measuring using PIV in a Mach 1.5 supersonic heated jet with an offset total temperature non-uniformity was conducted and compared to a uniform total temperature profile jet flow. A review of the mean flow characteristics revealed a reduction in the mean $\overline{U}_x$ velocity profile which caused a decrease in the mean shear stress in the offset jet when compared to the uniform case. Measurements of the vorticity thickness and growth rate near the jet nozzle revealed a much thicker shear layer and a slightly reduced entrainment rate in the offset jet compared to the uniform case, caused by the presence of the colder velocity fluid injected from the secondary nozzle.

To investigate the changes in the turbulent structure, a probe point in each jet was selected at 2 diameters from the nozzle exit and the transverse location where maximum transverse shear stress was located, and quadrant analysis was applied. Quadrant analysis is a conditional averaging technique, used extensively in wall-bounded flows, which filters the u'_x and u'_y signals into four bins, or quadrants, based on the signs of the fluctuation pairs. In this study, the motions of the four quadrants are Q1 ($u'_x > 0, u'_y > 0$) forward entrainment, Q2 ($u'_x > 0, u'_y < 0$) reverse entrainment, Q3 ($u'_x < 0, u'_y < 0$) reverse ejection, Q4 ($u'_x > 0, u'_y < 0$) forward ejection; where forward and reverse refer to axial motions moving downstream or upstream and entrainment and ejection refer to transverse motions moving towards or away from the jet centerline.

The vortices that were observed in the statistical structures obtained from the Q1 and Q3 quadrants are seen to induce pinching motions in the flow characterized by rapid acceleration and deceleration of turbulence in a small

spatial region. An increase in three-dimensionality of the turbulence was observed in the offset jet which altered the strength and spatial extent of structures observed. It is hypothesized that the reduction of the vortex strength in the offset jet could contribute to a reduction in far-field radiated noise.

The conditionally averaged reverse entrainment (Q2) and forward ejection (Q4) shear stress contours revealed counter-rotating vortex pairing which facilitated entrainment of fluid into, and ejection of fluid out of, the jet shear layers. These structures produce the bulk of the $\overline{u_x' u_y'}$ stress in the shear layer and the presence of the secondary plume in the offset jet reduced the strength of these motions.

The evidence presented in this study reveals a small, but significant change in the shear stress structures of the thermally offset jet compared to the uniform case. The alterations to the size and intensity of the turbulence are due to an increase in the three-dimensionality of the shear stress flow field, caused by the presence of stream-wise vortical structures. The vortical structures redistribute some of the $\overline{u_x' u_y'}$ turbulent energy into the $\overline{u_\theta'}$ direction which has been shown as a mechanism for noise reduction in jet flows.

Acknowledgments

This work was sponsored by the U.S. Office of Naval Research, program manager Dr. Steven Martens, via grants N00014-16-1-2444 and N00014-14-1-2836.

References

[1] Daniel, K. A., Mayo Jr., D. E., Lowe, K. T., and Ng, W. F., 2019, "Use of Thermal Non-Uniformity to Reduce Supersonic Jet Noise," *AIAA J.* (not yet published)

[2] Mayo Jr., D.E., Daniel,K., Lowe,K.T., and Ng,W.F., "The Flow and Turbulence Characteristics of a Heated Supersonic Jet with an Offset Total Temperature Non-Uniformity," *AIAA Journal*, May 2019. doi: 10.2514/6.2018-3144

[3] Alkislar, M. B., Krothapalli, A., and Butler, G. W., "The Effect of Streamwise Vortices on the Aeroacoustics of a Mach 0.9 Jet," *Journal of Fluid Mechanics*, Vol. 578, May 2007, pp. 139-169. doi: 10.1017/S0022112007005022

[4] Arakeri, V. H., Krothapalli, A., Siddavaram, V., Alkislar, M. B., and Lourenco, L. M., "On the Use of Microjets to Suppress Turbulence in a Mach 0.9 Axisymmetric Jet," *Journal of Fluid Mechanics*, Vol. 490, Oct. 2003,

pp. 75–98. doi: 10.1017/s0022112003005202

[5] Powers, R. W., Kuo, C.W., and Mclaughlin, D. K., “Experimental Comparison of Supersonic Jets Exhausting from Military Style Nozzles with Interior Corrugations and Fluidic Inserts,” *19th AIAA/CEAS Aeroacoustics Conference*, May 2013. doi: 10.2514/6.2013-2186.

[5] Stuber, M., Ng, W. F., and Lowe, K. T., “Synthesis of Convection Velocity and Turbulence Measurements in Three-Stream Jets for Investigation of Noise Sources,” *Experiments in Fluids*, 2019. (not yet published).

[6] Papamoschou, D., and Phong, V. C., “The Very Near Pressure Field of Single- and Multi-Stream Jets,” *55th AIAA Aerospace Sciences Meeting*, January 2017. doi: 10.2514/6.2017-0230

[7] Henderson, B. S., and Leib, S. J., “Measurements and Predictions of the Noise from Three-Stream Jets,” *21st AIAA/CEAS Aeroacoustics Conference*, May 2015. doi: 10.2514/6.2015-3120

[8] Tanna, H. K., Tester, B. J., Lau, J.C., "The Noise and Flow Characteristics of Inverted-Profile Coannular Jets," NASA-CR-158995, February 1979.

[9] Tanna, H. K., and Morris, P. J., “The Noise from Normal-Velocity-Profile Coannular Jets,” *Journal of Sound and Vibration*, Vol. 98, No. 2, January 1985, pp. 213–234. doi: 10.1016/0022-460X(85)90386-4

[10] Maus, J. R., Goethert, B. H., and Sundaram, C. V., “Noise Characteristics of Coannular Flows with Conventional and Inverted Velocity Profiles,” *Journal of Aircraft,* Vol. 18, No. 2, February 1981, pp. 135–141. doi: 10.2514/3.57474.

[12] Dahl, M. D., *The Aeroacoustics of Supersonic Coaxial Jets*, NASA-TM-106782, November 1994.

[13] Bhat, T., and Seiner, J., 1993, “The Effect of Velocity Profiles on Supersonic Jet Noise,” *15th Aeroacoustics Conference*, October 1993. doi: 10.2514/6.1993-4410

[14] Daniel, K.A., Mayo Jr., D.E., Lowe, K.T., and Ng, W.F., “Experimental Investigation of the Very Near Pressure Field of a Heated Supersonic Jet with a Total Temperature Non-Uniformity,” *2018 AIAA/CEAS Aeroacoustics Conference*., June 2018, doi: 10.2514/6.2018-3145..

[15] Tamm, P., Bres, G. A., Towne, A., and Lele, S. K., “Leveraging Large-Eddy Simulations to Investigate the Influence of Temperature Non-Uniformity on Jet Noise,” *Center for Turbulence Research Proceedings of the Summer Program 2018*, 2018, pp. 175–184.

[16] Papamoschou, D., “Modelling of Noise Reduction in Complex Multistream Jets,” *Journal of Fluid Mechanics*, Vol. 834, January 2018, pp. 555–599. doi: 10.1017/jfm.2017.73

[17] Wallace, J. M., Eckelmann, H., and Brodkey, R. S., 1972, "The Wall Region in Turbulent Shear Flow," *Journal of Fluid Mechanics*, Vol. 54, No. 1, July 1972, pp. 39–48. doi: 10.1017/S0022112072000515

[18] Wallace, J. M., 2016, "Quadrant Analysis in Turbulence Research: History and Evolution," *Annual Review of Fluid Mechanics*, Vol. 48, No. 1, January 2016, pp. 131–158. doi: 10.1146/annurev-fluid-122414-03455

[19] Antonia, R. A., and Browne, L. W. B., "Quadrant Analysis in the Turbulent Far-Wake of a Cylinder," *Fluid Dynamics Research*,Vol. 2, No. 1, January 1987, pp. 3–14. doi: 10.1016/0169-5983(87)90013-X

[20] Loucks, R. B., and Wallace, J. M., "Velocity and Velocity Gradient Based Properties of a Turbulent Plane Mixing Layer," *Journal of Fluid Mechanics*, Vol. 699, May 2012, pp. 280–319. doi: 10.1017/jfm.2012.103

[21] Örlü, R., and Alfredsson, P. H., 2008, "An Experimental Study of the Near-Field Mixing Characteristics of a Swirling Jet," Flow, Turbulence and Combustion., Vol. 80, No. 3, April 2008, pp. 323–350. doi: 10.1007/s10494-007-9126-y

[22] Viggiano, B., Dib, T., Ali, N., Mastin, L. G., Cal, R. B., and Solovitz, S. A., "Turbulence, Entrainment and Low-Order Description of a Transitional Variable-Density Jet," *Journal of Fluid Mechanics*, Vol. 836, February 2018, pp. 1009–1049. doi: 10.1017/jfm.2017.822

[23] Sreenivasan, K. R., and Antonia, R. A., 1978, "Joint Probability Densities and Quadrant Contributions in a Heated Turbulent Round Jet," *AIAA Journal*, Vol. 16, No. 9, September 1978, pp. 867–868. doi: 10.2514/3.60976

[24] Bendat, J.S., Allan, G. P., *Random Data: Analysis and Measurement Procedures*, 4th ed., Wiley, New York, February 2010. doi: 10.1002/9781118032428

[25] Brown, G. L., and Roshko, A., 1974, "On Density Effects and Large Structure in Turbulent Mixing Layers," *Journal of Fluid Mechanics*, Vol. 64, No. 4, July 1974, p. 775-816.

[26] Tennekes, H., Lumley, J.L., *A First Course in Turbulence*, MIT Press, Cambridge, MA, 1972,

[27] Kline, S. J., Reynolds, W. C., Schraub, F. A., and Runstadler, P. W., "The Structure of Turbulent Boundary Layers," *Journal of Fluid Mechanics*, Vol. 30, No. 4, December 1967, pp. 741-773. doi: 10.1017/S0022112067001740

[28] Corino, E. R., and Brodkey, R. S., "A Visual Investigation of the Wall Region in Turbulent Flow," *Journal of Fluid Mechanics*, Vol. 37, No. 1, June 1969 , pp. 1–30. doi: 10.1017/S0022112069000395.

[29] Jobard, B., and Lefer, W., 1997, "Creating Evenly-Spaced Streamlines of Arbitrary Density," Springer,

Vienna, pp. 43–55.

[30] Bernard, P.S., Thomas, J.M., Handler, R.A., “Vortex Dynamics and the Production of Reynolds Stress,” *Journal of Fluid Mechanics*, Vol. 253, August 1993, pp. 385–419. doi: 10.1017/S0022112093001843

[31] Chu, B.B., and Kovasznay, L.S.G., “Non-Linear Interactions in a Viscous Heat-Conducting Compressible Gas,” *Journal of Fluid Mechanics*, Vol. 3, No. 5, Feburary 1958**,** pp. 494–514. doi: 10.1017/S002211205800014.

Appendix

A. Supersonic Heated Jet Rig Setup

The Virginia Tech Heated Jet Rig, shown schematically in Figure A.1, at the Advanced Power and Propulsion Laboratory (APPL) was used to conduct the experiments presented in this dissertation. A round contour nozzle, designed using the axisymmetric method of characteristics ($D = 38.1\,mm$) by Kuo et al. [1], was scaled and manufactured for the rig. The primary nozzle provides a uniform Mach 1.5 exit profile at perfectly expanded conditions.

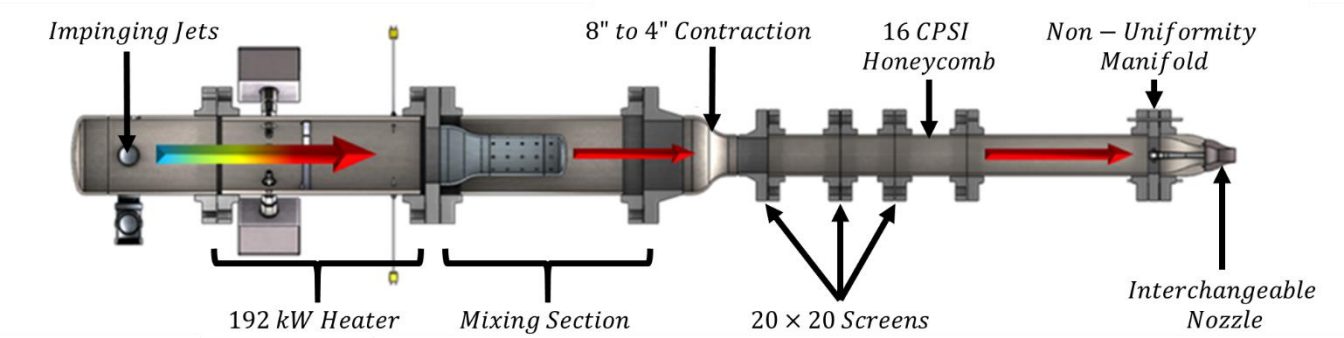

Fig. A.1. Diagram of Virginia Tech Hot Jet Rig

A converging secondary jet nozzle ($d = 8.38\,mm$) internal to the primary plenum was designed, manufactured, and added to this rig to introduce a total temperature non-uniformity within the heated primary jet flow (see Figure 2). Unheated air is supplied to the nozzle through a secondary plenum. The flow enters the non-uniformity manifold, impinges mixes with each other then turns 90° into a flow straightener before being exhausted through the nozzle. The nozzle of the secondary jet stream was terminated at the inlet of the primary nozzle, upstream of the converging portion of the converging-diverging nozzle, as shown in Figure A.2.

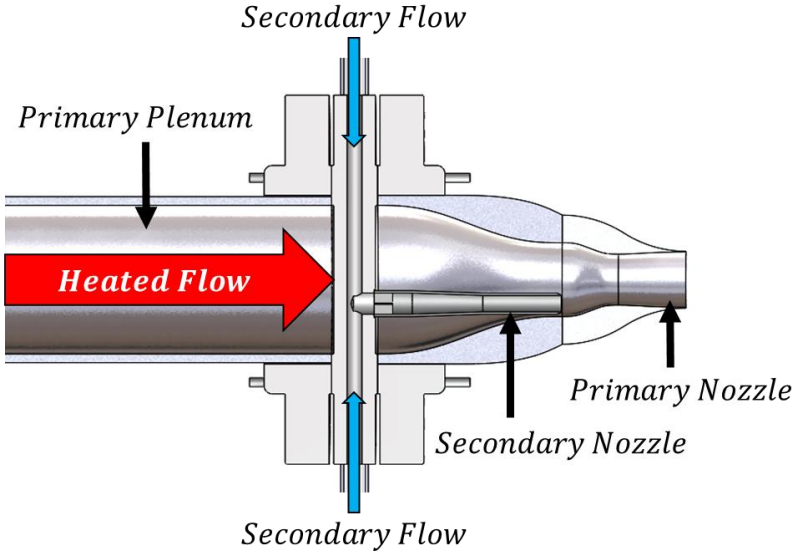

Fig. A.2. Diagram of the coaxial jet geometry

A National Instruments (NI) 9213 thermocouple module in a NI cDAQ-9184 chassis was used to measure total temperature data in the primary and secondary jet plenums, while total pressures of both core and secondary streams

were measured using a Scanivalve Corp. ZOC17IP/8Px-APC pressure scanner. The mass flow rate of the cold secondary stream is measured using static pressure and total temperature measurements collected from a Lambda-Square venturi meter in order to improve the accuracy of the mass flow rate estimations in the secondary plume. The temperature and pressure data were recorded using a NI PXIe-6358 DAQ installed in a NI PXIe-8133 computer data acquisition system.

References

[1] Kuo, C.W., McLaughlin, D. K., Morris, P. J., & Viswanathan, K. 2014. Effects of Jet Temperature on Broadband Shock-Associated Noise. Aiaa Journal, 53(6), 1–16.

B. Computing Flow Properties in the Supersonic Jet

Atmospheric pressure measurements were computed from the altimeter pressure readings reported by the National Weather Service Forecast Office in Blacksburg VA. The measurements were acquired at the Virginia Tech Airport, located ~0.5 miles from the testing site and updated every 20 minutes. The following formula [1] provided by the National Oceanic and Atmospheric Administration was used to numerically find the atmospheric pressure (p_{atm}) to from the altimeter pressure (P_{alt}) in inHg. The variable h is the altitude of the airport from sea level in meters.

$$p_{alt} = [p_{atm} - 0.3]\left[1 + \left(\left[\frac{(1013.25^{0.190284})(0.0065)}{288}\right]\left[\frac{h}{(p_{atm} - 0.3)\text{^}0.190284}\right]\right)\right] \times 100 \qquad \text{E.1}$$

Except where noted, the isentropic Mach relations were used to estimate the aero-thermodynamic conditions of the jet presented below [2]. The ideal gas law was used to acquire the static density at key points in both the primary and secondary plenums for calculation of the jet mass flow rates. R is the ideal gas constant for air.

$$p = \rho RT \qquad \text{E.2}$$

The primary plenum nozzle pressure ratio (NPR) was computed from the computed atmospheric pressure and the total pressure probe measurements (p_p) acquired.

$$NPR_p = \frac{p_p}{p_{atm}} \qquad \text{E.3}$$

The total temperature ratio for the primary jet flow (TTR) was computed from total temperature (T_p) probe measurements acquired from a probe mounted in the hot jet plenum and a static temperature probe (T_{atm}) mounted in the room where the hot jet is located.

$$TTR_p = \frac{T_p}{T_{atm}} \qquad \text{E.4}$$

The isentropic Mach number for the primary jet was determined using the following equation. γ is the adiabatic ratio which for air is 1.4.

$$M_j = \sqrt{\frac{2}{\gamma - 1}\left(\frac{p_p}{p_{atm}}\right)^{\frac{\gamma-1}{\gamma}} - 1} \qquad \text{E.5}$$

The isentropic jet temperature for the heated plume was calculated using the following formula. This is needed to compute the Reynolds number of the jet.

$$T_j = T_p\left(1 + \frac{\gamma - 1}{2}M_j^2\right)^{-1} \qquad \text{E.6}$$

The isentropic jet velocity for the primary jet plume was determined using the following equation.

$$U_j = M_j\sqrt{\gamma RT_j} \qquad \text{E.7}$$

The following formula [3] was used to compute the mass flow rate for the secondary plenum from the Lambda-Square orifice meter. p_h and p_l are respectively the upstream and downstream static pressure taps in the orifice meter.

The density (ρ_o) in the orifice of the meter was calculated using the ideal gas law and the static pressure and temperature measurements in the secondary plenum.

$$\dot{m}_s = C_o A_o \sqrt{2\rho_o p_h \left(\frac{\gamma}{\gamma-1}\right)\left(\left(\frac{p_l}{p_h}\right)^{\frac{2}{\gamma}} - \left(\frac{p_l}{p_h}\right)^{\frac{\gamma}{\gamma-1}}\right)} \quad \text{E.8}$$

For the thermally offset jet, since both the primary and secondary jet flows exit through the same orifice, a reduced effective exit area was computed for the primary jet flow to account for this discrepancy. Assuming that there was minimal mixing between the two flow streams in the nozzle and the two flows follow streamlines, the effective exit area was computed using the following equation. D_i and D_j are the inlet and exit diameter of the primary jet nozzle respectively.

$$A_{eff} = A_j - A_d \left(\frac{D_j}{D_i}\right)^2 \quad \text{E.9}$$

The isentropic Mach relations were used to compute the mass flow rate of the primary plenum flow. For the uniform jet, the nozzle exit area was used. For the offset jet, the effective nozzle exit area was used.

$$\dot{m}_p = p_p M_j A \sqrt{\frac{\gamma}{RT_p}} \left(1 + \frac{\gamma-1}{2} M_j^2\right)^{\frac{\gamma+1}{2(\gamma-1)}} \quad \text{E.10}$$

The dynamic viscosity (μ_p) of the primary jet flow was computed using total temperature measurements and Sutherland's formula [4]. T_j is the exit static temperature of the primary jet plume.

$$\mu_p = \frac{(1.512014288 \times 10^{-6})\left(T_j^{\frac{3}{2}}\right)}{T_j + 120} \quad \text{E.11}$$

The exit Reynolds number (Re_j) was computed using the following formula and only used the primary heated plume properties. The jet exit density (ρ_j) was determined using the ideal gas law. The effective exit diameter was used for the thermally offset jet and the total exit diameter was used for the uniform jet.

$$Re_j = \frac{\rho_j U_j D}{\mu_j} \quad \text{E.12}$$

References

[1] Brice, T., Hall, T., 2018, Altimeter Setting Calculator, Weather.gov [Online], Available: https://www.weather.gov/media/epz/wxcalc/altimeterSetting.pdf [Accessed: 4 June 2019].
[2] Shapiro, A.H., 1953, The Dynamics and Thermodynamics of Compressible Fluid Flow, 1st Edition. Wiley.
[3] Handbook of Chemical Hazard Analysis Procedures, Appendix B, Federal Emergency Management Agency, U.S. Dept. of Transportation and U.S. Environmental Protection Agency, 1989, pp. 394.
[4] Sutherland, W., 1893, The Viscosity of Gasses and Molecular Force, Philosophical Magazine, 5 (36), pp. 507-531.

C. Supersonic Jet PIV Data Acquisition Setup

The PIV data presented in this dissertation was acquired on the heated jet rig setup using a commercial LaVision Stereo PIV hardware and software system. This appendix describes the hardware setup used for this study.

The first step for setting up the PIV system to record data on the supersonic jet is to specify the solid particle seeding needed for the core flow. Unlike most PIV flows, which are seeded using liquid particles, solid particles are needed to seed the supersonic jet because the heated flow is hot enough to cause vaporization of most liquid particle seeding methods and the plenum pressure is too high to allow for injection of particles from fog or smoke seeders.

To estimate the size of the particle seeding needed, the Stokes number must be computed for candidate particles [1]. To compute the Stokes number, (Stk) the user needs to estimate the particle Mach number (E.1), jet exit velocity (E.2), and the particle Reynolds number (E.3) that results for the desired flow conditions and the manufacturer specified average particle diameter (d_p) and density (ρ_p). Once these values are computed, the Knudsen (Kn) number (E.4), is used to find the relaxation time (t_0) of the particle (E.5) and finally, the Stokes number can be computed (E.6).

$$M_p = M_j = \sqrt{\frac{2}{\gamma - 1}\left(\frac{p_p}{p_{atm}}\right)^{\frac{\gamma-1}{\gamma}} - 1} \quad \text{E.1}$$

$$U_j = M_j\sqrt{\gamma R T_j} \quad \text{E.2}$$

$$Re_p = \frac{\rho_p U_j d_p}{\mu_j} \quad \text{E.3}$$

$$Kn_p = \frac{M_p}{Re_p}\sqrt{\frac{\pi\gamma}{2}} \quad \text{E.4}$$

$$t_o = \frac{\rho_p d_p^2}{18\mu_j}\left(1 + 2.7Kn_p\right) \quad \text{E.5}$$

$$St = \frac{t_o U_o}{l_o} \quad \text{E.6}$$

(a) **(b)**

C.1. Solid particle cyclone seeder (a) and fog generator (b) used to seed the supersonic jet flow

The particles used to seed the core flow were 350 nm Al_2O_3 particles with an average density of 3950 kg/m^3 and an average diameter of 300 nm. The entrainment flow was seeded with mineral oil particles with an average density of 800 kg/m^3 and an average diameter ranging between 500 and 700 nm. This resulted in Stokes numbers of 0.03 for the primary core flow and 0.00125 for the entrainment flow.

The core flow seeding was provided by a custom built solid particle cyclone seeder (A.1(a)) which injected seed into both the primary and secondary jet paths. The pressure to operate the solid particle seeder was supplied by the shop compressed air line and was controlled by a regulator from inside of the jet cell control room. Since one seeder was used for two plenums operating at different pressures, a second regulator was mounted to the downstream path providing seed to the secondary plenum. This helped to reduce the number particles being injected into the secondary plenum. The entrainment air was seeded using a MDG MAX 3000 fog generator (A.1(b)). A compressed nitrogen gas tank was used to supply pressure to operate the generator. The fog generator was turned on from inside the jet cell control room prior to data acquisition and was capable of filling the entire test cell with smoke.

A Quantel Evergreen brand EVG00200 Nd:YAG laser was used as the light source for the low-speed PIV system. This laser is capable of producing 15 double laser pulses per second at 200 mJ/pulse with inter-frame times as low as 0.6 μs. The laser head and pump were mounted onto a moveable cart constructed out of T-slotted aluminum frame material. The laser head was installed onto an optical breadboard along with the two LaVision Imager sCMOS cameras. The breadboard was mounted to a Velmex linear traverse which laser head and cameras to be traversed in the stream-wise direction to acquire the entire developmental region of the jet.

To control the diameter of the emitted laser and the resulting laser sheet thickness, a collimator was mounted onto the laser head. A collimator is a device which contains a set of round lenses that produce an effectively long focal length and serves to narrow and focus the emitted laser beam.

A 400-750 nm anti-reflective coated fused silica mirror was used to redirect the collimated laser beam vertically to intersect with the center plane of the jet flow. The anti-reflective coating is necessary to minimize laser burn on the mirrors over long periods of experimentation. Two cylindrical lenses (each with a -10 focal length) were connected in series and mounted to the mirror to generate the laser sheet. Three lenses were used in order to spread the sheet wide enough to encompass the entire field of view of the cameras as the cart platform where the laser was mounted was ~ 0.5 meters below the field of view of the cameras. An image of the mirror and cylindrical lens mounted to the laser head is shown in Fig. A.2.

C.2. Quantel Evergreen laser head with mounted collimator, mirror, and cylindrical lenses.

The cameras were mounted on t-slotted posts above the laser head and were positioned so that the nozzle was centered in the frame of both cameras. Each camera was optimally angled at 45° towards each other to minimize in-plane uncertainties from cross-correlation. Two 50 mm focal length Nikon lenses were used on each camera with a set f-stop value of 4. These lenses and the f-stop value were found to give the best imaging results from trial and error.

Due to the large angle the cameras are positioned relative to the focusing plane of the jet, Schiempflug adapters were mounted between the camera photodetectors and the lenses. The adapters allow for the entire field of view to be in focus even though the cameras are angled away from the desired focus plane.

After physically setting up the laser and optics, a LaVision Type 31 3D calibration plate was mounted to the nozzle and aligned to where the measurement plane was desired. Before beginning laser sheet alignment, the laser and camera hardware should be connected to the PIV computer as accidental movement of the hardware will affect the alignment. After this, the laser was turned on to the lowest power setting and operated manually using the controls on the laser pump. The emitted laser sheet was then aligned with the calibration plate. Alignment is achieved when the thin laser sheet evenly illuminates the upraised surface of the calibration plate.

Once laser alignment was completed, the PIV software was setup for data acquisition. After following the process for connecting the PIV hardware to the computer described in the DaVis manual, the first operation was to calibrate the camera intensities. This involved putting the lens caps onto the camera and running the intensity calibration in the DaVis software. Following this, the cameras were focused onto the calibration plate and image calibration was performed using the calibration wizard in DaVis.

After successfully performing the calibration, the lenses for each camera were outfitted with a 532 nm band-pass light filter to eliminate light from all other wavelengths which serves to reduce noise in the raw particle images. The bay doors were opened to allow the jet flow to escape the room and a black laser cloth was draped over the hypersonic rig. The laser safety fabric was used to prevent damage to the hypersonic rig from the particle seeding and to provide a clean background for the camera imaging. Shakedown runs were then conducted on low speed jet flow (~10 to 20 m/s) to fine tune the focus on the particles in the flow and to see if the system is operating correctly. Laser power was set to 50% for both laser heads for the shakedown and production runs in this experiment. The flow for the shakedown was provided entirely by pressure from the solid particle seeder supplied by the shop air pressure line. Note: in order to get correlations at this low speed, the inter-frame time must be large enough to see frame-to-frame particle movement.

Once the low speed shakedown runs were completed, the jet was brought up to Mach 1.5, but kept unheated, and the solid particle seeder and fog generator were turned on. At this condition, a second set of shakedown runs were conducted to make sure the seeders were working properly. Once again, it is important to adjust the inter-frame time to achieve correlations at the higher speed. Once this shakedown run is completed, the seeders were turned off to conserve material.

Next, the heater is turned on and the jet flow conditions were adjusted to the desired operating point. Before conducting the actual measurement, the jet was allowed to run at condition for at least 30 minutes to allow the jet to reach thermal steady state. During the heat up time, a final set of shakedown runs were conducted to find the best inter-frame time for data acquisition and to make sure that good correlations are achieved. After the jet reached steady state, background images were acquired at all of the measurement locations in the jet prior to seeding the flow for measurement.

References

[1] Scarano F., 2007, Overview of PIV in Supersonic Flows. In: Particle Image Velocimetry: New Developments and Recent Applications. Topics in Applied Physics, 112. Springer, Berlin, Heidelberg, pp. 446-447.

D. Processing of Raw PIV Images in LaVision

After acquiring particle images from the jet, processing of the raw images must be done to extract velocity data from the sample. The first step is to filter the raw particle images so that the particle signal for the cross-correlation is improved. To do this for the supersonic jet, a background subtract is performed. This process takes an average of the images acquired while the jet is running with no seed present, then subtracts the resulting image from each image acquired containing particles.

Following the background image subtract, stereo self-calibration was applied to the images. The self-calibration technique uses the recorded particles to quantify and correct misalignment between the laser sheet and the calibration plate.

After self-calibration was applied to the images, image pre-processing was performed on the raw images. A four pixel sliding background image subtraction was performed to increase the fidelity of the individual particles acquired. Additionally, a particle intensity normalization filter with a scale of six was applied to the data which corrects for intensity variations across the field of view. The results of the background subtract and the image pre-processing filtering can be seen in Fig. D.1.

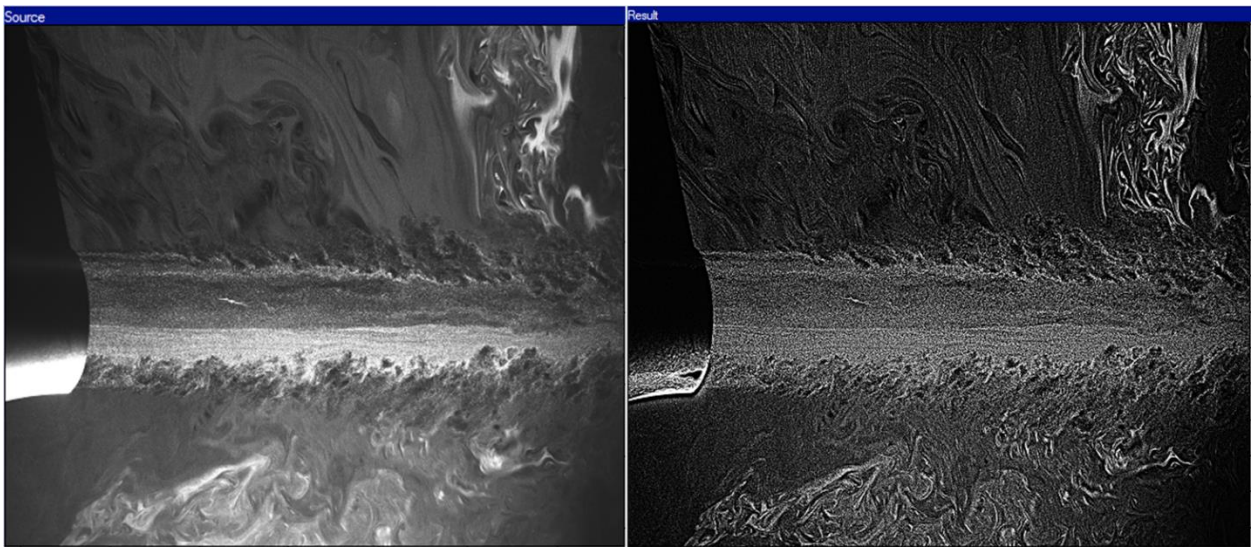

(a) **(b)**

D.1. Raw image (a) and pre-processed image (b) comparison of the seeded heated supersonic jet

No mask was used in the processing of the data set as the only geometry present in the field of view was the nozzle and this geometry was used as a reference point for translating the resolved velocity field so that the nozzle centerline was at y/D = 0 and the nozzle lip was at x/D = 0.

Figure D.2 contains an image of the vector calculation parameter settings used. Four stereo cross-correlation passes were used to process the images from the two cameras to obtain the three-component velocity field. The interrogation window size used for the first two correlation passes was square and consisted of 128x128 pixels with 25% overlap. The final two correlation passes used a 64 x 64 pixel window size with 75% window overlap an adaptive PIV window shape. The adaptive PIV window uses the local velocity gradients computed from the previous passes to best capture the flow structure at each resolved vector location. The “high accuracy mode for final passes” and the “Calculate Uncertainty” options were selected as well.

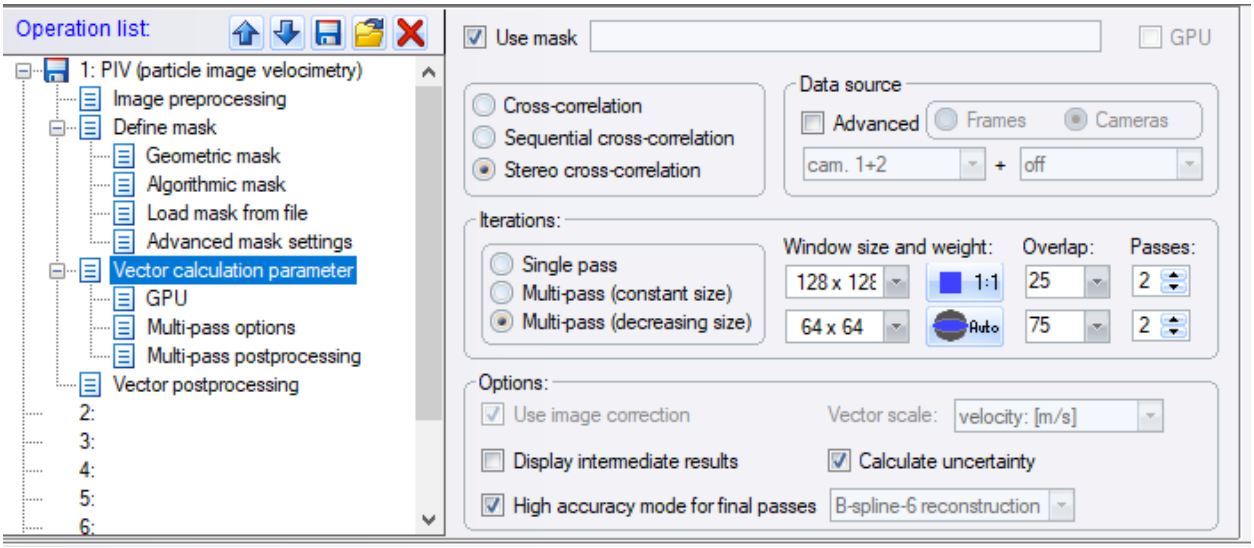

D.2. Settings for calculating velocity vectors from the filtered particle images

Figure D.3 contains an image of the multi-pass post-processing settings used. In the multi-pass post-processing settings, the follow options were applied. The “Delete vector if its peak ratio Q<” was set to 2. The peak ratio, Q, is a measure of the prominence of the largest peak in the interrogation window and is the ratio of the largest peak to the second largest peak. A peak ratio of 2 means that the largest correlation peak is at least twice as large as the second peak in the interrogation window, which ensures a low uncertainty in the computed velocity correlation.

A spatial 2 x median filter was applied which was set to remove velocity vectors if their difference to the average of their neighbors were greater than 3 standard deviations while processing the velocities, then re-insert them if their difference was less than 4 standard deviations of the average of their neighbors after computing the entire vector field. The “remove groups with <” option was set to 100 to eliminate interrogation windows with low signal.

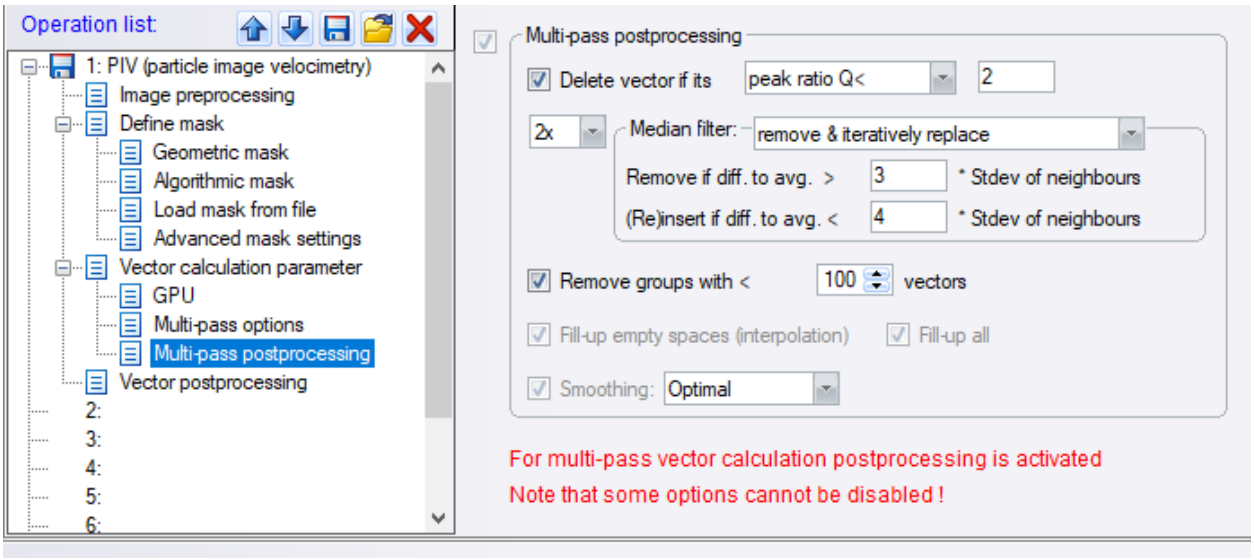

D.3. Multi-pass post-processing settings used to process the PIV images

Figure D.4 contains the vector post-processing settings used for the supersonic jet data. The same settings used during the multi-pass post-processing step for the peak ratio Q, 2x median filter, and remove groups were utilized during the post processing phase. In addition to this, spatial linear interpolation was used to fill in holes in the vector field and a smoothing filter was applied to the final velocity vector fields.

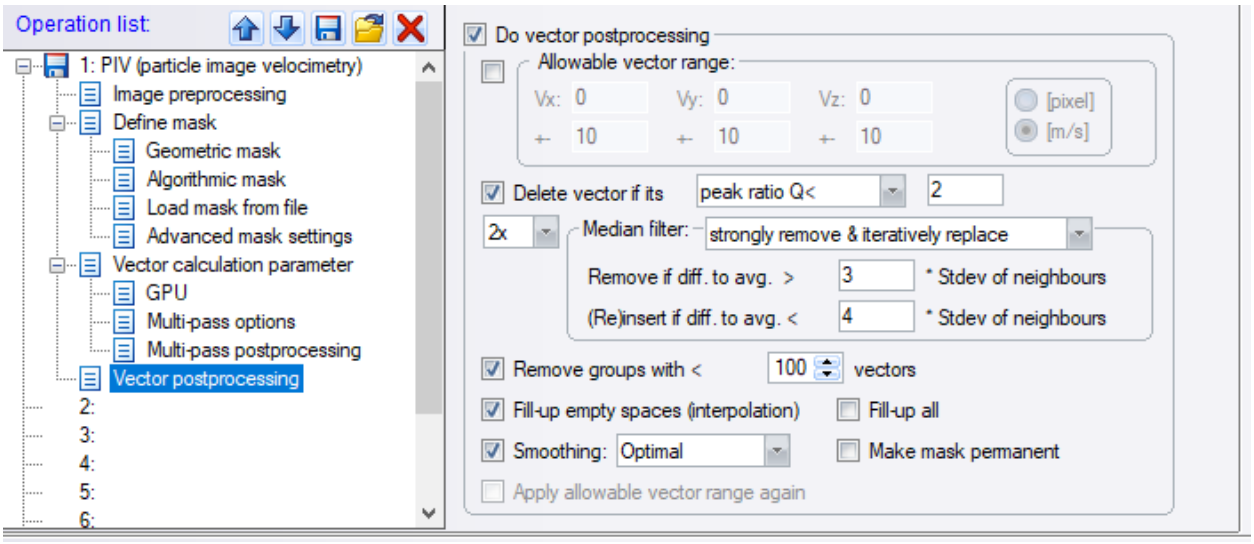

D.4. Vector post-processing settings used to process the PIV images

Following this processing, the average and standard deviation velocities as well as the Reynolds stresses, the turbulent kinetic energy, and the uncertainties for each were computed for the velocity field and analyzed in DaVis prior to exporting to ensure that the velocity field looked reasonable prior to exporting for further analysis in MATLAB. The uncertainties computed by DaVis use the method developed by Wieneke [1] and the uncertainties reported using this method are smaller than those computed through the standard error estimator. Thus to be conservative, the standard error uncertainty is used for the data presented in this dissertation.

References

[1] Wieneke, B., 2015, PIV uncertainty quantification from correlation statistics, Measurement Science and Technology, 26 (7) pp. 1-10.

E. Filtering PIV Velocity Vectors

Based on the physics of the measured flow field, band pass magnitude filters were set based on the maximum and minimum expected three-component velocities. For the uniform and offset jets, table E.1 lists the maximum and minimum allowable velocity ranges for all three components measured. Values outside of this range were set to NaN's. Additionally, any values that had an exact value of zero were also set to NaN's as well.

Table E.1. Velocity magnitude filter settings

Velocity Component	Lower Limit	Upper Limit
$\boldsymbol{U_x}$	-100 m/s	1.5 U_j
$\boldsymbol{U_y}$	$-0.5\ U_j$	$0.5\ U_j$
$\boldsymbol{U_z}$	$-0.5\ U_j$	$0.5\ U_j$

After filtering the velocities based on the magnitude of the fluctuations, a valid signal filter was used. For each resolved vector location, the ratio of NaN values to non-NaN values in the velocity signal were checked. This filter serves to remove velocities near the edges of the PIV field of view or beyond the end of the laser sheet where the signal-to-noise ratio was low. If the validity ratio for a resolved vector location was below 0.9, that location was marked and saved in a separate filter matrix, which will be applied at the end of the filtering process.

After using the valid signal filter, an ellipsoidal standard deviation filter was applied to the data at each resolved vector location. The filter removed all velocity values at a single spatial location whose fluctuating velocity values were greater than four standard deviations from zero. To do this, the mean subtracted velocities were evaluated for all three velocity components (this equation can be found in Appendix E).

After doing this, proper orthogonal decomposition was applied to each pair of signals, giving the eigenvectors and eigenvalues which align with the principal axes of the data pair (i.e. u'_x & u'_y, u'_x & u'_z *and* u'_y & u'_z). The first two eigenvectors give the direction of the principal axes relative to the Cartesian coordinate system.

The eigenvectors were used to rotate the data so that the principal axes align with the Cartesian axes using three-dimensional rigid body rotation. The angle between the principal and Cartesian axes for each velocity component pair (α, β, γ) can be found using E.3.

$$\alpha, \beta, \gamma = \tan^{-1}\left(\frac{\vec{v}(2)}{\vec{v}(1)}\right) \tag{E.2}$$

The formula for rotating the data so the principal axes are aligned with the Cartesian axes [1] is given in E.4-6.

$$\begin{aligned} x = {} & u'_x(\cos(\alpha)\cos(\beta)\cos(\gamma) - \sin(\alpha)\sin(\gamma)) \\ & - u'_y(\cos(\alpha)\cos(\beta)\sin(\gamma) + \sin(\alpha)\cos(\gamma)) \\ & + u'_z(\cos(\alpha)\sin(\beta)) \end{aligned} \tag{E.3}$$

$$\begin{aligned} y = {} & u'_x(\sin(\alpha)\cos(\beta)\cos(\gamma) + \cos(\alpha)\sin(\gamma)) \\ & - u'_y(\sin(\alpha)\cos(\beta)\sin(\gamma) - \cos(\alpha)\cos(\gamma)) \\ & + u'_z(\sin(\alpha)\sin(\beta)) \end{aligned} \tag{E.4}$$

$$z = -u'_x\sin(\beta)\cos(\gamma) - u'_y\sin(\beta)\sin(\gamma) + u'_z\cos(\beta) \tag{E.5}$$

Once the data is rotated, the standard deviation for each of the rotated data components were evaluated, then the ellipsoidal standard deviation filter (E.6) is applied. Values greater than the filter limits were removed and set to NaN. The rest of the values in the rotated data matrix were set to ones, then the original data matrices and the newly created filter matrix were multiplied to eliminate the outlying samples in the un-rotated data.

$$F_\sigma = \left(\frac{x}{4\,\sigma_x}\right)^2 + \left(\frac{y}{4\,\sigma_y}\right)^2 + \left(\frac{z}{4\,\sigma_z}\right)^2 > 1 = NaN \tag{E.6}$$

After applying the filters to the velocity field, a two-dimensional linear spatial interpolation scheme was used to fill in the missing data in the velocity fields. Finally, the valid signal filter was applied to the interpolated vector field again to remove erroneous extrapolated data.

References

[1] Haber, H., 2012, Three-Dimensional Rotation Matrices [Online], Available: http://scipp.ucsc.edu/~haber/ph216/rotation_12.pdf [Accessed: 4 June 2019].

F. Single and Two Point Statistical Processing

The equations used to evaluate the single point velocity statistics are given in this section and are evaluated on the filtered instantaneous velocity vectors.

Mean Velocity

$$\bar{U} = \frac{1}{N}\sum_{n=1}^{N} U_n \quad \text{E.1}$$

Instantaneous Fluctuating Velocity

$$u' = U - \bar{U} \quad \text{E.2}$$

Instantaneous Reynolds Stress (where u' and v' are any two fluctuating velocity signals at a single location)

$$\tau'_{uv} = u'v' \quad \text{E.3}$$

Mean Reynolds Stress (where u' and v' are any two fluctuating velocity signals at a single location)

$$\overline{\tau'_{uv}} = \overline{u'v'} = \frac{1}{N}\sum_{n=1}^{N}(U_n - \bar{U})(V_n - \bar{V}) \quad \text{E.4}$$

Mean Fluctuating Velocity (Standard Deviation of Velocity)

$$\bar{u'} = \sqrt{u'u'} \quad \text{E.5}$$

Mean Vorticity Thickness

$$\delta_{\bar{\Omega}_\theta} = \frac{U_j}{\max(\partial \bar{U}_x/\partial y)} \quad \text{E.6}$$

Mean Two-Point Correlation Coefficient (when i,j = x,y, the autocorrelation coefficient is obtained)

$$\bar{\rho}_{u'v'} = \frac{\overline{u'(i,j)v'(x,y)}}{\sqrt{\overline{u'u'(i,j)}\;\overline{v'v'(x,y)}}} \quad \text{E.7}$$

The uncertainties for the single point statistics are given below and are evaluated using the method presented in Bendat and Piersol [1]. The uncertainties for the resolved quadrant analysis data presented in Paper 2 are computed using equation E.8 with N being the number of samples which pass the condition.

Mean Velocity Uncertainty

$$\delta(\bar{U}) = \frac{\bar{u'}}{\sqrt{N}} \quad \text{E.8}$$

Mean Reynolds Stress Uncertainty

$$\delta(\overline{u'v'}) = \sqrt{\frac{2}{N-1}}(\overline{u'v'}) \quad \text{E.9}$$

Mean Fluctuating Velocity Uncertainty

$$\delta(\bar{u'}) = \frac{u'}{\sqrt{N}} \quad \text{E.10}$$

The uncertainty in the mean correlation coefficient and the vorticity thickness are evaluated using the Kline-McClintock [2] method for propagating uncertainties. The uncertainty in the x and y positions of the data are taken from the LaVision software and the uncertainty in U_j is assumed to be negligible for the supersonic jet.

Mean Two-Point Correlation Coefficient Uncertainty

$$\delta(\bar{\rho}_{u'v'}) = \sqrt{\left(\frac{\partial\left(\bar{\rho}_{u'v'}(x,y)\right)}{\partial u'(x,y)}\right)^2 \delta\left(u'(x,y)\right)^2 + \left(\frac{\partial\left(\bar{\rho}_{u'v'}(x,y)\right)}{\partial v'(x,y)}\right)^2 \delta\left(v'(x,y)\right)^2} \quad \text{E.11}$$

Mean Vorticity Thickness Uncertainty

$$\delta(\delta_{\bar{\Omega}_\theta}) = \sqrt{\left(\frac{\partial\left(\delta_{\bar{\Omega}_\theta}\right)}{\partial U_j}\right)^2 \delta\left(U_j\right)^2 + \left(\frac{\partial\left(\delta_{\bar{\Omega}_\theta}\right)}{\partial \bar{U}_x}\right)^2 \delta(\bar{U}_x)^2 + \left(\frac{\partial\left(\delta_{\bar{\Omega}_\theta}\right)}{\partial y}\right)^2 \delta(y)^2} \quad \text{E.12}$$

References

[1] Bendat, J.S., Piersol, A.G., 2010, Random Data: Analysis and Measurement Procedures, 4th Edition. Wiley.
[2] Kline, S. J., & McClintock, F. A., 1953, Describing Uncertainties in Single-Sample Experiments. Mechanical Engineering, 3–8.

G. The Reynolds Stress Transport and Shear Stress Production

In Section 2.2.1 of the literature review, it was established that the dominant source of turbulent self-noise was $\rho U_i U_j$ and the shear stresses were neglected. However, it has also been established experimentally that increasing mixing near the nozzle of turbulent plumes reduces noise. In order for the increase in mixing to have an impact on noise, the changes in the shear stresses need to be understood. In this section, I will establish the validity of using the Reynolds-averaged Navier-Stokes equations (which are derived for incompressible flow) to analyze a supersonic heated jet and the impact of the Reynolds shear stress on the normal stress production.

The Reynolds stress transport (RST) equation is the second moment of the Navier-Stokes equation, and describes the transport, production, redistribution, and dissipation of the Reynolds stresses in a flow field. The incompressible RST is (Eq E.1),

$$\frac{DR_{ij}}{Dt} = D_{ij} + P_{ij} + \Pi_{ij} + \omega_{ij} - \varepsilon_{ij}, \qquad \text{E.1}$$

where R_{ij} is the kinetic Reynolds stress $\overline{u_x' u_y'}/\bar{\rho}$, D_{ij} is the stress diffusion term, P_{ij} is the stress production term, Π_{ij} is the pressure-strain stress redistribution term, ω_{ij} is the rotational transport term, and ε_{ij} is the dissipation rate term (Pope 2000). Due to not having the mean density and pressure field in the measurement domain, only the convection transport and stress production terms are computable with the PIV data collected for this study.

The validity of using the incompressible RST equation to evaluate data collected on a supersonic heated jet will now be addressed. Ideally, one would compute the transport of compressible stresses by analyzing the first moment of the Favre-averaged Navier-Stokes equations, but due to the lack of information regarding the density field in the measurement domain, this analysis is not possible. To confidently apply the RST equation to the current data set, it must be established that the turbulence behaves in an incompressible manner for the given aero-thermodynamic conditions.

The strong Reynolds analogy or Morkovin's hypothesis (Bradshaw 1974) is a conjecture which assumes the direct effects of density fluctuations on turbulence is small if the following is true (Eq E.2),

$$\frac{\overline{p'}}{\bar{p}} \ll 1 \; and \; \frac{\overline{\rho'}}{\bar{\rho}} \ll 1, \qquad \text{E.2}$$

where $\bar{p}$ is the mean pressure, $\overline{p'}$ is the root-mean-square fluctuating pressure, $\bar{\rho}$ is the mean density, and $\overline{\rho'}$ is the root-mean-square fluctuating density.

The fluctuating density ratio can be estimated via the strong Reynolds analogy. Since the turbulence intensity, $u_x'/\bar{U}_j$, is small for both the uniform and thermally offset jets (proven in the journal paper presented in Section 3), $\rho'/\bar{\rho}$ will be small as long as $(\gamma - 1)M_c^2 \leq 1$, where M_c is the convection velocity and γ is the adiabatic ratio. The largest M_c in the developmental region of both jet flows presented in this study occurs in the thermally offset jet with a value of 0.87 which results in the max scaling term in the flow $(\gamma - 1)M_c^2 = 0.30$. The largest observed value is sufficiently smaller than 1, thus guaranteeing all other values in the flow field will be smaller and validating strong Reynolds analogy for the entire field.

In the Reynolds stress transport equation, the stress production term, P_{ij}, governs the generation of the Reynolds stress in the flow (Eq. E.3),

$$P_{ij} = \left(\overline{u_i' u_k'} \frac{\partial U_j}{\partial k} + \overline{u_j' u_k'} \frac{\partial \bar{U}_i}{\partial k} \right), \qquad \text{E.3}$$

where $i, j,$ and k are each equal to x and y in every combination. The production term describes the transfer of kinetic energy from the mean flow to the turbulent fluctuations. When this term is expanded, it can be easily shown that The result reveals that all three Reynolds stress components and all four velocity gradients contribute in some way to the production of each other Reynolds stress component in the jet.

References

[1] Pope, S. B., 2000, *Turbulent Flows*, Cambridge University Press, Cambridge.
[2] Bradshaw, P., 1974, "The Effect of Mean Compression or Dilatation on the Turbulence Structure of Supersonic Boundary Layers," J. Fluid Mech., **63(**3), pp. 449–464.

H. Proper Orthogonal Decomposition

POD has been a prominent method for identifying spatially and temporally coherent structures in jet flow measurements. POD restructures flow data into modes and temporal coefficients which are optimally ranked by their energy contribution to the flow field. The snapshot method [1,2], is a computationally efficient method for applying POD to PIV data. POD is performed on the fluctuating Reynolds shear stress $u'_x u'_y(x,y,t)$ in this study,

$$\boldsymbol{u'_x u'_y}(x,y,t) = [\boldsymbol{U_x}(x,y,t) - \boldsymbol{\bar{U}_x}(x,y)] \cdot \left[\boldsymbol{U_y}(x,y,t_k) - \boldsymbol{\bar{U}_y}(x,y)\right], \quad \text{E.1}$$

where $\boldsymbol{U_x}(\boldsymbol{x},\boldsymbol{y},t_n)$ and $\boldsymbol{U_y}(\boldsymbol{x},\boldsymbol{y},t_n)$ are discrete samples of instantaneous axial and transverse velocities at location (x,y) in the measurement domain and $\bar{U}_x(x,y)$ and $\bar{U}_y(x,y)$ are the time averaged velocities at the same location. The fluctuating Reynolds stress field can be represented by,

$$\boldsymbol{u'_x u'_y}(\boldsymbol{x},\boldsymbol{y},t) = \sum_{i=1}^{M} \boldsymbol{a_i}(t)\boldsymbol{\psi_i}(\boldsymbol{x},\boldsymbol{y}) + \boldsymbol{u'_x u'_{y_{res}}}(\boldsymbol{x},\boldsymbol{y},t_n) \quad \text{E.2}$$

Where a are the temporal POD modes, ψ are the spatial POD modes, i is the mode number and M are the total number of snapshots. The goal is to find the lowest order representation of the fluctuating Reynolds stress field which minimizes the norm of the residual.

The temporal POD modes can be determined from the eigenvalues, λ_i of the autocorrelation matrix, $\boldsymbol{R}$, at each point in the domain,

$$\boldsymbol{R} = \left[\boldsymbol{u'_x u'_y}(\boldsymbol{x},\boldsymbol{y},t_n)\right]^T [\boldsymbol{u'_x u'_y}(\boldsymbol{x},\boldsymbol{y},t_n)] \quad \text{E.3}$$

$$\boldsymbol{R}\,\boldsymbol{a_i} = \lambda_i \boldsymbol{a_i}. \sum_{i=1}^{N} a_i(t)\boldsymbol{\psi_i}(\boldsymbol{x},\boldsymbol{y}) + \boldsymbol{u'_x u'_{y_{res}}}(\boldsymbol{x},\boldsymbol{y},t_n) \quad \text{E.4}$$

The resulting eigenvalues are real and nonnegative and sorted from largest to smallest magnitude and its corresponding temporal POD mode is sorted based on its eigenvalue pair. The temporal POD modes are mathematically constrained to be orthogonal to each other.

The spatial POD modes can be determined by first normalizing the temporal mode, $\overline{a_i a_j} = \lambda \delta_{ij}$, then combining the temporal mode with the entire fluctuating shear stress field,

$$\boldsymbol{\psi_i}(\boldsymbol{x},\boldsymbol{y}) = \frac{1}{\sqrt{N\lambda_i}} \sum_{i=1}^{N} a_i(t_n)\boldsymbol{u'_x u'_y}(\boldsymbol{x},\boldsymbol{y},t_n). \quad \text{E.5}$$

The resulting POD field contain structures in each mode which reveal correlated spatial fluctuations, with the highest energy containing structures located in the first mode, the second highest in the second mode, and so on to mode M. The eigenvalues of the i^{th} mode represents the energy associated with that mode. It is important to note that, as the orthogonality constraint is mathematically enforced and not physics based, the coherent structures observed in the modes of the decomposition are orthogonal. This means that the spatial POD modes may show features which do not physically exist [3]. Additionally, the resultant spatial POD modes only give insight into the wavenumber space and provide no insight into the frequencies associated with the observed structures as only the spatial autocorrelation tensor was utilized in determining the modes [4].

Convergence of the resolved modes of the POD technique should be analyzed prior to attempting further analysis. To test if the modes are converged, one needs compute the modes with fewer samples into the POD function than the total amount available. If the resolved mode shapes change drastically with a reduction in the number of samples used, then the POD modes have not converged. One way to address this issue is to use record more samples in future experiments or to employ block processing, a technique presented in the Appendix G.

References

[1] Sirovich, L., 1987, Proper orthogonal decomposition applied to turbulent flow in a square duct. Q. Appl. Maths 45, 561–671
[2] Kostas, J., Soria, J. & Chong, M., 2005, A comparison between snapshot POD analysis of PIV velocity and vorticity data. Exp. Fluids 38 (2), 146–160.
[3] Soria, J., 2006, Particle image velocimetry – application to turbulence studies. In Turbulence and Coherent Structures in Fluids, Plasmas and Nonlinear Media, pp. 319–330. World Scientific
[4] Edgington-Mitchell, D., Oberleithner, K., Honnery, D. R., & Soria, J., 2014, Coherent structure and sound production in the helical mode of a screeching axisymmetric jet. Journal of Fluid Mechanics, 748, 822–847.
[5] Towne, A., Schmidt, O. T., & Colonius, T., 2018, Spectral proper orthogonal decomposition and its relationship to dynamic mode decomposition and resolvent analysis. Journal of Fluid Mechanics, 847, 821–867.

I. Block Processing of Velocity Data

When there are a limited number of temporal samples in a resolved velocity signal but a large number of spatial data is present, block processing can be employed to increase the number of effective samples in the time domain. This technique groups multiple spatially adjacent velocity signals together and treats the grouping as a single resolved velocity vector. In doing this, the effective number of temporal samples available is increased. A visual example of the technique is presented in Fig. I.1.

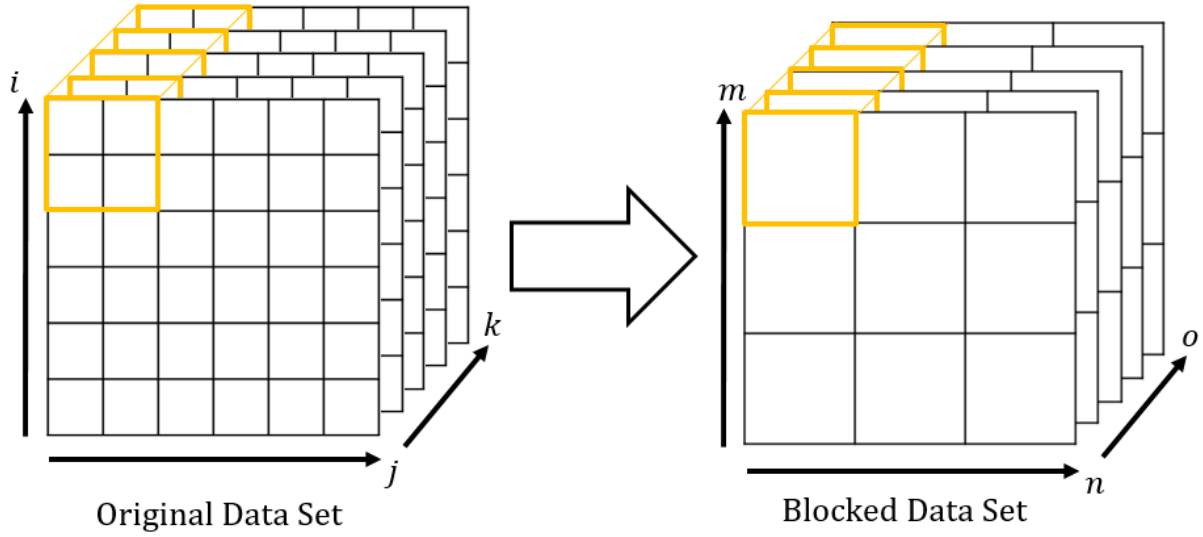

Fig.I.1. Visual example of block processing. The number of spatial samples is reduced to increase the number of temporal samples at a single location.

Before applying block processing to PIV data, the velocity gradients in the flow need to be analyzed. If the change in the velocity components between adjacent velocity locations are large, then the turbulence statistics which result from the block processing will be inaccurate. To minimize this error, block processing should be performed in the direction of the smallest gradient (i.e. $\partial \bar{U}_x/\partial x$ for the supersonic jet) The error between the block processed data and the original data set can be evaluated by interpolating the blocked processed mean velocity fields onto the original velocity field spatial grid then taking the difference between the original velocity field and the block processed velocity field.